12-2006

Interference effects among $J = 3/2^+$ resonances in ^{19}Ne system & Searching for resonances in the unbound ^{6}Be nucleus

Kyung Yuk Chae
University of Tennessee - Knoxville

Recommended Citation

Chae, Kyung Yuk, "Interference effects among $J = 3/2^+$ resonances in ^{19}Ne system & Searching for resonances in the unbound ^{6}Be nucleus. " PhD diss., University of Tennessee, 2006.
https://trace.tennessee.edu/utk_graddiss/1920

To the Graduate Council:

I am submitting herewith a dissertation written by Kyung Yuk Chae entitled "Interference effects among *J* = $3/2^+$ resonances in ^{19}Ne system & Searching for resonances in the unbound ^{6}Be nucleus." I have examined the final electronic copy of this dissertation for form and content and recommend that it be accepted in partial fulfillment of the requirements for the degree of Doctor of Philosophy, with a major in Physics.

Mike W. Gudiry, Major Professor

We have read this dissertation and recommend its acceptance:

Michael S. Smith, Pengcheng Dai, Chia C. Shih, Lawrence W. Townsend

Accepted for the Council:
Carolyn R. Hodges

Vice Provost and Dean of the Graduate School

(Original signatures are on file with official student records.)

To the Graduate Council:

I am submitting herewith a dissertation written by Kyung Yuk Chae entitled "Interference effects among $J^\pi = \frac{3}{2}^+$ resonances in ^{19}Ne system & Searching for resonances in the unbound ^{6}Be nucleus." I have examined the final electronic copy of this dissertation for form and content and recommend that it be accepted in partial fulfillment of the requirements for the degree of Doctor of Philosophy, with a major in Physics.

Mike W. Gudiry
Major Professor

We have read this dissertation
and recommend its acceptance:

Michael S. Smith

Pengcheng Dai

Chia C. Shih

Lawrence W. Townsend

Accepted for the Council:

Linda Painter
Interim Dean of Graduate Studies

(Original signatures are on file with official student records.)

Interference effects among $J^\pi = \frac{3}{2}^+$ resonances in ^{19}Ne system

&

Searching for resonances in the unbound ^{6}Be nucleus

A Dissertation

Presented for the

Doctor of Philosophy

Degree

The University of Tennessee, Knoxville

Kyung Yuk Chae

December 2006

Dedication

This dissertation is dedicated to my parents who raised me with freedom of choice,
to my wife, Miun, who has always been there,
and to my son, Hagen, who has grown into a wonderful 1 year old boy.

Acknowledgments

I would like to take this opportunity to thank the many people who have made this work possible. First and foremost, I would like to thank my dissertation advisor, Dr. Mike Guidry for his guidance and encouragement. Very special thanks go to three research physicists of the experimental nuclear astrophysics group at the Oak Ridge National Laboratory. Michael Smith lead me to this very fun field of study, and taught me how to be a professional scientist. I am indebted to Dan Bardayan for his watchful guidance, kind encouragements, forgiveness, and three ^{28}Si targets. He never got tired of answering my questions. Jeff Blackmon also gave me lots of inspiration through conversation and discussion.

Thanks as well to the other my committee members: Drs. Pengcheng Dai, Chia Shih, and Lawrence Townsend. My thanks go out to each of them for having so kindly agreed to serve on my committee.

A number of people that I have met at the ORNL deserve my special thanks. Thanks to Ray Kozub for his wonderful explanation about physics. John Shriner helped me a lot in using MULTI. Valdir Guimarães gladly came to ORNL from Brazil in order to help us, twice. Kate Jones taught me what kind of stuff should be written on a log book: *everything*. Steve Pain is always "Right.", and he is still too tall. Caroline Nesaraja encouraged me whenever I was depressed. Jake Livesay, my longest buddy in this country, has been keeping me motivated and encouraged when I never saw the light at the end of the tunnel. Jeff Thomas always reminds me the beautiful trip to Los Alamos and my *first* shift. Brian Moazen is getting married soon. Also, I would like to thank Zhanwen Ma, Micah Johnson, Dale Visser, J. J. Das, Darren Gregory, Stan Paulauskas, Matt Porter-Peden, and Nathan Smith. This work could not be done without your help.

Finally, special thanks should go to Eunjoo Im, Hagen's first and only nanny so far, for her great taking care of our son.

Thank you all for always being there.

Abstract

The ^{18}F(p,α)^{15}O reaction plays a crucial role in understanding γ-ray emission from novae. Because of the importance of understanding the ^{18}F + p reactions, a number of studies of the A=19 isobars have been made using stable and exotic beams. The interference effects among $J^{\pi} = \frac{3}{2}^{+}$ resonances in the $^{18}F + p$ system, however, have never been measured, but they can change the S-factor by a factor of 20 at nova energies. R-matrix calculations indicate that the cross sections above the $E_{c.m.} = 665$ keV resonance are sensitive to the interference between the $E_{c.m.} = 8$, 38, and 665 keV resonances. In order to study the interference effects, an excitation function for the ^{1}H(^{18}F,α)^{15}O reaction has been measured in the energy range of $E_{c.m.} = 663$-877 keV using radioactive ^{18}F beams at the Holifield Radioactive Ion Beam Facility (HRIBF). By measuring the ^{18}F(p,α)^{15}O cross section off resonance and comparing the cross section with theoretical calculations, we provide the first experimental constraints on the interference of $\frac{3}{2}^{+}$ resonances.

The ^{3}He(^{3}He,2p)^{4}He reaction is responsible for destruction of ^{3}He in stars, and strongly affects the calculated neutrino luminosity from the sun. Previous measurements demonstrated a rise in the ^{3}He(^{3}He,2p)^{4}He S-factor at low energies, which could be due to a low energy resonance in the ^{3}He + ^{3}He (^{6}Be) system, or be due to an electron screening effect. In the ^{6}Be nucleus, however, no excited states have been observed above the first 2^{+} state at $E_x = 1.67$ MeV up to 23 MeV. But there is considerable evidence to support the presence of unknown excited states in ^{6}Be. First of all, in the mirror nucleus ^{6}He two excited states have been established below the $t + t$ threshold at $E_x = 12.3$ MeV. Secondly, a recent measurement at Notre Dame University found tentative evidence for a ^{6}Be level at 9.6 MeV. A search for the missing ^{6}Be levels was performed by studying the $d(^{7}\mathrm{Be},t)^{6}\mathrm{Be}$ reaction with the radioactive ^{7}Be beam at Oak Ridge National Laboratory HRIBF. No excited states in ^{6}Be were found; however, we could set the upper limits on the reaction cross section.

Contents

List of Tables

List of Figures

Chapter 1

Nuclear Astrophysics

Nuclear Astrophysics is the study of nuclear structure and reactions to explain both the formation of all naturally occurring elements in the universe and the structure and evolution of the stars. This field of study can be traced back to Eddington's very early work for the energy production in stars [Edd20]. The standard theory of the stellar energy production at that time was the *contraction hypothesis*: the contraction of a star due to gravitational force causes the energy production. Eddington, however, pointed out that the contraction theory predicted the age of our sun was only 20 million years old, in direct disagreement with evidence suggesting the sun was more than one billion years old [Bol07]. Thus, Eddington postulated that "all the elements are constituted out of hydrogen atoms bound together with negative electrons"[*] [Edd20], and the energy released from this process due to mass difference is the source of star energy production. In 1957, E. M. Burbidge, G. R. Burbidge, Fowler, and Hoyle (and independently, Cameron) presented a coherent theory of nucleosynthesis which demonstrated that all elements heavier than helium could be synthesized in the interior of stars [Bur57].

---

[*] The neutron was not discovered until 1932.

Our current understanding of element synthesis is such that the first light nuclei (such as hydrogen, helium, and lithium) were produced roughly 3 minutes after the *Big Bang*, the beginning of the Universe, and the heavier elements were forged much later through vast series of nuclear reactions inside of stars, with the synthesized heavy elements ejected into the interstellar medium by stellar explosions. A star's mass, temperature, and density helps determine its evolution through all stages in its life. Some important stages and phenomena include the main sequence, giant phase, and explosions such as novae, x-ray bursts, and supernovae. The remainder of this Chapter will focus on a brief history of the Universe and the astrophysical environments.

1.1 Abundance Distribution Curve

Figure 1.1 shows the relative abundance of elements in the solar system. Hydrogen and helium make up approximately 98% of the solar system. The most abundant element on the earth's crust is, however, ^{16}O. The abundance distribution in Figure 1.1 is therefore not universal: the earth and the other planets did not have gravitational fields large enough to retain hydrogen and helium against thermal escape in their original formation [Fow67].

One remarkable fact in Figure 1.1 is the existence of a clear peak at atomic number 26 (iron, ^{56}Fe). The binding energy for a nucleus of proton number Z and mass number $Z + N$ is expressed as

$$B(Z, N) = \left[Z m_p + N m_n - m(Z, N) \right] c^2, \tag{1.1}$$

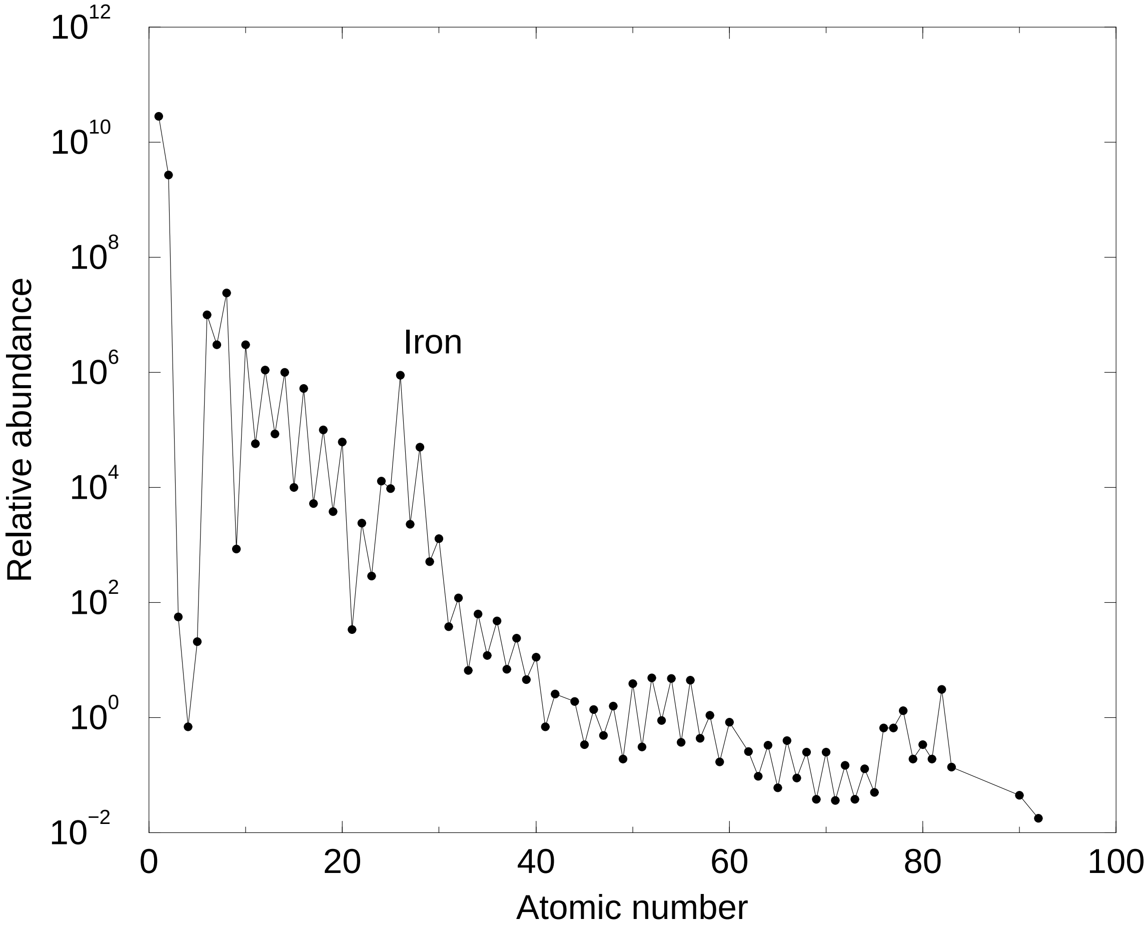

Figure 1.1: Relative abundances vs. atomic number as measured in our solar system.

where $m(Z, N)$ is the mass of the nucleus, m_p, m_n are the mass of a proton and a neutron, respectively. The binding energy per nucleon versus atomic mass number $A(= Z + N)$ is shown in Figure 1.2. The maximum of binding energy occurs in the vicinity of A=60 as a result of the competition between surface and Coulomb effects. The isotopes in this region are called the iron group nuclei, and they are thermodynamically the most stable isotopes in the Universe [Rol88].

1.2 Main Sequence Stars: Hydrogen Burning

A nuclear reaction in which an element Z is converted into other elements is usually called Z burning (e.g., hydrogen burning, helium burning, etc.) when the reaction is thermonuclear. In normal hydrogen burning, two main sequences of reactions are involved: the *pp* chain and the CNO cycle.

The *pp* chain starts with two protons combining together to form a deuterium nucleus, which in turn combines with another proton to form a ^{3}He nucleus:

$$\begin{aligned} p + p &\rightarrow {}^2\mathrm{H} + e^+ + \nu_e, \\ {}^2\mathrm{H} + p &\rightarrow {}^3\mathrm{He} + \gamma. \end{aligned}$$

The ^{3}He nucleus formed in the above process can end up as a ^{4}He nucleus through three different channels, which are conventionally called *pp*-I, *pp*-II, and *pp*-III. The first chain is completed by

$$^3\mathrm{He} +^3 \mathrm{He} \rightarrow {}^4\mathrm{He} + p + p.$$

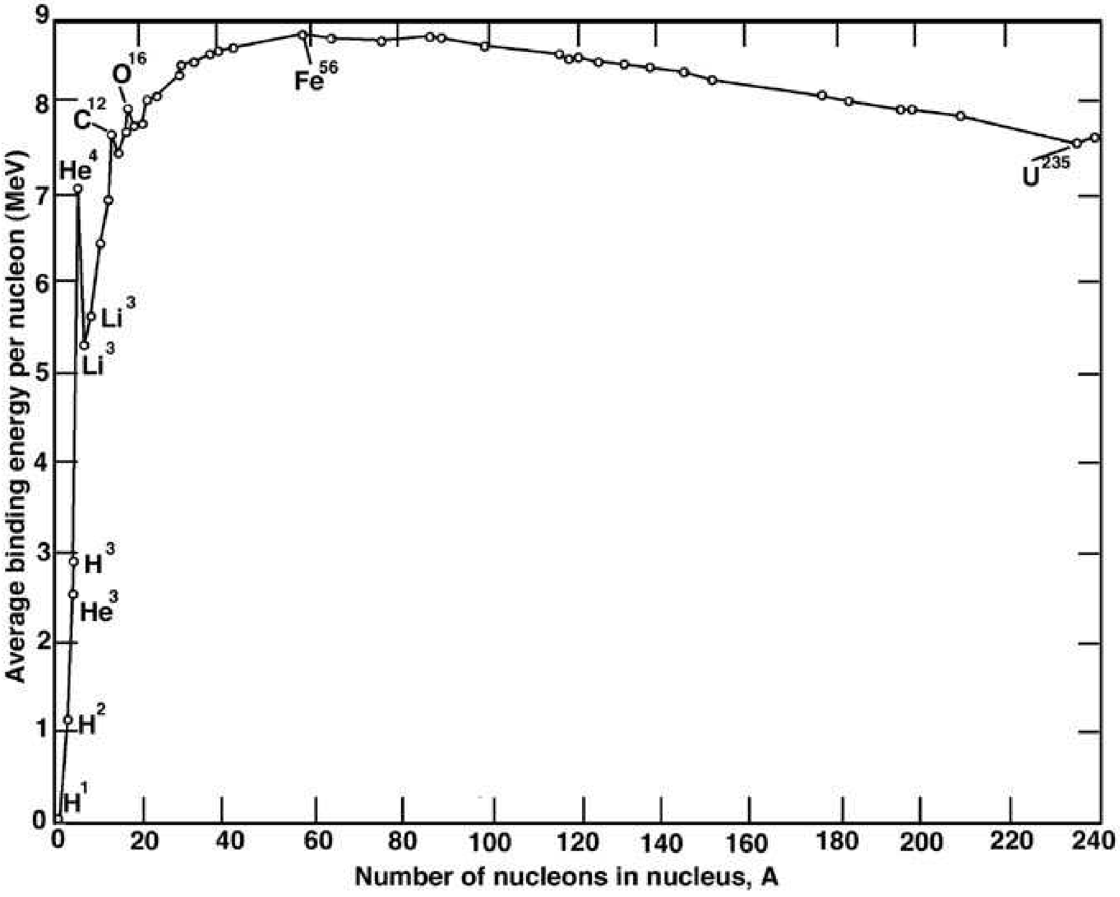

Figure 1.2: The binding energy per nucleon vs. atomic mass number.

The *pp*-II chain is:

$$\begin{aligned} {}^{3}\mathrm{He} + {}^{4}\,\mathrm{He} &\rightarrow {}^{7}\mathrm{Be} + \gamma \\ {}^{7}\mathrm{Be} + e^{-} &\rightarrow {}^{7}\mathrm{Li} + \nu_e \\ {}^{7}\mathrm{Li} + p &\rightarrow {}^{4}\mathrm{He} + {}^{4}\mathrm{He}, \end{aligned}$$

while the *pp*-III chain is:

$$\begin{aligned} {}^{7}\mathrm{Be} + p &\rightarrow {}^{8}\mathrm{B} + \gamma \\ {}^{8}\mathrm{B} &\rightarrow {}^{8}\mathrm{Be} + e^{+} + \nu_e \\ {}^{8}\mathrm{Be} &\rightarrow {}^{4}\mathrm{He} + {}^{4}\mathrm{He}. \end{aligned}$$

The starting point for *pp*-II and *pp*-III requires the ^{4}He nucleus, which could be from the earlier *pp*-I chain reaction or could be present primordially. Calculations based on our current knowledge about our Sun indicate *pp*-I produces about 85% of the Sun's energy, while *pp*-II and *pp*-III produce about 15% and 0.02% respectively.

The *pp* chains do not require the presence of elements heavier than hydrogen to begin. However, the other hydrogen burning mechanism, the carbon-nitrogen-oxygen (CNO) cycle, converts hydrogen into helium in the presence of heavier elements in which the heavier elements act only as catalyst. The sequence is:

$$\begin{aligned}
{}^{12}\mathrm{C} + p &\quad\rightarrow\quad {}^{13}\mathrm{N} + \gamma \\
{}^{13}\mathrm{N} &\quad\rightarrow\quad {}^{13}\mathrm{C} + e^{+} + \nu_e \\
{}^{13}\mathrm{C} + p &\quad\rightarrow\quad {}^{14}\mathrm{N} + \gamma \\
{}^{14}\mathrm{N} + p &\quad\rightarrow\quad {}^{15}\mathrm{O} + \gamma \\
{}^{15}\mathrm{O} &\quad\rightarrow\quad {}^{15}\mathrm{N} + e^{+} + \nu_e \\
{}^{15}\mathrm{N} + p &\quad\rightarrow\quad {}^{12}\mathrm{C} + {}^{4}\mathrm{He} \\
&\quad -\mathrm{or}- \\
{}^{15}\mathrm{N} + p &\quad\rightarrow\quad {}^{16}\mathrm{O} + \gamma \\
{}^{16}\mathrm{O} + p &\quad\rightarrow\quad {}^{17}\mathrm{F} + \gamma \\
{}^{17}\mathrm{F} &\quad\rightarrow\quad {}^{17}\mathrm{O} + e^{+} + \nu_e \\
{}^{17}\mathrm{O} + p &\quad\rightarrow\quad {}^{14}\mathrm{N} + {}^{4}\mathrm{He}
\end{aligned}$$

The first six reactions is sometimes called the CN cycle, since it involves the interaction of hydrogen with carbon and nitrogen only. The net result of the CN cycle is:

$$^{12}\mathrm{C} + 4p \rightarrow ^{12}\mathrm{C} + ^{4}\mathrm{He} + 2\beta^{+} + 2\nu.$$

Although the starting point of the CN cycle is $^{12}\mathrm{C}(p,\,\gamma)^{13}\mathrm{N}$ in the above expression, any step can initiate the cycle since it is a closed cycle.

The full set of 10 reactions is called the CNO cycle. The rate of branching into the second set of reactions depends on stellar conditions. For the temperatures less than 10^8 K, however, the branching is typically about one part in 10,000 [Cla83]. At the end of the 10 reactions, helium is produced and hydrogen is consumed or burned, while a heavy nucleus (C, N, or O) acts as a catalyst.

Both the *pp* chain and CNO cycle convert hydrogen into helium. The *pp* chain can occur in any star containing hydrogen, but additional isotopes such as C, N, or O are required for the CNO cycle occurrence. A main sequence star will continue burning in this way until the hydrogen fuel in the central region has run out.

1.3 Evolving Stars

As main sequence stars burn out hydrogen fuel in the core, the region is replaced by the products of hydrogen burning processes: helium. At this stage, fusion energy is no longer produced in the core and can no longer prevent gravitational contraction, so the star contracts and hydrogen fusion resumes in the shell surrounding the core. This shell gradually expands as the hydrogen in the shell burns and helium core becomes more massive and dense due to continuing gravitational contraction. The increasing temperature in the core results in the increase in thermal pressure, so the outer regions of the star sometimes expand by a factor of 50 in its radius [Rol88]. This is the *red giant* phase of star evolution.

If the star is sufficiently massive ($M \geq 0.25 M_\odot$), the core temperature becomes high enough to ignite the helium due to the *electron degeneracy pressure* (see below), at a temperature just above 10^8 K. The first reaction in this helium burning chain is

$$^4\mathrm{He} +^4 \mathrm{He} +^4 \mathrm{He} \;\leftrightarrow\; ^{12}\mathrm{C}^*.$$

This is an exothermic reaction with an energy release of 7.275 MeV and proceeds through an excited state of $^{12}\mathrm{C}^*$ at an energy of 7.654 MeV. The decay of $^{12}\mathrm{C}^*$ by the emission of a γ-ray prevents the destruction of ^{12}C by inverse reaction of ^{12}C* to ^{8}Be and an α particle. Calculations show, however, that only one in about every 2500 excited carbon nuclei decays to the stable ground state [Cla83]. The overall effect of the two reactions is the conversion of three α particles into a carbon nucleus. The process is thus called the *triple alpha reaction*.

Once carbon nuclei have been created, further reactions consuming α particles can proceed. These reactions are:

$$\begin{aligned} {}^{12}\mathrm{C} + \alpha &\rightarrow {}^{16}\mathrm{O} + \gamma \\ {}^{16}\mathrm{O} + \alpha &\rightarrow {}^{20}\mathrm{Ne} + \gamma \end{aligned}$$

Because there is no resonance in ^{16}O near the threshold energy, not all of the carbon is consumed by α capture as soon as it is produced.

At high densities, a new form of pressure called electron degeneracy pressure becomes important in addition to gas pressure and radiation pressure. To investigate the role of the degeneracy pressure, consider a gas of electrons at absolute zero temperature. The electrons will fall into quantum states of the lowest possible energy. The electrons are packed so dense by that the Pauli principle prevents any further packing. For this reason the gas is said to be degenerate [Per03]. In a degenerate core, the thermal conductivity is extremely high since the core does not expand with increase in temperature[†]. Thus the extra energy in the core ignites helium, and thus more energy would be generated. The energy propagates throughout the core very quickly. This explosive energy flow is called the *helium flash*.

[†] In nondegenerate gas, the pressure gets larger as temperature increases. The core of the star expands as a result and would cool down. For degenerate gas, however, the gas pressure does not depend on the temperature.

Stars of relatively low mass, such as our sun, will form cores of carbon and oxygen after the helium burning process. The higher temperature of the core now will lead to helium burning in a spherical helium shell surrounding the core. The stellar envelope will expand by a factor of 50 in its radius and eventually escape to form a planetary nebula surrounding the star. The remaining core, which is mostly composed of carbon, forms a very dense, very hot object called a *white dwarf*. The energy of a white dwarf comes from gravitational contraction and leftover heat radiation.

Main sequence stars with masses 0.25 $M_\odot \leq \mathrm{M} \leq 1.4 M_\odot$ eventually become white dwarfs. The upper limit, 1.4 $M_\odot$, is the *Chandrasekhar limit*. A star with mass above this limit will experience relativistic degeneracy ($p_F \gg m_e c$, where p_F is the momentum of an electron corresponding to the Fermi energy) in the core, causing an unstable state of the core. The lower limit, 0.25 $M_\odot$, is because the evolution of stars and their emergence as white dwarfs of masses below this limit would be on a timescale much longer than the present age of the universe [Per03].

More massive stars evolve further through fusion reactions to produce successively heavier elements than carbon. A cross section of the star in this kind would have an onion-like shell structure (Figure 1.3). In every shell, different nuclear reactions are taking part and new elements are being created. The heaviest element which can be synthesized in this star is iron. If an element heavier than iron is synthesized, the element would decay into iron and smaller element ($^{56}\mathrm{Fe} + \mathrm{X} \rightarrow \mathrm{Y}^* \rightarrow {}^{56}\mathrm{Fe} + \mathrm{X}$) due to the high stability of iron.

1.4 Stellar Collapse: Type II Supernovae

A sufficiently massive star with $\mathrm{M} > 8 M_\odot$ will show very different nuclear reactions than those of an main sequence star during the late states of its evolution. The star

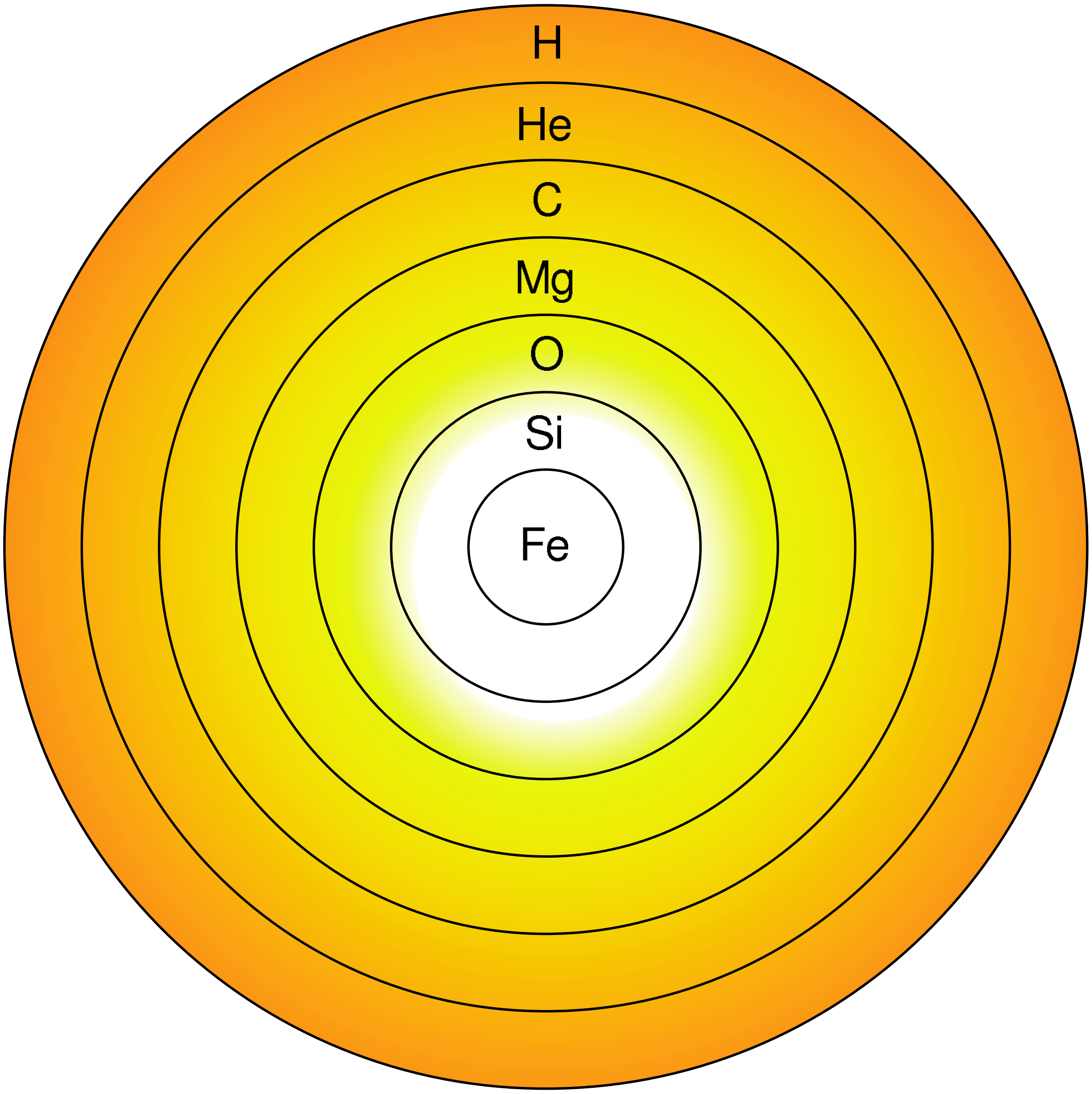

Figure 1.3: Onion-like shell structure of the core of a massive star.

can evolve through all the stages of stellar fusion until an iron core is formed via silicon burning. As more silicon is burned in the shell surrounding the iron core, both the mass of the iron core and its temperature will increase until the mass exceeds the Chandrasekhar limit [Per03]. At this stage, neutrino interactions with the nuclei play a significant role, and the neutrino processes can act as the main cooling mechanism for the core [Pad00b]. As the core of a massive star collapses gravitationally, the temperature at the core reaches very high values ($\sim$ 100 billion degrees) and becomes unstable against the collapse.

The collapse of the inner core is halted as the density of the inner core reaches roughly that of a nucleus. The repulsive nuclear force at short distances resists further compression. Consequently, the inner core material will "bounce", sending a pressure wave outwards through the in-falling matter of the outer core. This supersonic wave will give rise to the spectacular phenomenon of a Type II or core collapse supernova. Normally this leaves behind a neutron star. Depending on the mass of the star (M $> 25M_{\odot}$), however, the remnant mass after the explosion could be larger than the Chandrasekhar mass and the remnant would collapse to form a black hole.

During the supernova explosion, a series of reactions called the r-process (r for rapid) is responsible for element synthesis. The neutron capture path for the process is shown in Figure 1.4. The process can be characterized as

$$(Z, A) + n \;\rightarrow\; (Z, A+1) + \gamma.$$

If the new nucleus is stable, the process can continue with the absorption of another neutron, producing $(Z, A+2)$, and so on. At some stage in this sequence, the product from the neutron capture reaction may be unstable. If this is the case, the beta decay

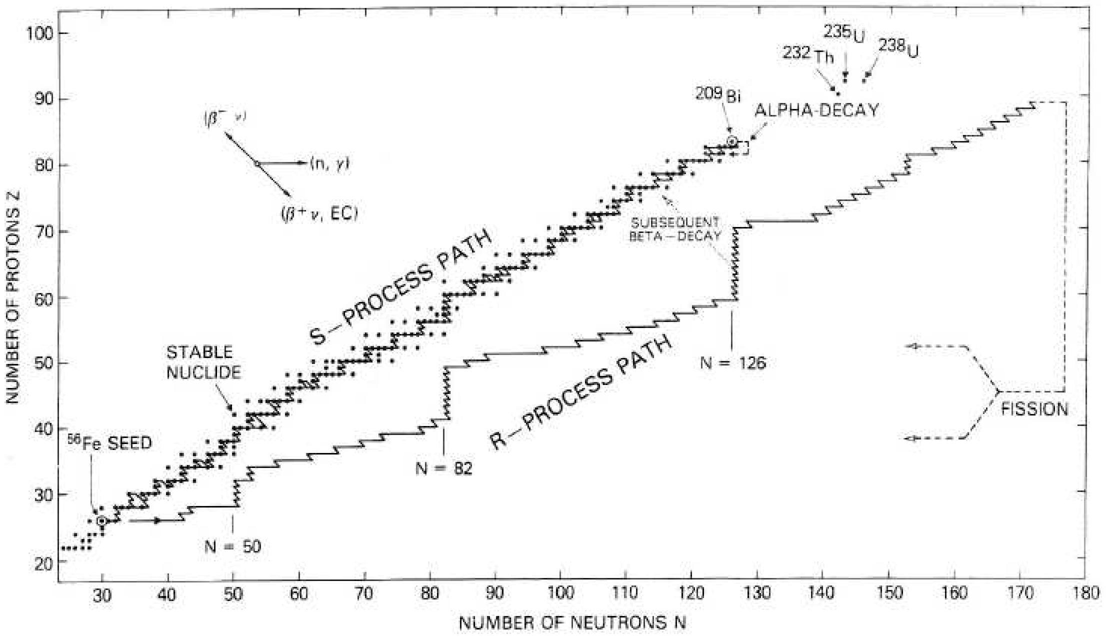

Figure 1.4: The neutron capture paths for the *s*-process and the *r*-process. Figure taken from [Rol88].

(a process converting a proton to a neutron by emitting an electron) may occur:

$$(Z, A+1) + n \;\rightarrow\; (Z+1, A+1) + e^{-} + \nu.$$

Depending on the stability of this new product, $(Z+1, A+1)$, the further evolution will be decided.

The end-point of the r-process is not known well, but it is believed to be beyond the Th-U element region. The r-process requires very high density and flux of neutrons, thus the process occurs only after the core collapse. Core collapse supernovae are likely responsible for the synthesis of neutron-rich heavy elements as shown, but they can not explain the existence of most proton-rich isotopes.

1.5 Accreting Binary Systems

Observation suggests that more the half the stars are the members of binary systems [Rol88]. If the distance between two stars that form a binary system is small enough and the radius of one of the stars becomes significantly larger during its evolution, mass may flow from the evolving star to another. This accretion leads to different astrophysical phenomena such as novae, type Ia supernovae, and X-ray bursts.

In a binary system where both stars are approximately a few solar masses initially, the more massive star reaches the red giant phase first. After losing mass the massive star becomes a hot white dwarf. When the other star evolves towards the red giant stage, the layers of this star may fill the *Roche lobe* (gravitational equipotential surface surrounding a star in a binary system) of the white dwarf, and begin to transfer mass to the hot white dwarf. An accretion disk is formed because of the angular momentum of accreting particles. The accretion rate and the mass of the primary star (white dwarf, in this case) are important quantities in characterizing novae, X-ray bursts, and type Ia supernovae. In the case of novae, roughly $(10^{-10} - 10^{-8})M_{\odot}$/year of mass is accreted onto white dwarf.

If the accreting matter is sufficiently degenerate, a strong temperature-dependent thermonuclear runaway can occur. As the temperature at the accreted envelope increases, the degeneracy is suddenly lifted, which causes an explosion involving $\sim 10^{-4}M_{\odot}$ of mass. This is a *nova explosion*, and typical nova outbursts occur at a density of $\sim 10^{3}$g/cm^{3}. During the nova explosions, the rapid proton capture process (*rp*-process) can occur. This is a sequence of proton captures and β decays that can produce heavy elements up to ^{40}Ca [Jos06].

As the accreted material is compressed and heated, the temperature can be higher than 10^{7} K and the hydrogen burning through CNO cycle can take place [Pad00b]. As the temperature rises to $\sim 10^{8}$ K, however, the beta decay of ^{13}N in CNO cycle (^{13}N$(e^{+}\nu_{e})^{13}$O) can be replaced by the proton capture reaction on ^{13}N (^{13}N$(p,\gamma)^{14}$O), and the Hot CNO cycle begins. The Hot CNO cycle is a sequence of reactions such as

$$^{12}\mathrm{C}(p,\gamma)^{13}\mathrm{N}(p,\gamma)^{14}\mathrm{O}(e^{+}\nu_{e})^{14}\mathrm{N}(p,\gamma)^{15}\mathrm{O}(e^{+}\nu_{e})^{15}\mathrm{N}(p,\alpha)^{12}\mathrm{C}.$$

At still higher temperatures and densities, a faster Hot CNO cycle or a breakout from the cycle to the *rp* process is possible since the ^{14}O$(\alpha,\, p)^{17}$F and ^{15}O$(\alpha,\, \gamma)^{19}$Ne reaction rates will become large enough for the cycle to bypass the beta decays of ^{14}O and ^{15}O [Utk98]. ^{18}F then can be produced either by ^{14}O$(\alpha,\, p)^{17}$F$(p,\gamma)^{18}$Ne$(e^{+}\nu_{e})^{18}$F or by ^{16}O(p,γ) ^{17}F$(p,\gamma)^{18}$Ne$(e^{+}\nu_{e})^{18}$F in novae. The second sequence is also possible due to high ^{16}O abundance on the surface of a white dwarf.

The γ-ray emission from novae during the first several hours of the expansion is dominated by positron annihilation resulting from the beta decay of radioactive

^{18}F nuclei in the expanding envelope [Coc00, Her99]. The decay of ^{18}F is the most important positron annihilation source during this time because of its relatively long half-life (110 min) and large production rate. The observation of ^{18}F γ-rays is one of the most promising mechanisms for constraining nova models. Since ^{18}F is destroyed predominantly by the ^{18}F(p, α)^{15}O reaction, the reaction is very important in understanding nova phenomena.

X-ray bursts are thought to consist of a neutron star and a high-mass ($\geq 15 M_\odot$) companion. Similar to novae, X-ray bursts can be characterized by the mass of the neutron star and the accretion rate of $(10^{-10} - 10^{-8}) M_\odot$/year. The thermonuclear reaction mechanism for X-ray bursts is similar to that of a nova. X-ray bursts involve high density ($\sim 10^6$g/cm^3) and high temperature ($\sim 10^9$ K), and thus the end point of *rp* process is a closed cycle in the Sn-Te region (SnSbTe cycle) [Sch01].

Chapter 2

Introduction

2.1 Reaction Rate Formalism

2.1.1 Stellar Reaction Rates

The probability that a particular nuclear reaction will take place is proportional to the "geometrical area" of the interacting nuclei. This probability also depends on the center-of-mass energy (or relative velocity v) of the projectile-target pair, and is expressed as a nuclear cross section, $\sigma(v)$, of a particular reaction. If two different species of nuclei x and y have number densities N_x and N_y with relative velocity v, the rate at which nuclear reaction occur is defined as [Cla83]

$$r_{xy} = N_x N_y v \sigma(v). \tag{2.1}$$

At a given temperature T in a star, the relative velocity of the particles varies over a wide range of values (given by the probability function $\phi(v, T)$), and thus the reaction rate can be expressed as

$$r_{xy}(T) = N_x N_y \int_0^\infty \phi(v,T) v\sigma(v) dv, \tag{2.2}$$

where

$$\phi(v,T) = 4\pi v^2 \left(\frac{\mu}{2\pi kT}\right)^{3/2} \exp\left(-\frac{\mu v^2}{2kT}\right),$$

$$\int_0^\infty \phi(v,T) dv = 1.$$

Since the reaction rate depends linearly on the densities of interacting particles, one often considers the probability for only one pair of particles at a stellar temperature T, $< \sigma v >$:

$$\begin{aligned} < \sigma v > &= \int_0^\infty \phi(v,T) v\sigma(v) dv \\ &= \left(\frac{8}{\pi\mu}\right)^{1/2} \frac{1}{(kT)^{3/2}} \int_0^\infty \sigma(E) E \exp\left(-\frac{E}{kT}\right) dE. \end{aligned} \tag{2.3}$$

In the above expressions, μ is the reduced mass of the interacting particles in amu, k is the Boltzmann constant, and E is the center-of-mass energy. The quantity $< \sigma v >$ is a thermal average over the Maxwell-Boltzmann distribution of the product of the reaction cross section and the relative velocity of the reactants, and is a function of the temperature of the system [Rol88].

In stellar environments, reactions are hampered by the Coulomb barrier between the colliding charged particles

$$V_C = \frac{Z_x Z_y e^2}{r}. \tag{2.4}$$

Eq.(2.4) assumes no relative motion between the interacting two particles (orbital angular momentum $l = 0$, s-wave). For non-zero angular momentum, an additional term should be added to Eq.(2.4):

$$V_{eff} = V_C + V_l = \frac{Z_x Z_y e^2}{r} + \frac{l(l+1)\hbar^2}{2\mu r}. \tag{2.5}$$

The effective Coulomb barrier as a function of r and l is shown in Figure 2.1.

Assuming $E_C \gg E$, the probability for s-waves to penetrate the barrier may be expressed as

$$P(E) \propto \exp(-2\pi\eta), \tag{2.6}$$

where the dimensionless Sommerfeld parameter η is defined by

$$\eta = \frac{Z_x Z_y e^2}{\hbar v}. \tag{2.7}$$

The astrophysical S-factor ($S(E)$), which represents the nuclear part of the probability for the occurrence of a nuclear reaction, then can be defined by dividing out the dominant energy-dependent factors in $\sigma(E)$: the "size" of the nucleus $\lambda\!\!\!{}^{-2} \sim 1/E$ and the $l = 0$, s-wave Coulomb penetrability $\exp(-2\pi\eta)$

$$\sigma(E) = \frac{1}{E}\exp(-2\pi\eta)S(E). \tag{2.8}$$

Since the two strongly energy-dependent terms in the cross section $\sigma(E)$ are factored out, $S(E)$ is a more smoothly varying function of energy that is much more readily extrapolated to low energies than $\sigma(E)$ [Cla83]. Inserting Eq.(2.8) into Eq.(2.3), the reaction rate per particle pair becomes

$$<\sigma v>= \left(\frac{8}{\pi\mu}\right)^{1/2} \frac{1}{(kT)^{3/2}} \int_0^\infty S(E)\exp\left(-\frac{E}{kT} - \frac{b}{E^{1/2}}\right) dE, \tag{2.9}$$

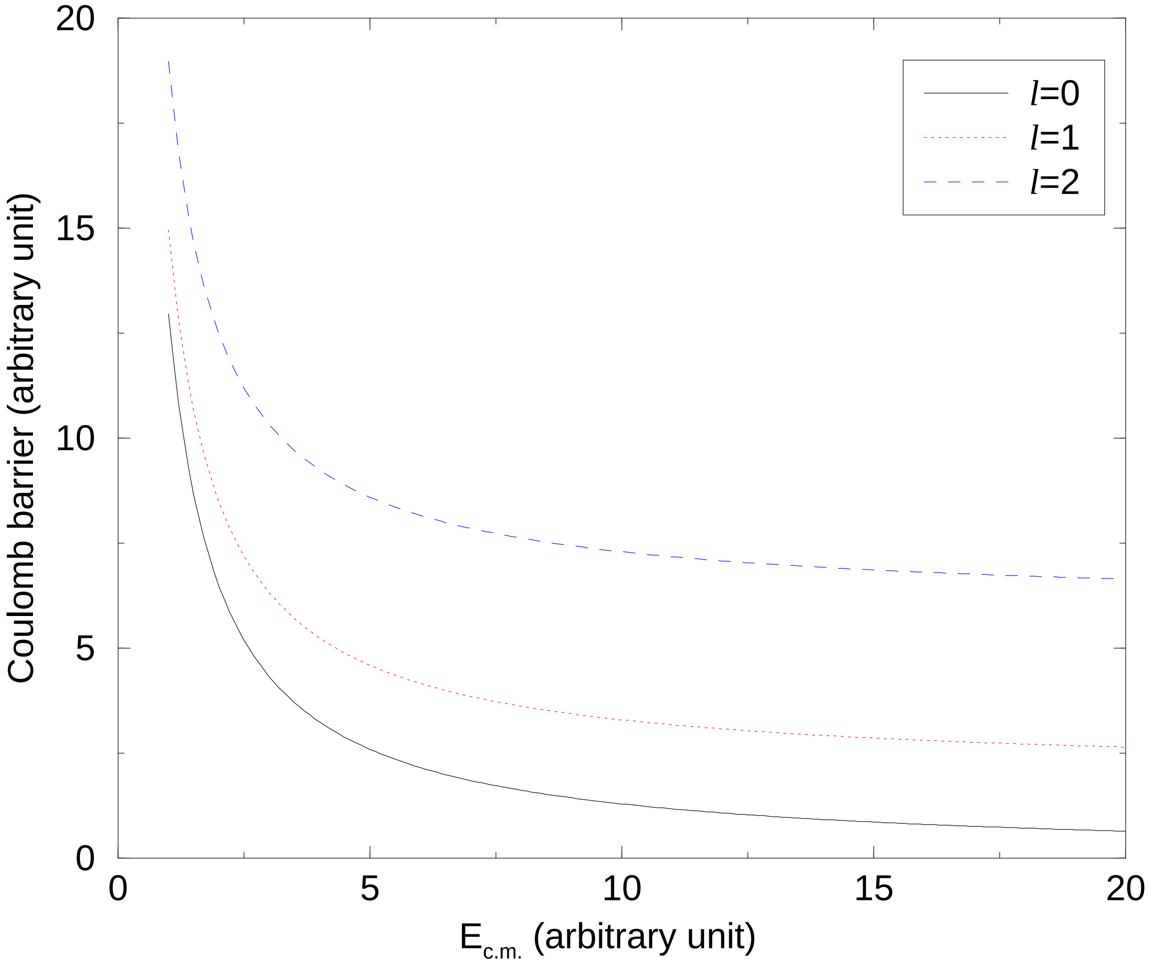

Figure 2.1: The effective Coulomb barrier functions for several l values.

where the quantity b is given by $(2\mu)^{1/2}\pi e^2 Z_x Z_y/\hbar$, and b^2 is called the Gamow energy.

Since the first factor in the exponent, which arises from the Maxwell-Boltzmann velocity distribution, decreases rapidly with energy, while the second increases rapidly with energy, the product

$$\exp\left(-\frac{E}{kT}-\frac{b}{E^{1/2}}\right)$$

is strongly localized in energy. By taking the first derivative of this expression and setting it to zero, one can find that the maximum of the peak is at

$$E_0=\left(\frac{bkT}{2}\right)^{2/3}=1.22\left(Z_x^2 Z_y^2 \mu T_6^2\right)^{1/3}\text{keV}, \tag{2.10}$$

where T_6 is the temperature in units of 10^6 K. The full width of the Gamow peak can be approximated by a Gaussian distribution:

$$\Delta=\frac{4}{\sqrt{3}}\sqrt{E_0 kT}=0.75\left(Z_x^2 Z_y^2 \mu T_6^5\right)^{1/6}\text{keV}. \tag{2.11}$$

Since the Gamow peak decreases rapidly outside of the Gamow window, $E_0 \pm \Delta$, the reaction rate is strongly dependent on the S-factor (equivalently, cross section) in the window. The determination of the reaction rates is, therefore, reduced to determining the energy dependent cross section in or near the Gamow window. The Gamow window for the ^{18}F + p system is shown in Figure 2.2 for a stellar temperature of T_9=0.1.

In the absence of resonances, the astrophysical S-factor $S(E)$ is nearly a constant over the window

$$S(E)=S(E_0)=\text{constant}, \tag{2.12}$$

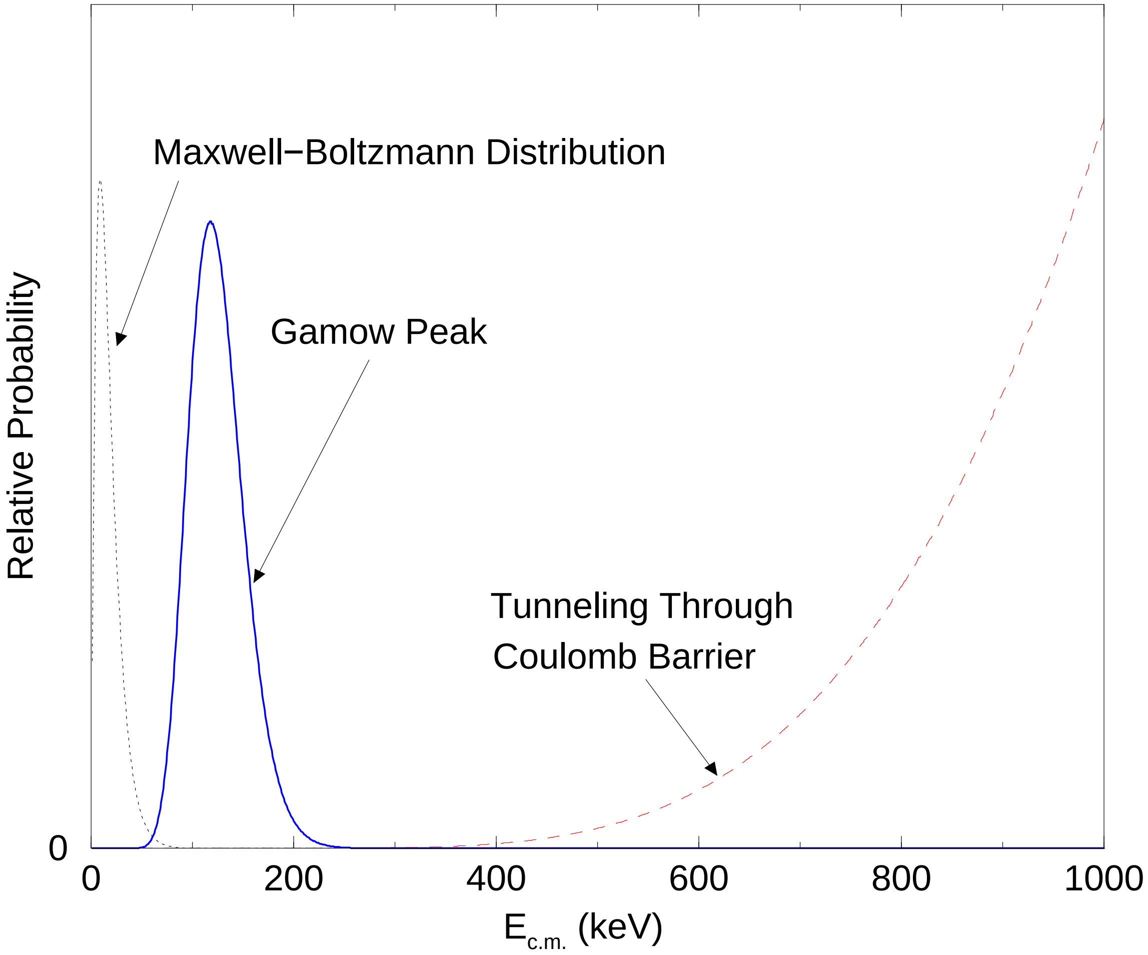

Figure 2.2: The Gamow window for the ^{18}F + p system for a stellar temperature of T_9=0.1.

and Eq.(2.9) reduces to

$$< \sigma v >= \left(\frac{8}{\pi\mu}\right)^{1/2} \frac{1}{(kT)^{3/2}} S(E_0) \int_0^{\infty} \exp\left(-\frac{E}{kT} - \frac{b}{E^{1/2}}\right) dE. \tag{2.13}$$

The exponential term in the integrand of Eq.(2.13) can be approximated by a Gaussian function

$$\exp\left(-\frac{E}{kT} - \frac{b}{E^{1/2}}\right) \propto \exp\left[-\left(\frac{E - E_0}{\Delta/2}\right)^2\right], \tag{2.14}$$

giving for a non-resonant reaction rate:

$$< \sigma v >= \left(\frac{2}{\mu}\right)^{1/2} \frac{\Delta}{(kT)^{3/2}} S(E_0) \exp\left(-\frac{3E_0}{kT}\right), \tag{2.15}$$

where Δ is defined in Eq.(2.11). This expression is useful when no resonant level exists.

2.1.2 Resonant Reactions

The reaction rate expression, Eq.(2.3), relies on the smoothly varying S-factor with energy for non-resonant reactions. In many cases, however, the reaction rate is dominated by resonances when the two nuclei x and y fuse into an excited state of a compound nucleus, which then decays into the product particles. If the incident energy is such that the wavefunctions of the incident particle and the compound state have a significant overlap (the sum of the Q-value for the reaction and the center of mass resonance energy E_R is close to the energy E_x of the excited state in the compound nucleus), the cross section for reaction is greatly enhanced.

The nuclear cross section for a resonant reaction can be expressed in the Breit-Wigner form:

$$\sigma_{BW}(E) = \pi\lambda\!\!\!^{-2}\frac{2J+1}{(2J_x+1)(2J_y+1)}(1+\delta_{xy})\frac{\Gamma_a\Gamma_b}{(E-E_R)^2+(\Gamma/2)^2}, \tag{2.16}$$

where J, J_x, J_y are the spins of the resonance and the two interacting particles, $\lambda\!\!\!^{-2} = \hbar^2/2\mu E$, and Γ_a, Γ_b, Γ are the partial widths of the entrance, exit channels and the total width, respectively. If Eq.(2.16) is inserted into Eq.(2.3), we can obtain the following expression for the reaction rate through a single resonance:

$$< \sigma v >= \left(\frac{8}{\pi\mu}\right)^{1/2}\frac{1}{(kT)^{3/2}}\int_0^\infty \frac{\lambda\!\!\!^{-2}}{4\pi}\frac{\omega E\Gamma_a\Gamma_b}{(E-E_R)^2+(\Gamma/2)^2}\exp\left(-\frac{E_R}{kT}\right)dE. \tag{2.17}$$

where ω is the spin-statistical factor $\omega = \frac{2J+1}{(2J_x+1)(2J_y+1)}$. For a narrow resonance (typically $\Gamma/E_R < 10\%$) with $\lambda\!\!\!^{-2} \simeq \hbar^2/2\mu E_R$ and with negligible energy dependence of the partial and total widths, this expression reduces to

$$< \sigma v >= \left(\frac{2\pi}{\mu kT}\right)^{3/2}\hbar^2(\omega\gamma)_R\exp\left(-\frac{E_R}{kT}\right), \tag{2.18}$$

where $(\omega\gamma)_R$ is the strength of a resonance:

$$(\omega\gamma)_R = \frac{2J_R+1}{(2J_a+1)(2J_b+1)}\frac{\Gamma_a\Gamma_b}{\Gamma_R}. \tag{2.19}$$

A narrow resonance has the specific property of acting like a δ-function in the reaction rate integral.

In the presence of several narrow, isolated resonances that are not interacting with each other, this reaction rate can be generalized to

$$< \sigma v >= \left(\frac{2\pi}{\mu kT}\right)^{3/2} \hbar^2 \sum_i (\omega\gamma)_i \exp\left(-\frac{E_i}{kT}\right). \tag{2.20}$$

For broad resonances, however, explicit knowledge of the energy dependence of the partial widths is required to calculate the reaction rate. This can be done by parameterizing the widths in terms of the reduced widths θ_l^2:

$$\Gamma_l(E) = \frac{2\hbar}{R_n}\left(\frac{2E}{\mu}\right)^{1/2} P_l(E, R_n)\theta_l^2, \tag{2.21}$$

where Γ_l is the partial width in the relevant reaction channel for the l^{th} partial wave, R_n is the nuclear radius, and P_l is the penetrability:

$$P_l = \frac{1}{F_l^2(E, R_n) + G_l^2(E, R_n)}. \tag{2.22}$$

F_l and G_l are the regular and irregular solutions to the Coulomb wavefunction for a given relative orbital angular momentum, l.

2.2 R-Matrix Theory

The **R**-matrix formalism is a parameterization of the properties of compound nucleus reactions. For a short-range potential there exist *quasi-bound* or *virtual single particle states* which have positive energy. A simplified picture of the formation of the compound nucleus is that the projectile with positive energy is momentarily trapped in one of the quasi-bound states. A given compound nucleus may decay in a variety of different ways, and essential to the compound nucleus model of nuclear reactions is the assumption that the relative probability for decay into any specific set of final products is independent of the means of formation of the compound nucleus. The decay probability depends only on the total energy given to the system; in effect, the compound nucleus “forgets” the process of formation and decays governed primarily by statistical rules [Kra87].

The formulation of **R**-matrix theory begins with the idea of a *nuclear surface* which defines the volume within which nucleons are considered part of a compound nucleus. Because of the short range of nuclear forces, we can choose the compound nucleus surface S so that all the nuclear interactions take place only within V, which is the volume enclosed by S [Vog62]. The regions outside the nuclear surface are referred to as distinct reaction *channels*. In this region, the nuclear forces between particles are extremely weak. The only contributing forces to the particles in the external region are electromagnetic. The particle system is described as a superposition of incoming and outgoing waves in this region [Rui03].

Before we discuss the formalism of **R**-matrix theory, it is useful to introduce the concept of the configuration space of all A nucleons. Corresponding to the three spatial degrees of freedom of each particle, this space has $3A$ dimensions. There is a certain region, called the *internal region* by Wigner and Eisenbud, corresponding to all nucleons being close together in a volume of nuclear dimensions in physical space. Certain other regions, called *channels* by Breit [Bre40], corresponds to the nucleons being separated into two groups, say A_1 and A_2, in physical space beyond *interaction radius*, $a_\alpha = r_0(A_1^{1/3} + A_2^{1/3})$. All the rest of configuration space corresponds to physical space which occur with negligible probability [Lan58].

The following discussion follows mainly the formalism of Refs. [Lan58], [Vog59], and [Rui03].

2.2.1 Form of the Wave Functions and R-function

In order to describe the formal procedure employed in the **R**-matrix theory, we consider the simplest case of potential scattering for spinless particles with only the elastic scattering channel being open. For a spinless $l = 0$ particle scattering from a central potential, we may show the wavefunction of the internal region satisfies the radial Schrödinger equation:

$$-\frac{\hbar^2}{2m}\frac{d^2\psi}{dr^2} + V(r) = E\psi \tag{2.23}$$

where

$$\begin{aligned} V(r) &= -V_1 & \qquad\qquad r \le R_a \\ &= 0 & \qquad\qquad r > R_a \end{aligned}$$

and R_a is the radius of nuclear surface. The wavefunction has to be regular at the origin so that inside the potential well we have

$$\psi = A \sin Kr \qquad\qquad r < R_a, \tag{2.24}$$

where A is a normalization constant and K is the wave number inside the well, $K^2 = 2m/\hbar^2(E + V_1)$. Outside the well, the wave function is a linear combination of incoming waves and outgoing waves.

In reality, however, the compound nuclear decays, and therefore does not have well defined energies. A wavefunction ψ may be expanded in terms of a complete set of stationary states, X_λ:

$$\psi = \sum_\lambda A_\lambda X_\lambda. \tag{2.25}$$

The energy-dependent expansion coefficients A_λ are

$$A_\lambda = \int_V X_\lambda^* \psi dV. \tag{2.26}$$

These stationary states satisfy the Hamiltonian equation $HX_\lambda = E_\lambda X_\lambda$, where E_λ are the energy eigenvalues of the system and X_λ are the eigenvectors. Furthermore, the states also satisfy the orthonormal condition $\int_V X_{\lambda'} X_\lambda dV = \delta_{\lambda'\lambda}$, so that they are the "basis" of the system. The boundary condition at the nuclear surface $r = R_a$ is required to make sure that these states relate directly to the actual quasi-stationary states:

$$\frac{dX_\lambda}{dr} + bX_\lambda|_{r=R_a} = 0, \tag{2.27}$$

where b is a boundary constant.

By substitution and integration, we can obtain

$$-\frac{\hbar^2}{2m}\left(\psi\frac{dX_\lambda}{dr} + X_\lambda\frac{d\psi}{dr}\right)_{r=R_a} = (E - E_\lambda)\int_0^{R_a} X_\lambda \psi dr. \tag{2.28}$$

Combining all the equations from Eq.(2.26) to Eq.(2.28) gives

$$A_\lambda = -\frac{\hbar^2}{2m}X_\lambda(R_a)\frac{\psi'(R_a) + b\psi(R_a)}{E - E_\lambda}, \tag{2.29}$$

and thus Eq.(2.25) becomes

$$\psi(r) = G(r, R_a)\left(\psi'(R_a) + b\psi(R_a)\right), \tag{2.30}$$

where $G(r, R_a)$ is the Green's function, given by

$$G(r, R_a) = -\frac{\hbar^2}{2m} \sum_{\lambda} \frac{X_\lambda(r) X_\lambda(R_a)}{E_\lambda - E}, \tag{2.31}$$

which relates the value of the wave function in the internal region to its derivative on the surface [Boh37]. The R-function is defined as the value of the Green's function at $r = R_a$:

$$R \equiv G(R_a, R_a) = \frac{\hbar^2}{2m} \sum_{\lambda} \frac{X_\lambda^2(R_a)}{E_\lambda - E} = \sum_{\lambda} \frac{\gamma_\lambda^2}{E_\lambda - E}, \tag{2.32}$$

where γ_λ is the reduced-width amplitude such that $\gamma_\lambda^2 = (\hbar^2/2m)|X_\lambda|^2$. The R-function is then related to the logarithmic derivative of the wavefunction by

$$\frac{\psi'(R_a)}{\psi(R_a)} = \frac{1 - bR}{R}. \tag{2.33}$$

Therefore, knowing the logarithmic derivative of the wavefunction at point $r = R_a$ for all energies is equivalent to knowing the cross section for all energies [Vog59].

As mentioned earlier, the total wavefunction in the external region can be written as a superposition of the incoming and outgoing waves, I and O respectively:

$$\Psi_l = I_l - U_l O_l \tag{2.34}$$

where l represents the incident orbital angular momentum and U_l is the *collision function.* It is obvious then the coefficient U_l is the amplitude of the unit-flux outgoing wave O_l which is associated with a unit-flux incoming wave I_l.

The collision function U_l may be expressed in terms of the R-function by equating the logarithmic derivatives of the internal and external wave functions at $r = R_a$:

$$U_l = \exp(2i\delta_l), \tag{2.35}$$

where

$$\delta_l = \tan^{-1}\left[R_l P_l/(1 - R_l P_l)\right] - \phi_l \tag{2.36}$$

is a *phase shift.* ϕ_l, P_l, and S_l are the hard sphere scattering phase shift, penetrability, and energy shift function, respectively, and are given by

$$\phi_l = \tan^{-1}(F_l/G_l) \tag{2.37}$$

$$P_l = kr/(F_l^2 + G_l^2)|_{r=R_a} \tag{2.38}$$

$$S_l = P_l(F_l F_l' + G_l G_l'). \tag{2.39}$$

In order to obtain an expression for the differential scattering cross section in terms of the U_l, one forms the following expression for the *nuclear scattering amplitude* which can be constructed by manipulating incident and outgoing wave equations of unit flux and using Eq.(2.34):

$$A(\theta) = \frac{1}{2} i k^{-1} \sum_l (2l+1)(1 - U_l) P_l(\cos\theta), \tag{2.40}$$

where $P_l(\cos\theta)$ is the Legendre polynomial. The differential cross section for elastic scattering of spinless particles by a central potential is then given by

$$\frac{d\sigma(\theta)}{d\Omega} = |A(\theta)|^2 = \frac{1}{4} k^{-2} \left| \sum_l (2l+1)(1 - U_l) P_l(\cos\theta) \right|^2 . \tag{2.41}$$

2.2.2 R-Matrix in the Multi-Channel Case and Interference Effects

The considerations in the previous section can be immediately generalized to take account of the occurrence of spins and reaction channels. At this point, it is convenient to introduce matrix notation and a corresponding set of indices. The indices are the set $c = \{\alpha s \nu l m\}$, which denote channel, channel spin, channel spin component, orbital angular momentum, and orbital angular momentum component, respectively. Since each reaction channel is uniquely defined by these five indices, they can be grouped together under the index c.

The fundamental relation of the **R**-matrix theory is the multi-channel generalization of Eq.(2.32). Such a relation is used to determine the collision matrix **U** just as Eq.(2.32) was used to determine the collision function U in the single-channel case. This relation may be derived by means of Green's theorem. Then, the R-function becomes the **R**-matrix, whose elements are expressed as

$$R_{cc'} = \sum_{\lambda} \frac{\gamma_{\lambda c}\gamma_{\lambda c'}}{E_{\lambda} - E}. \tag{2.42}$$

where the unprimed and primed indices represent the corresponding values of entrance and exit channels respectively. Similarly, the collision function U becomes the collision matrix **U** [Vog62]:

$$U_{cc'} = (k_c r_c)^{1/2} O_c^{-1} \left[(1 - \mathbf{RL})^{-1} (1 - \mathbf{RL}^*) \right]_{cc'} I_{c'} (k_{c'} r_{c'})^{-1/2}, \tag{2.43}$$

Here **L** is the diagonal matrix whose components are given by $L_c = S_c - B_c + iP_c$, where B_c is the matrix form of the boundary constant. Before deriving the form of the total cross section for multi-channel cases from the above equations, it is worthwhile to consider the treatment of isolated levels in **R**-matrix theory first.

The occurrence of sharp resonance peaks in the excitation curves of low-energy nuclear reactions is one of the most striking phenomena encountered in the **R**-matrix theory. Many of these levels have been fitted with the famous Breit-Wigner one-level resonance formula (Eq.(2.16)), which is an unsatisfactory situation when there is an interference effect between two isolated resonances. With the advent of the rigorous **R**-matrix theory, the difficulty can be largely resolved. In this theory, the corrections to the one-level formula appear explicitly when the general theory is approximated to the one-level case. The familiar condition for the validity of the one-level formula is that the level width Γ should be much less than the level spacings D. The advantage of having **R**-matrix theory comes when the condition is not well satisfied so that other levels may influence the cross section near a peak. In such cases the **R**-matrix theory can give explicit modifications to the one-level formula in terms of parameters representing the presence of the other levels. With these extra parameters, one has more freedom in fitting so that a poor fit obtained with a one-level formula may be improved.

When $\Gamma/D \ll 1$, it is possible to obtain an approximate expansion for $\mathbf{U}$ in terms of the levels of the system [Bet37], and thus the corresponding cross sections of the reactions can be written as:

$$\sigma_{\alpha\alpha'} = \frac{\pi}{k_\alpha^2} \sum_{Jsls'l'} g_J \left| \sum_\lambda \frac{\Gamma_{\lambda c}^{1/2} \Gamma_{\lambda c'}^{1/2}}{E_\lambda + \Delta_\lambda - E - \frac{i}{2}\Gamma_\lambda} \right|^2 , \tag{2.44}$$

where k_α is the wave number, E_λ is the resonance energy, Γ_λ is the level width, Δ_λ is the level shift, and g_J is the spin statistical factor:

$$g_J = \frac{2J+1}{(2J_1+1)(2J_2+1)}. \tag{2.45}$$

The sum over λ in Eq.(2.44) is over levels of given spin J and parity. The individual reduced width amplitudes, and thus the partial widths as well, are equally likely to be positive or negative [Fre65, Lan58].

For levels with the same J^π value, the astrophysical S-factor due to those levels can be taken from Eq.(2.44), and expressed as

$$S_{tot} = \left| \sum_j \pm\sqrt{S_j} e^{i\delta_j} \right|^2, \tag{2.46}$$

where j is the resonance index, S_j is the S-factor from the resonance with index j, and δ_j is the phase [$\tan(\delta_j)=\Gamma/(2(\mathrm{E}_j\text{-}\mathrm{E}))$]. Each term in this sum can have either positive or negative signs, as mentioned earlier, and this ambiguity results in the observed interference in the cross section.

In summary, the cross section is enhanced when the incident wavefunction matches the internal wavefunction; That is, when the energy of the incident particle is closely matched to that of the physical state. This appears as a resonance in the cross section, whose resonant energy corresponds to the physical energy of the compound nuclear state. The **R**-matrix formalism provides a complete description of scattering cross sections of resonant reactions in cases where one or more nuclear states can be formed in the compound nucleus via a variety of different mechanisms. One point that **R**-matrix theory takes into account, which a simple Breit-Wigner resonance does not, is that neighboring resonances can interfere with each other leading to phase shift modification as shown in Eq.(2.44).

2.3 Background Considerations

2.3.1 Three-Body Continuum (Sequential Decay)

When the projectile picks up a light particle (e.g. nucleon), the projectile may lose some portion of energy by forming an intermediate state. Normally these states are very unstable [Boh85], and thus subsequently decay by particle emission. Since the two-step process yields three particles (or more) in the final channel, and gives a continuous energy distribution, the process produces a *three-body continuum.* The continuous energy distribution is the result of incomplete reconstruction of the kinematics [Boh01]: The recoil of the emitted particle shifts the energy of the outgoing fragment depending on the emission angle, which causes the broad energy distribution.

It is thus crucial to understand the mechanisms of the de-excitation process in order to obtain reliable information on the primary reaction. An example of a three-body continuum process is

$$\begin{array}{rl} {}^{7}\mathrm{Be} + d \rightarrow {}^{5}\mathrm{Li} + & {}^{4}\mathrm{He}^{*} \\ & \Downarrow \\ & t + p \end{array}$$

The process consists of two successive steps, each of which can be considered to be two-body reaction: (i) the deuteron, d, from ^{7}Be is picked up by a ^{2}H component of the target forming an unbound state of the ^{4}He, and (ii) the intermediate, unstable ^{4}He* fragment decays to a proton and a triton.

For the ^{7}Be + d system, there are several possibilities for the sequential break-up that give a triton in the exit channel:

$$^7\mathrm{Be} + d \Rightarrow \begin{cases} t +^6\mathrm{Be} & & & (1) \quad \text{direct two-body reaction} \\ ^3\mathrm{He} +^6\mathrm{Li}^* & = & ^3\mathrm{He} + t +^3\mathrm{He} & (2) \\ ^3\mathrm{Li} +^6\mathrm{He}^* & = & ^3\mathrm{Li} + t + t & (3) \\ ^4\mathrm{Li} +^5\mathrm{He}^* & = & ^4\mathrm{Li} + t + d & (4) \\ ^4\mathrm{He} +^5\mathrm{Li}^* & = & ^4\mathrm{He} + t + p + p & (5) \\ ^5\mathrm{Li} +^4\mathrm{He}^* & = & ^5\mathrm{Li} + t + p & (6) \end{cases}$$

Expression (1) is not one of the sequential break-ups, but the direct two-body reaction. The expression is shown for comparison purpose. The expressions from (2) to (6) can be summarized as

$$A + a \rightarrow B + b^* \rightarrow B + x + t,$$

where $b = x + t$, and x is a light pick-up particle. The triton, t, comes from the two major mechanisms in this case (the direct two-body reaction and the sequential break-ups). A knowledge of the sequential break-ups is required, therefore, to understand the ^{7}Be(d, t)^{6}Be reaction. The reactions labeled (2), (3), and (4) are not possible due to the kinematics. For instance, the reaction (2) is not possible since a 100 MeV ^{7}Be beam would populate ^{6}Li* with at most $E_x = 12$ MeV, which is below the ^{3}He + ^{3}He threshold. The only reactions that have been studied are, therefore, expressions (5) and (6).

When several decay channels are open, the competition between different particle decay channels can be approximated as [Bod62, Hil79]

$$\frac{\Gamma_2}{\Gamma_1} = \frac{(2s_2+1)m_2\sigma_2^0}{(2s_1+1)m_1\sigma_1^0} \exp\left[\frac{(S_1 - S_2) + (V_1' - V_2')}{T}\right], \tag{2.47}$$

where $i = 1, 2$ is the channel index, Γ_i, s_i, m_i, σ_i^0, S_i, V_i', and T are the decay width, spin, mass, inverse capture cross section, separation energy, effective Coulomb barrier, and the average temperature, respectively.

The energy of the emitted nucleus, t, is given by [Boh85, Ada87]

$$E_t^{'} = \frac{t}{b}E_b + \frac{x}{b}\varepsilon + 2\sqrt{\frac{tx}{b^2}E_b\varepsilon}\cos\theta_x, \tag{2.48}$$

where t, b, and x are the masses of the corresponding particles, E_b is the kinetic energy of b calculated for the two-body reaction $A(a,b)B$, θ_x is the emission angle of x with respect to the direction of b in the rest frame of b. $\varepsilon = E_b^* - E_{t'}^* - S_{bx}$ is the decay energy in $b \rightarrow t + x$ with

E_b^* the excitation energy of b

$E_{t'}^*$ the excitation energy of t after emission of x

S_{bx} the separation energy of x in $b = t + x$.

Particle emission decreases the kinetic energy of fragment b and causes an energy broadening, even if b is monoenergetic. The triton angle is also shifted according to $\theta_{t'} = \theta_b - \Delta\theta$, where

$$\Delta\theta = \sqrt{\frac{x}{t}\frac{\varepsilon}{E_b}}\sin\theta_x\left[1 + \sqrt{\frac{x}{t}\frac{\varepsilon}{E_b}}\cos\theta_x\right]^{-1}. \tag{2.49}$$

The energy spectrum for the triton in the pick-up and decay process is expressed as [Boh85]

$$\frac{d^2\sigma}{d\Omega_t dE_t} = \int_0^\infty \int_0^\pi \frac{d^2\sigma}{d\Omega_b dE_b}(\theta_b, E_b^*)\frac{\sin\theta_b}{\sin\theta_t}\Gamma_{bx}W_x(\Omega_b, \Omega_x)\frac{d\theta_x}{d\varepsilon}\sin\theta_x d\phi_x d\varepsilon. \tag{2.50}$$

The first term includes all the information about forming the intermediate state, such as the angular distribution, the Q-value dependence, etc. The term can be approximately factorized as

$$\frac{d^2\sigma}{d\Omega_b dE_b} = C_1 \exp\left(-C_2\theta_b\right) \exp\left[-\left(\frac{E_x - C_3}{C_4}\right)\right]. \tag{2.51}$$

Here, the angular dependence of the distribution is approximated with an exponential decay and the Q-value dependence is described by a Gaussian distribution.

The second term in the exponent of Eq.(2.50), $\sin\theta_b/\sin\theta_a$, transforms the solid angle of b into that of a. Γ_{bx} is the branching ratio of the channel $b \rightarrow t + x$, and $W_x(\Omega_b, \Omega_x)$ is the correlation function for the emission of x into the angles θ_x, ϕ_x with respect to θ_b, ϕ_b. Thus, if we assume an isotropic emission in the c.m. system of particle b, this function becomes 1.

2.3.2 Phase Space Model

The Phase Space Model (PSM) was originally developed by Enrico Fermi in order to investigate phenomena in which two colliding nucleons may give rise to several π-mesons and some anti-nucleons [Fer50]. When two nucleons collide with high energy in their center of mass system, the energy will be released in a relatively small region surrounding the two nucleons. The entire volume will be occupied by the nucleons and the surrounding pion field so that the space is loaded with large amount of energy [Fer50]. Since the interactions of the pion field are strong, one may expect that the energy will be distributed among the various degrees of freedom present in the volume according to statistical laws. The purpose of the PSM is, thus, computing statistically the probability of pion creation with a given energy distribution. As the wave function plays a central role in Schrödinger picture, the phase space distribution is the starting point in the phase space picture of quantum mechanics [Nou98].

First order perturbation theory gives for the cross section

$$\sigma = \frac{2\pi}{\hbar} \frac{|T_{if}|^2}{|\text{flux}|} w, \tag{2.52}$$

where T_{if} is the matrix element for the transition from the initial state i to a final state f, and w is the density of states [Del83]. Fermi proposed to replace $|T_{if}|^2$ by a constant when a statistical equilibrium is reached. This is the so-called phase space model or statistical model.

In the PSM, there is only one adjustable parameter: the volume Ω, in which the energy of the two colliding nucleons is dumped. Since the strong field surrounding the nucleons extends to a distance of the order of $\hbar/\mu c$, where μ is the mass, the volume Ω is expected to have this order of magnitude [Fer50]. Therefore, the form of Ω is

$$\begin{aligned} \Omega &= \Omega_0 A & (2.53) \\ &= \frac{4\pi R^3}{3} A, & (2.54) \end{aligned}$$

where R is the radius of the volume ($R = \hbar/\mu c = 1.4 \times 10^{-13}$ cm), and A is the Lorentz contraction. The term A is required only the two interacting nucleons have relatively large energies. The assumption of statistical equilibrium is such that $|T_{if}|^2$ in Eq.(2.55) is proportional to the probability that all particles are confined inside Ω.

If there are n-bodies in the exit channel, the phase space distribution for particle i in the center of mass system is [End05]

$$P_i^{\text{c.m.}}(\mu, E, E') = C_n \sqrt{E'} \left(E_i^{\max} - E'\right)^{\frac{3n}{2}-4}, \tag{2.55}$$

where E is the incident energy, E' is the energy of the product emitted with $\cos\mu$, $E_i^{\max}$ is the maximum possible center of mass energy for particle i, and C_n are normalization constants:

$$\begin{aligned} C_3 &= \frac{4}{\pi(E_i^{\max})^2} && (2.56) \\ C_4 &= \frac{105}{32(E_i^{\max})^{7/2}} && (2.57) \\ C_5 &= \frac{256}{14\pi(E_i^{\max})^5}. && (2.58) \end{aligned}$$

In the laboratory system, the expression becomes

$$P_i^{\mathrm{lab}}(\mu, E, E') = C_n\sqrt{E'}\left[E_i^{\max} - \left(E^* + E' - 2\mu\sqrt{E^*E'}\right)\right]^{\frac{3n}{2}-4}, \tag{2.59}$$

where E^* is the incident energy in the center of mass system. The value of $E_i^{\max}$ is given by

$$E_i^{\max} = \frac{M - m_i}{M}E_a, \tag{2.60}$$

where M is the total mass of the n-particles and E_a is the energy available in C.M. for one-step reactions ($E_a = E^* + Q$).

For the ^{7}Be + d reaction, there are three possible reactions that can be treated by PSM and give tritons in the exit channel:

$$^7\mathrm{Be} + d \Rightarrow \begin{cases} t + p + p +^4\mathrm{He} & \text{(a)} \\ t +^3\mathrm{He} +^3\mathrm{He} & \text{(b)} \\ t + p +^5\mathrm{Li} & \text{(c).} \end{cases}$$

These three expressions are similar to expressions (2), (5), and (6) for the three-body continuum (Sec. 2.3.1).

Chapter 3

Facility and Equipments

3.1 ^{18}F Beam Production & Transportation

The production of ^{18}F radioactive ion beams (RIBs) at the Holifield Radioactive Ion Beam Facility (HRIBF) is based on the Isotope Separation On-Line (ISOL) technique. Radioactive ions are produced by directing light ion beams accelerated by the Oak Ridge Isochronous Cyclotron (ORIC) [Alt98] onto thick, hot, refractory targets. The radioactive atoms diffusing out of the target material are then ionized, mass-analyzed, charge-exchanged (if needed), and injected into the 25-MV tandem accelerator in order to accelerated to the appropriate energy for the experiments. This RIB production is illustrated in Figure 3.1.

As the first step of ^{18}F beam production, $\sim 1\ \mu A$ of 85 MeV ^{4}He beam from the ORIC bombarded a thick HfO_2 target. ^{18}F atoms were then produced via the $^{16}O(\alpha, pn)^{18}F$ reaction. The target was of fibrous form to allow fast diffusion of ^{18}F ions out of the target. A Scanning Electron Microscope (SEM) image of a single HfO_2 fiber taken at a magnification of 5000 times is shown in Figure 3.2.

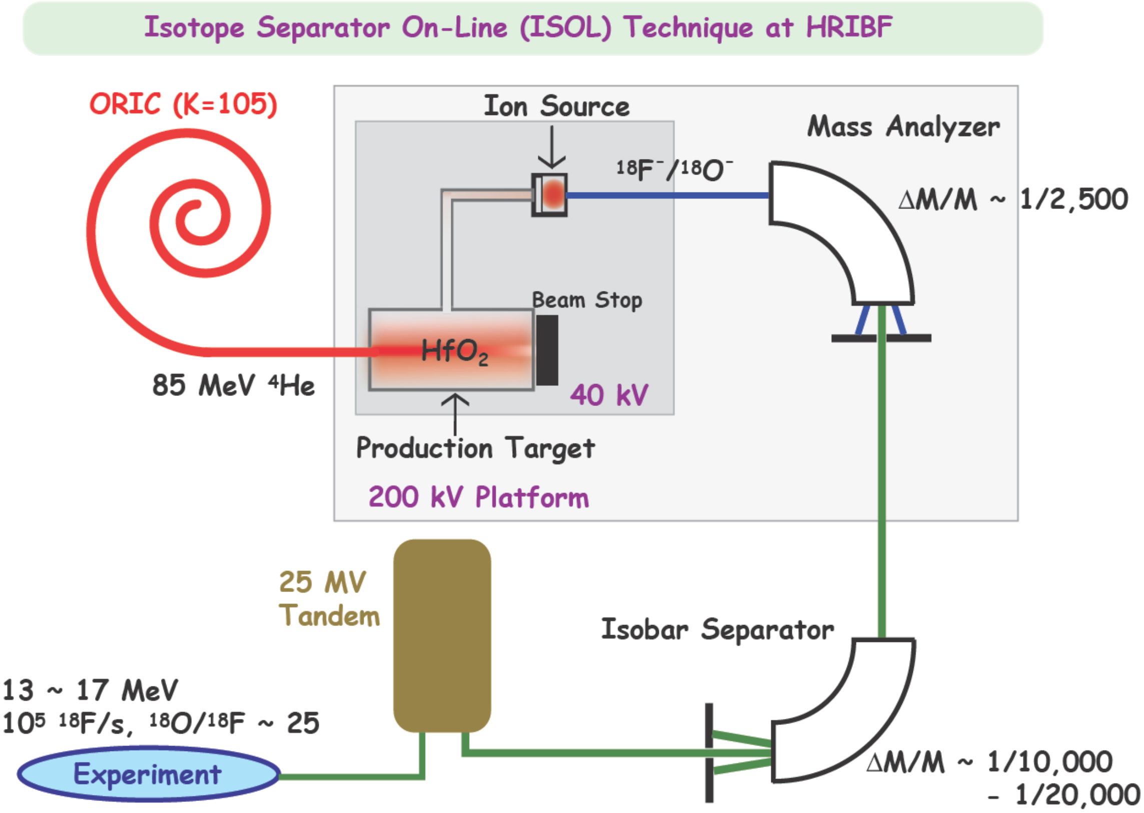

Figure 3.1: The RIB production process.

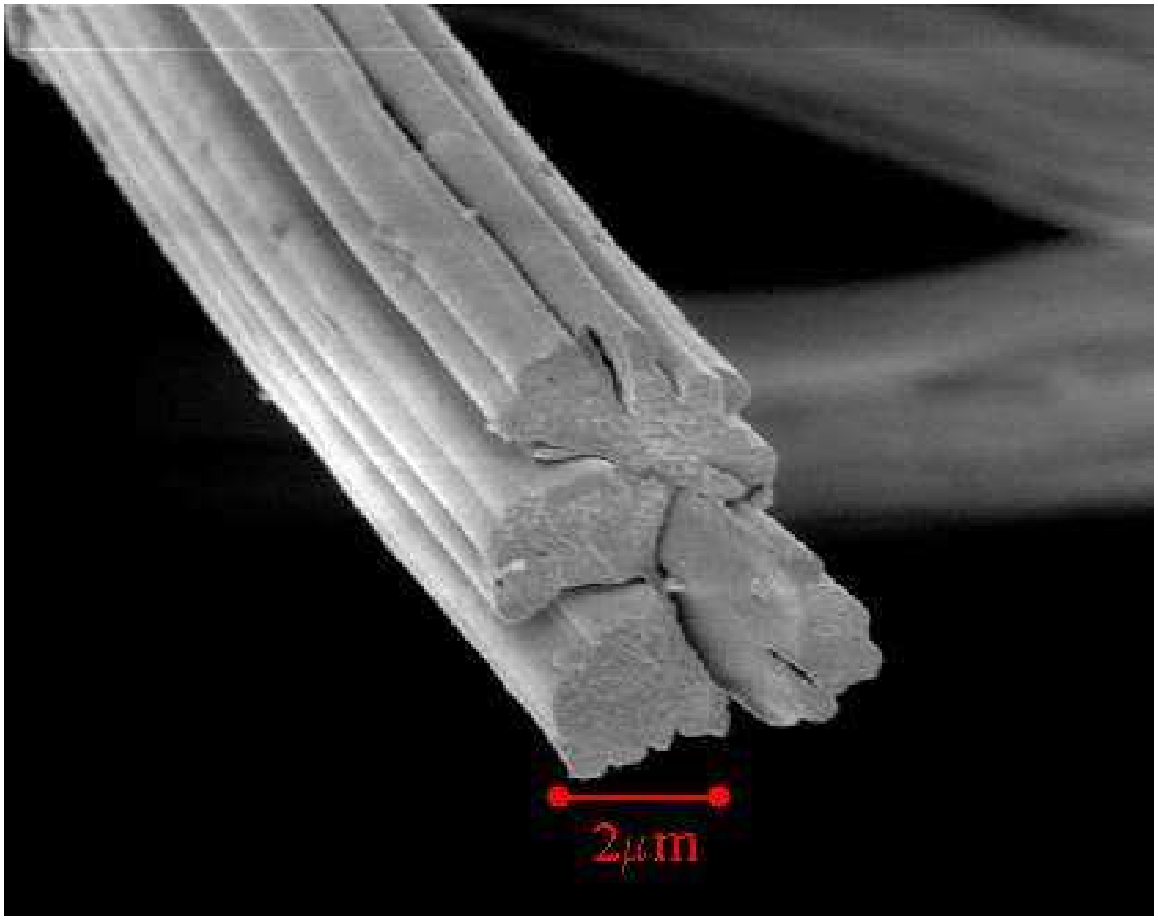

Figure 3.2: SEM photograph of a single HfO_2 fiber taken with a magnification of 5000 times.

Since the tandem accelerator requires injection of negative ions, the RIB can either be produced directly in a negative-ion source or first positively ionized and then passed through a charge-exchange cell containing a metallic vapor to form a beam of negative ions [Wel02]. The charge-exchange process for the fluorine isotopes, however, typically has a poor efficiency (e.g. $0.3 \sim 5$ %, for $\mathrm{Al}^{17}\mathrm{F}^{+}$ to $^{17}\mathrm{F}^{-}$) [Wel99]. In the production of ^{18}F beam, therefore, we have used a negative ion source. The source utilized Cs^{+} ions to ionize ^{18}F atoms by bombarding the fluorine atoms [Wel02].

After extracted from the ion source, the beam was mass-analyzed at the isobar-separation system which has a mass resolution $\Delta M/M \sim 1/2500$. The resulting $^{18}\mathrm{F}^{-}$ ions leave the high-voltage platform and go through a second-stage mass-analyzing magnet ($\Delta M/M \sim 1/10000$ to $1/20000$). The beam can be focused by a set of electrostatic quadrupole lenses onto a removable radionuclide identification system, a moving tape that brings implanted beam particles in front of a Ge detector before they decay. Following species identification, the beam was focused into a thin, vertical line which served as the object for a high-resolution magnetic isobar separation system [Alt98], and was then injected into the 25 MV tandem for acceleration to final energies needed to reproduced those in stars and stellar explosions.

The tandem electrostatic accelerator at the Oak Ridge National Laboratory (ORNL) is a folded-geometry device with excellent beam quality ($\Delta E/E = 1 \times 10^{-4}$). The high-voltage generator, located inside a 100-ft-high, 33-ft-diameter pressure vessel has been built in a folded configuration with both low- and high-energy acceleration tubes contained within the same column structure. The high terminal voltage is produced by mechanically transporting positive charge from ground. The tandem electrostatic accelerator at the ORNL is schematically drawn in Figure 3.3. The beam is accelerated through low-energy tube, and is stripped to have positive charge state at the terminal by passing through a gas- or a foil-stripper (in case of ^{18}F beam, a carbon foil

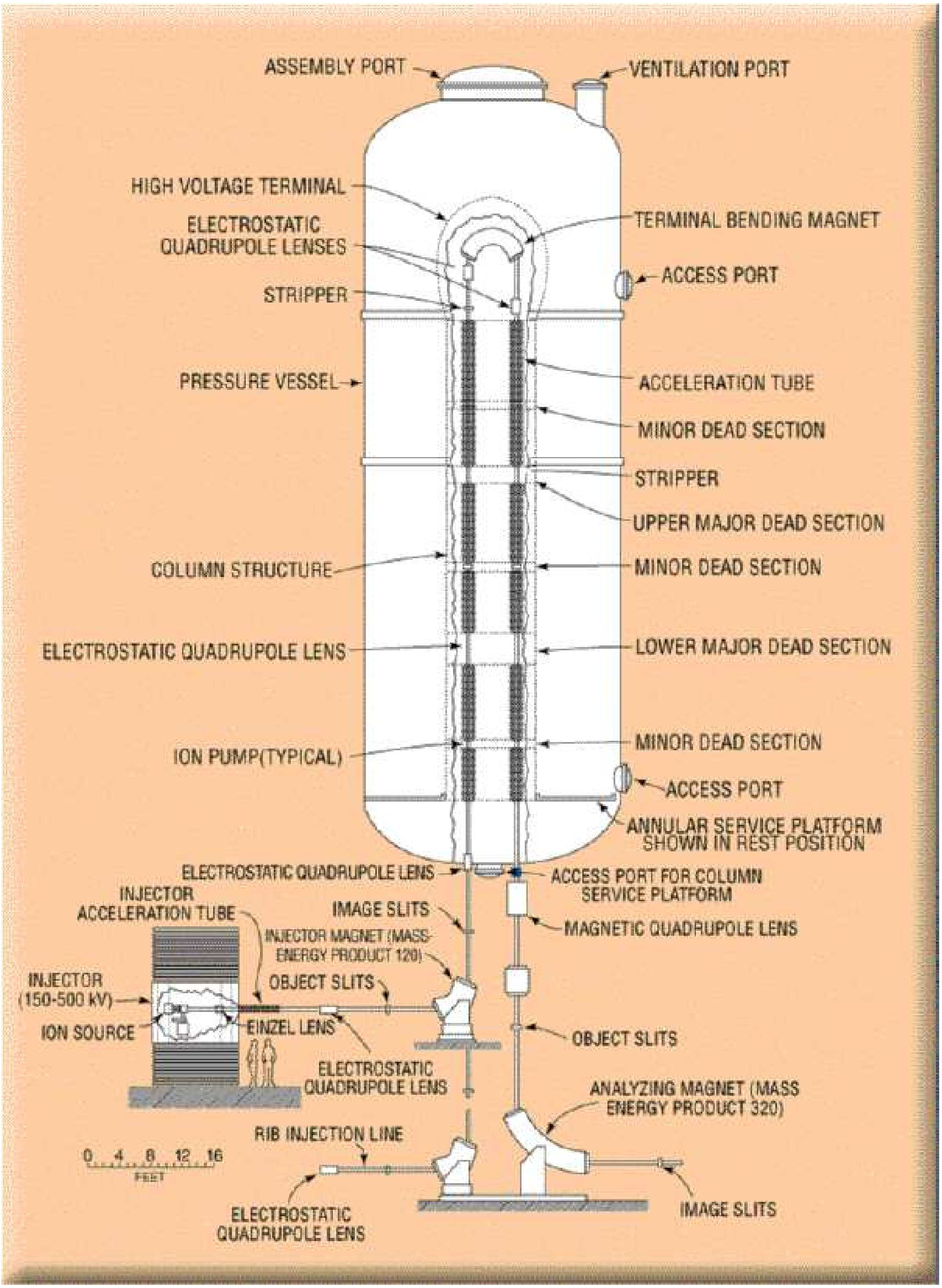

Figure 3.3: Side view of the 25 MV tandem electrostatic accelerator.

was used). Finally, the positively charged RIB is reaccelerated through high-energy tube, and goes through an energy-analyzing magnet and slits before delivery to the experimental room.

3.2 ^{7}Be Beam Production & Transportation

^{7}Be was produced at the Triangle Universities Nuclear Laboratory (TUNL) via the well-known ^{7}Li(p,n)^{7}Be reaction [Lis75]. The proton beam was accelerated up to 11.0 MeV by the FN tandem accelerator, and impinged on a 3 mm ^{7}Li target that stopped the beam. The thickness of 3 mm was chosen to maximize the ^{7}Be yield, while keeping the total ^{7}Li amount to a minimum [Fit05]. The lithium pellet was then delivered to ORNL, and ^{7}Be was chemically separated from the pellet. The chemical process was developed by Gialanella *et al.* [Gia02], and the process used at ORNL was nearly identical to their method.

After extracted, the ^{7}Be was used in a multisample cesium *sputter ion source*. The design was similar to that of sputter source described in [Alt94]. The ^{7}Be activity was mixed with copper powder and pressed into aluminum holders that are designed to fit into a multi-sample target wheel to be used with a Cs-sputter ion source. In the source, the ^{7}Be was mounted on a negatively biased probe. An oven vaporizes Cs first, which will be accelerated to the cathode by a 4.5 keV potential. The negative ^{7}Be ions are then sputtered from the cathode, and then extracted from the source by an electrode. Bombardment of the ^{7}Be with energetic cesium ions results in a large fraction of the sputtered ions being negatively charged [Rol88]. The figure of the cathodes is shown in Figure 3.4.

The schematic diagram the beam transportation system is very similar to that of ^{18}F beam (Figure 3.1), except that ORIC and the production target were not used,

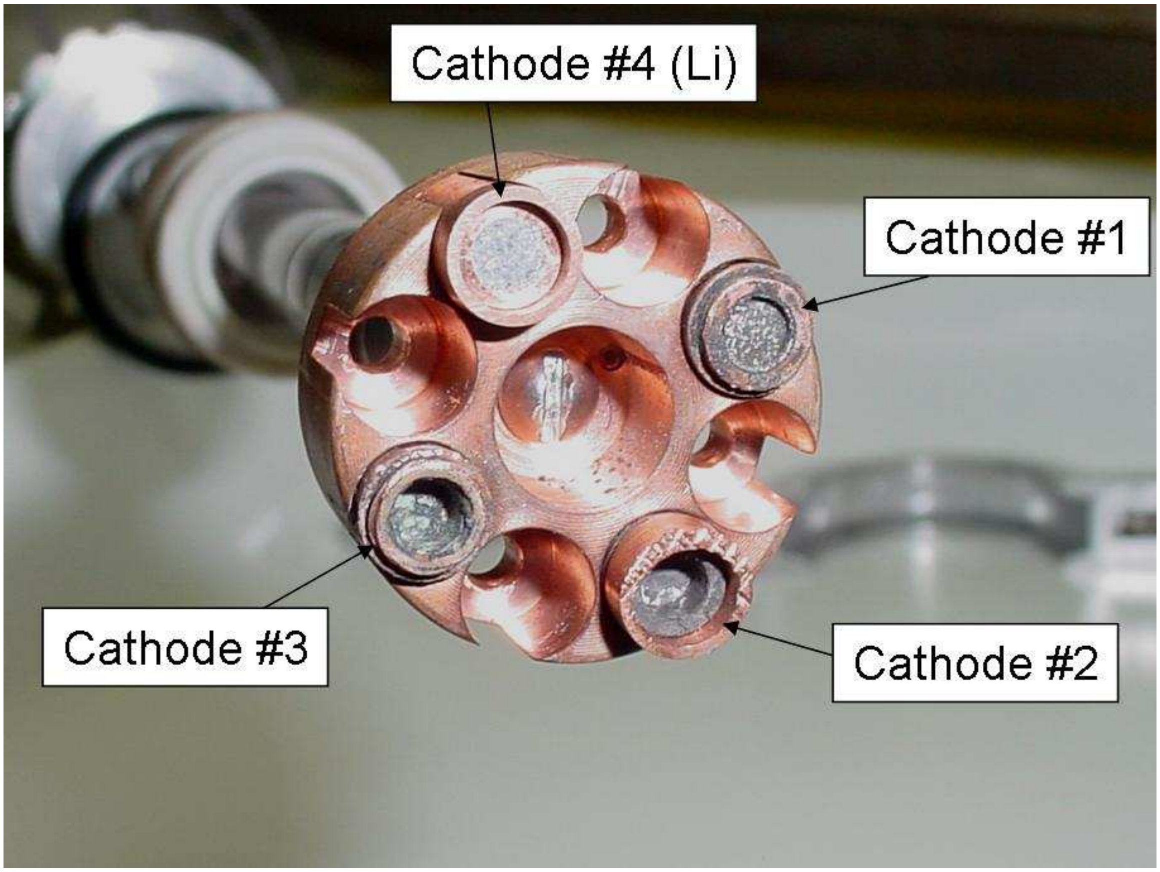

Figure 3.4: The figure of the cathodes.

and the multisample sputter ion source was used instead. The negative ^{7}Be ion is then mass analyzed, isobar separated, and injected into the 25 MV tandem accelerator.

The ^{7}Be beam is contaminated with ^{7}Li until this stage. The contamination can, however, be removed by stripping and by the analyzing magnet. By passing through carbon foil which is located at the terminal, the negative ^{7}Be ions lose their electrons and become positively charged. The majority of the ^{7}Be beam has now $q = 4^+$ state, while that of the ^{7}Li contamination has $q = 3^+$. Finally, the ^{7}Li contamination in the beam can be rejected by the energy-analyzing magnet which is located at the bottom of the high-energy end.

3.3 Detectors

3.3.1 Silicon Strip Detectors

The α particle products from the ^{18}F(p,α)^{15}O reactions and the tritons from the ^{7}Be(d, t)^{6}Be reactions need to be measured with good energy and angular resolution in an array of detectors covering a large solid angle. In the present measurements, a large area array of silicon semiconductor strip detectors was used. The silicon detector array (SIDAR) consists of 6 MSL-type YY1 wedges with 16 strips (p-type) per wedge, manufactured by Micron Semiconductor, Ltd. [Mic06] (Figure 3.5). For every sector of 16 strips, there was a single large area n-type pad on the back side. The detectors used in this experiments varied in thickness from 100 to 500 μm. The properties of a single SIDAR sector are summarized in Table 3.1 [Bar99, Mic06]. The wedges are arranged in a “lampshade” configuration in which six wedges are equally spaced and tilted forward 43° from the perpendicular to the beam axis in order to cover a larger

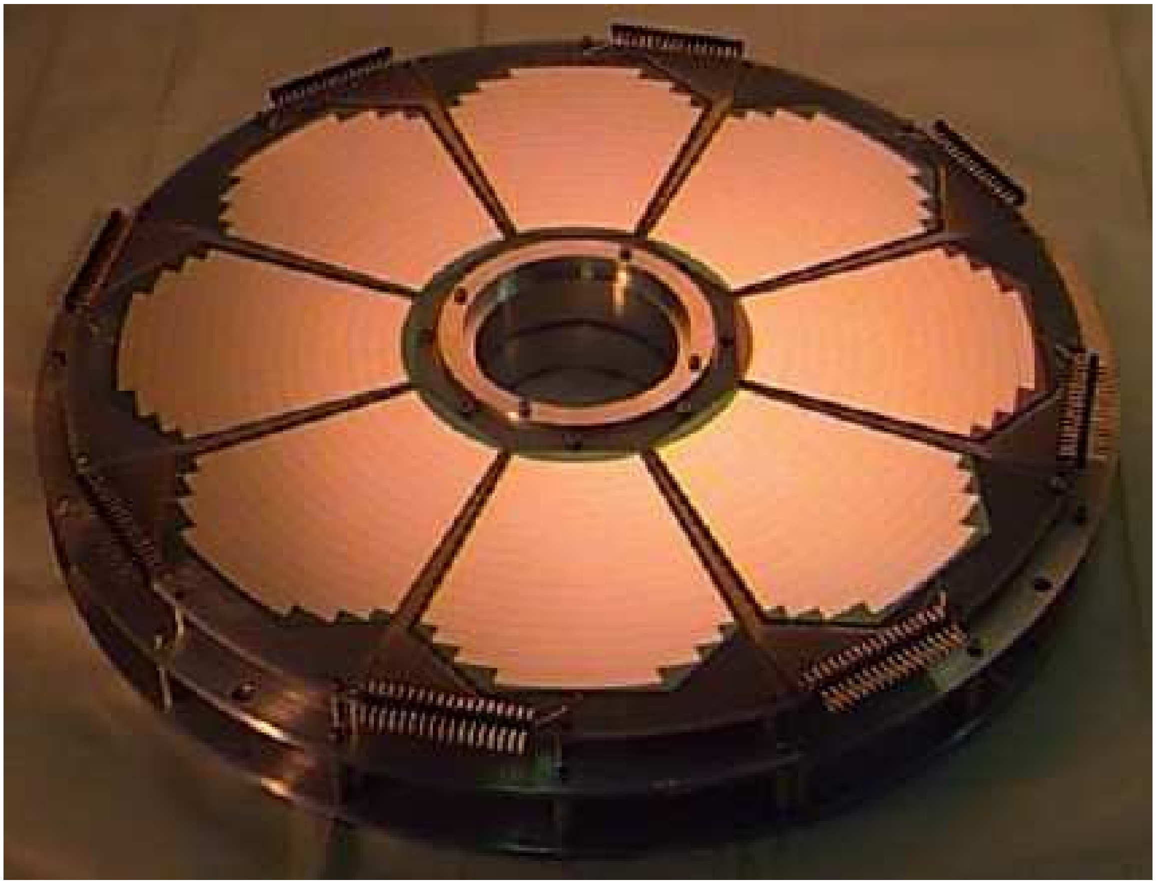

Figure 3.5: A picture of the SIDAR in flat geometry.

Table 3.1: Summary of properties for a single SIDAR sector [Bar99, Mic06].

Active inner dimensions	50 mm
Active outer dimensions	130 mm
Active area	$\simeq$ 56 cm^2
Thickness	100-500 μm
Front face	16 p-type strips
Back face	1 n-type pad
Strip width	5 mm
Inter-strip distance	100μm

angular range than a "flat" geometry (Figure 3.5). The array is centered on the beam axis and is positioned relative to the target to cover the desired angular range.

For ^{7}Be(d, t)^{6}Be measurements, three arrays of detectors were configured as shown in Figure 3.6. Each layer of detectors act as ΔE (100 μm), E (500 μm), and veto (300 μm) detectors, respectively.

Each individual detector can measure the deposited energies of the particles. In ΔE-E telescope (a thin transmission detector backed by a thick detector), however, it is possible to identify the particles by reconstructing the energy loss in a thin detector and the total energy of the particle.

The energy loss ΔE is given by the relation [Rol88]

$$\Delta E \propto \frac{MZ^2}{E}, \tag{3.1}$$

where M is the mass, Z is the charge, and E is the total kinetic energy of the particle. A measurement of ΔE and E determines, therefore, the value of MZ^2. An example of ΔE-E plot is shown in Figure 5.6 (Sec. 5.2). The plot forms hyperbolae, displaced according to the quantity MZ^2. The third layer of detectors, veto detectors, was required because of large amount of ^{3}He punching through the E detectors.

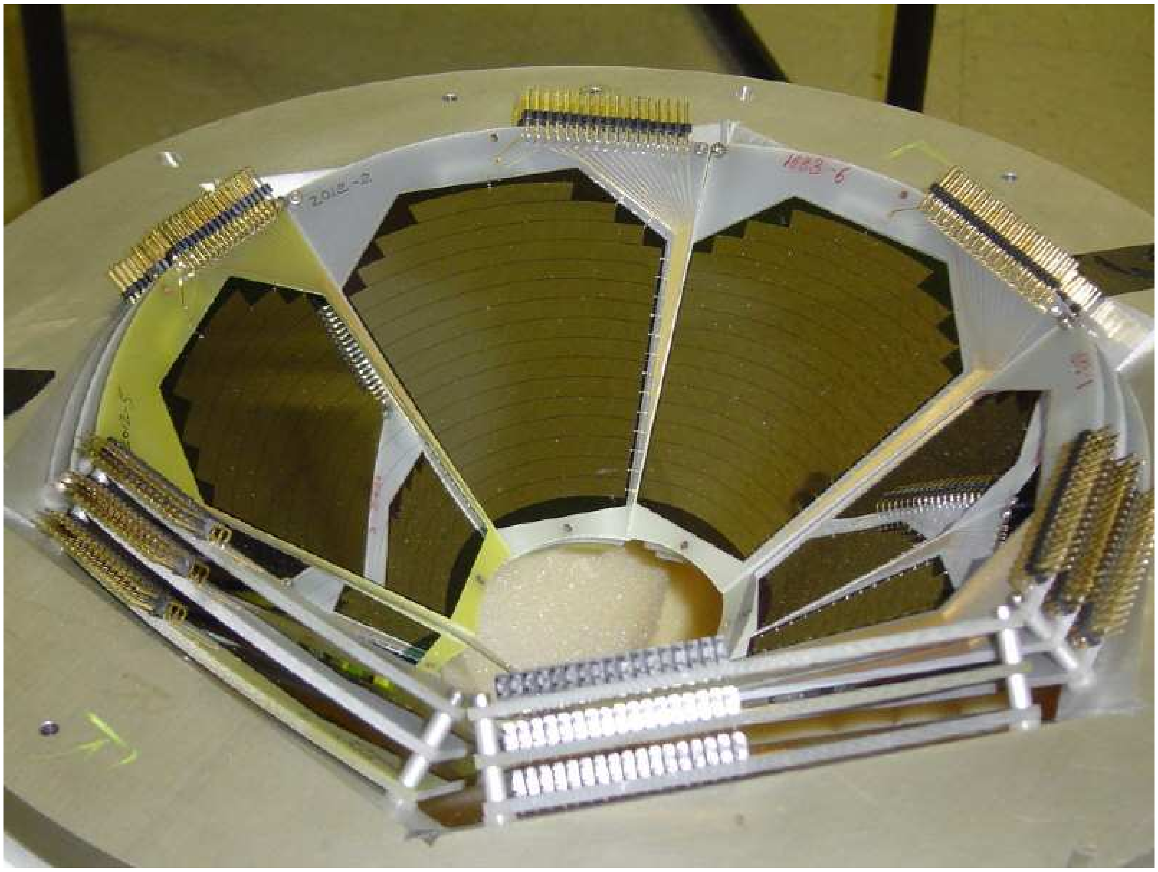

Figure 3.6: Three layers of silicon detectors in lampshade geometry.

Meanwhile, the ^{15}O products also need to be measured for the ^{18}F(p, α)^{15}O reaction. This was done by using another smaller annular detector called "MINI." The detector is constructed in quarters, each quadrant having 16 p-type strips as shown in Figure 3.7. The active inner and outer dimensions are 48 mm and 96 mm respectively.

The semiconductor junction diodes, such as SIDAR and MINI, act as charged particle detectors. When a particle deposits energy in a semiconductor detector, equal numbers of conduction electrons and holes are formed within a few picoseconds along the particle track. Once they are formed in a semiconductor, they will tend to migrate either spontaneously or under the influence of an applied electric field until they are either collected or recombination takes place [Kno00].

The region over which the charge imbalance exists is called the *depletion region* and extends into both the p and n side of the junction. Electrons and holes will diffuse into regions with lower concentrations of electrons and holes. Since n-type semiconductor has an excess of free electrons, and p-type has an excess of holes, when n-doped and p-doped pieces of semiconductor are placed together to form a junction, electrons will diffuse into the p side and holes will diffuse into the n side. When a hole and an electron come into contact, however, they eliminate each other through recombination. This bares the donor atoms, which are now charged ions, adjacent to the depletion region. The ions are positive on the n side and negative on the p side, creating an electric field that counteracts the continued diffusion of charge carriers. When the electric field is sufficient to repel incoming holes and electrons, the depletion region reaches its equilibrium width. Normally, the reverse bias(p negative with respect to n) is applied so that the depletion region extends throughout the whole volume of the silicon [Kno00]. Under this condition, the electron-hole pairs induced by ionizing radiation that passes through the depleted volume are collected on the electrodes bounding the active volume of the silicon detector.

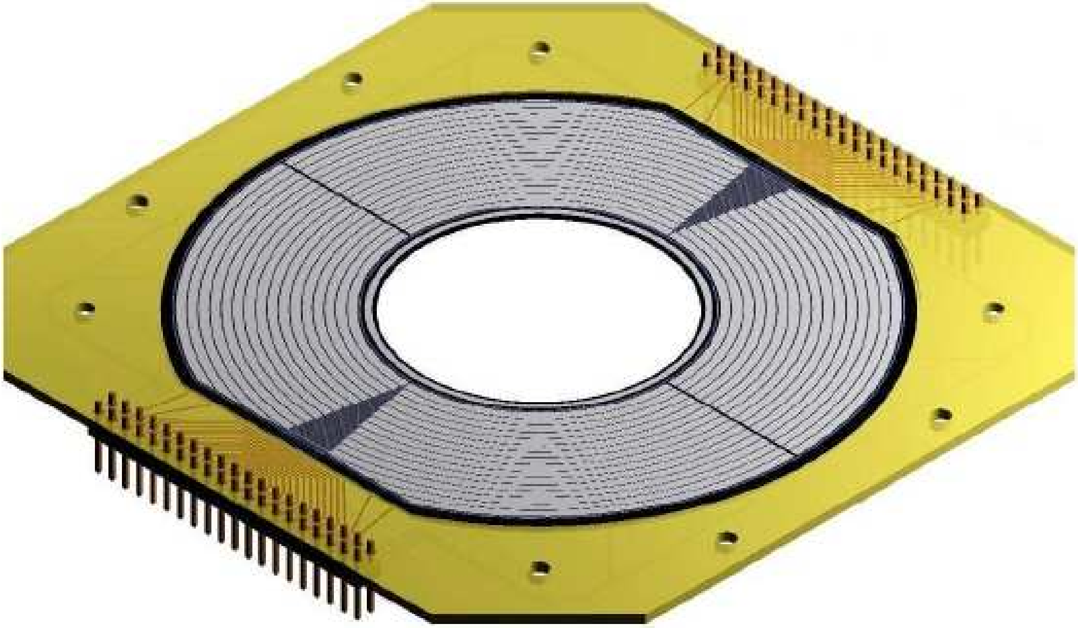

Figure 3.7: MINI is shown in the figure. Figure from Micron Semiconductor Limited [Mic06].

The main benefit of silicon detectors is that the resolution of silicon detectors is typically an order of magnitude greater than that of the gas-filled ionization counters (Sec. 3.3.2). The reason for this is that the energy required to produce an electron-hole pair in silicon detector (3.62 eV at 300 K) is roughly ten times less than the energy required to create an electron-ion pair ($\sim$ 30 eV) at the gas-filled ionization counter [Kno00]. Obviously, the same amount of ionizing radiation will create ten electron-hole pairs in silicon for every one electron-ion pair produced in a gas. With a larger current produced, the resolution of a silicon detector will correspondingly be improved. In addition to their resolution, another benefit of the silicon detector is their size. The detectors are very small and compact.

The solid angle covered by each silicon strip was obtained using a calibrated ^{244}Cm source which emits 5.805 MeV (branching ratio of 76%) and 5.763 MeV (branching ratio of 24%) alpha particles. The energy calibration spectrum from one of the SIDAR strip is shown in Figure 3.8. This measured solid angle agreed with geometric calculations within 3%.

3.3.2 The Gas-filled Ionization Counter

The ^{18}F radioactive beams delivered to the target was highly contaminated by ^{18}O. As we shall see in Sec. 4.2, the ^{18}O(p,α)^{15}N events fell in the ^{18}F(p,α)^{15}O gate, making it necessary to measure ^{18}O(p,α)^{15}N with pure ^{18}O beams. The beam amount deposited on the target was required in both cases, and this was done by monitoring the scattered ^{18}F and ^{18}O ions using the gas-filled ionization counter (IC).

Heavy charged particles interact with matter primarily through Coulomb forces between their positive charge and the negative charge of the orbital electrons within the absorber atoms. In some cases, the interaction is strong enough to *excite* or *ionize*

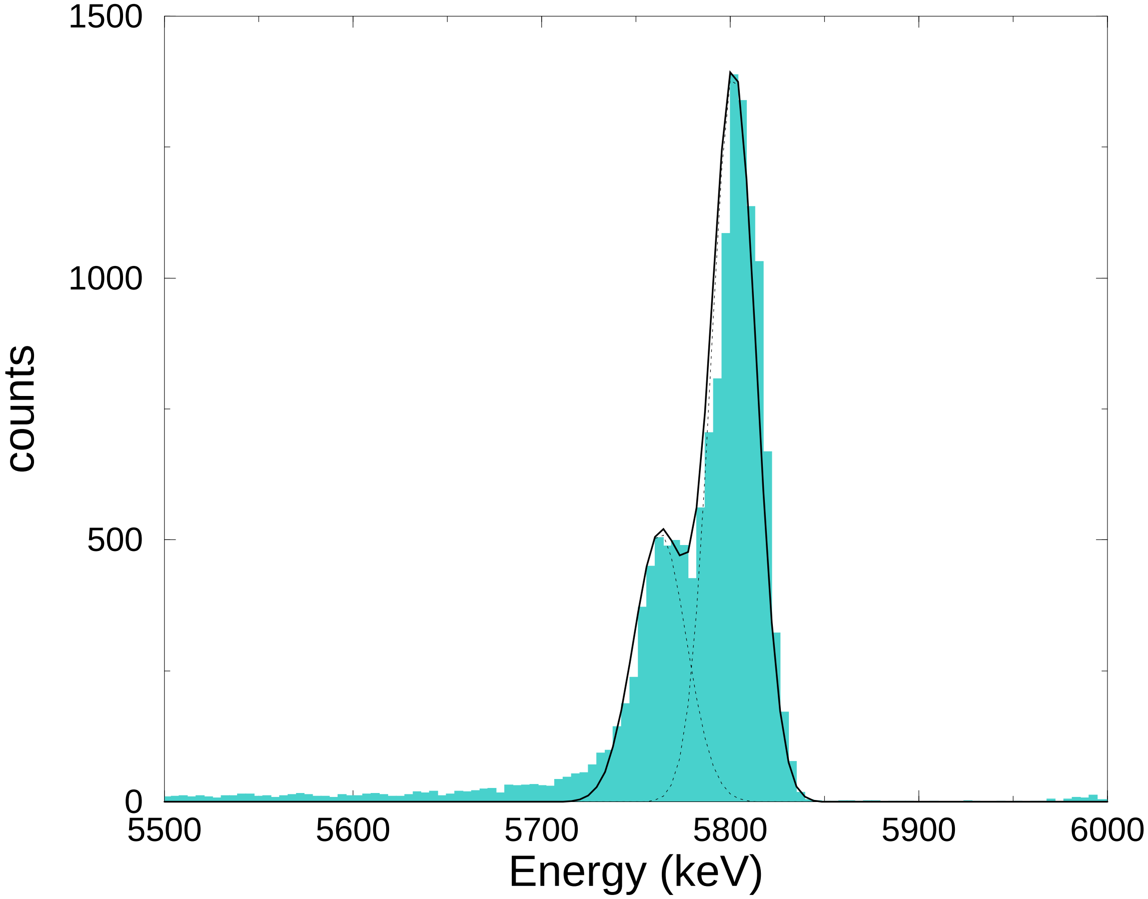

Figure 3.8: The energy calibration spectrum from one of the SIDAR strips.

atoms in the absorbing medium. Energy required to ionize (or excite) atoms must come from the incoming charged particle, and its velocity is therefore decreased as a result of this. The energy loss (also known as *stopping power*) is described by the *Bethe formula* as [Kno00]

$$-\frac{dE}{dx} = \frac{4\pi e^4 z^2}{m_0 v^2} NZ \left[\ln \frac{2m_0 v^2}{I} - \ln\left(1 - \frac{v^2}{c^2}\right) - \frac{v^2}{c^2}\right], \qquad (3.2)$$

where v are ze are the velocity and charge of the primary particle, N and Z are the number density and atomic number of the absorber atoms, m_0 is the electron rest mass, I is the average excitation and ionization potential of the absorber, and e is the electronic charge [Kno00]. For nonrelativistic charged particles ($v \ll c$), the stopping power varies as z^2/v^2 since the other factors in the above expression vary slowly with particle energy, or species of the incident particle. The IC shows therefore the sensitivity to different atomic species.

When the charged particle comes into the IC through thin window, the energy is transferred from the incoming particle to the gas and thus *electron-ion pairs* are created along the track of the particle. Collisions between positive ions and free electrons may result in *recombination* in which the electron is captured by the positive ion and returns it to a neutral atom. An external electric field is applied to the region in which ions or electrons exist in the gas in order to prevent recombination, and attract electrons and ions to electrodes (*anode* and *cathode*, respectively).

The IC that was used for the experiments is a 30 cm long particle detector with 3 anodes (lengths of 5 cm, 5cm, and 20 cm) and one cathode. The first two anodes of 5 cm lengths act as ΔE detector, while the third one is used as E detector. The anodes are parallel to the beam direction and located on the beam-right side of the counter. The volume of the IC is divided into two parts by a *Frisch grid*, which can remove the dependence of the pulse amplitude on position of interaction [Kno00]. The grid is located $\sim$ 1 cm in front of the anodes maintaining an intermediate potential between the anodes and the cathode. Once the electrons pass through the grid, the voltage between the anodes and the grid starts to drop and a signal voltage begins to develop. Since the grid prevents any voltage change in anodes when the electron is out of grid-anodes region, the rise time of anode signal only depends on the drift velocity of the electron. The pulse amplitude is now simply proportional to the total number of ion pairs produced. More details about the IC are given in Ref. [Jam88].

The diagram of the IC is shown in Figure 3.9. The IC was filled with perfluoromethane (CF_4) gas which shows a fast response and recovery time. The IC was attached at the end of beam line in order to monitor the ^{18}F and ^{18}O ions which were scattered from the carbon component of the target. The CF_4 gas pressure ($\sim$ 5 torr) was chosen so that the incident particles could stop somewhere between the end of the first anode and the back of IC. In this way, the energy loss ΔE and the remaining energy E can be measured at anode 1+2 and anode 3, respectively.

Since the stopping power for nonrelativistic charged particles is proportional to z^2/E as shown above, the IC is sensitive to incoming atomic species. When particles of two different species with the same energy enter into the IC, for instance, the particle with higher energy atomic number loses more energy in the first anode than the other particle. By plotting ΔE versus E (or ΔE+E), therefore, different species are easily identified (see Figure 4.3).

The average energy required to create one electron-ion pair (the W-value) in IC is in principle a function of the species of gas involved. A typical value is 25-35 eV/ion pair [Kno00]. The expected counting rate at the IC is $\sim$ 3000 particles per second, which is enormously large number compared to charged particle detectors counting

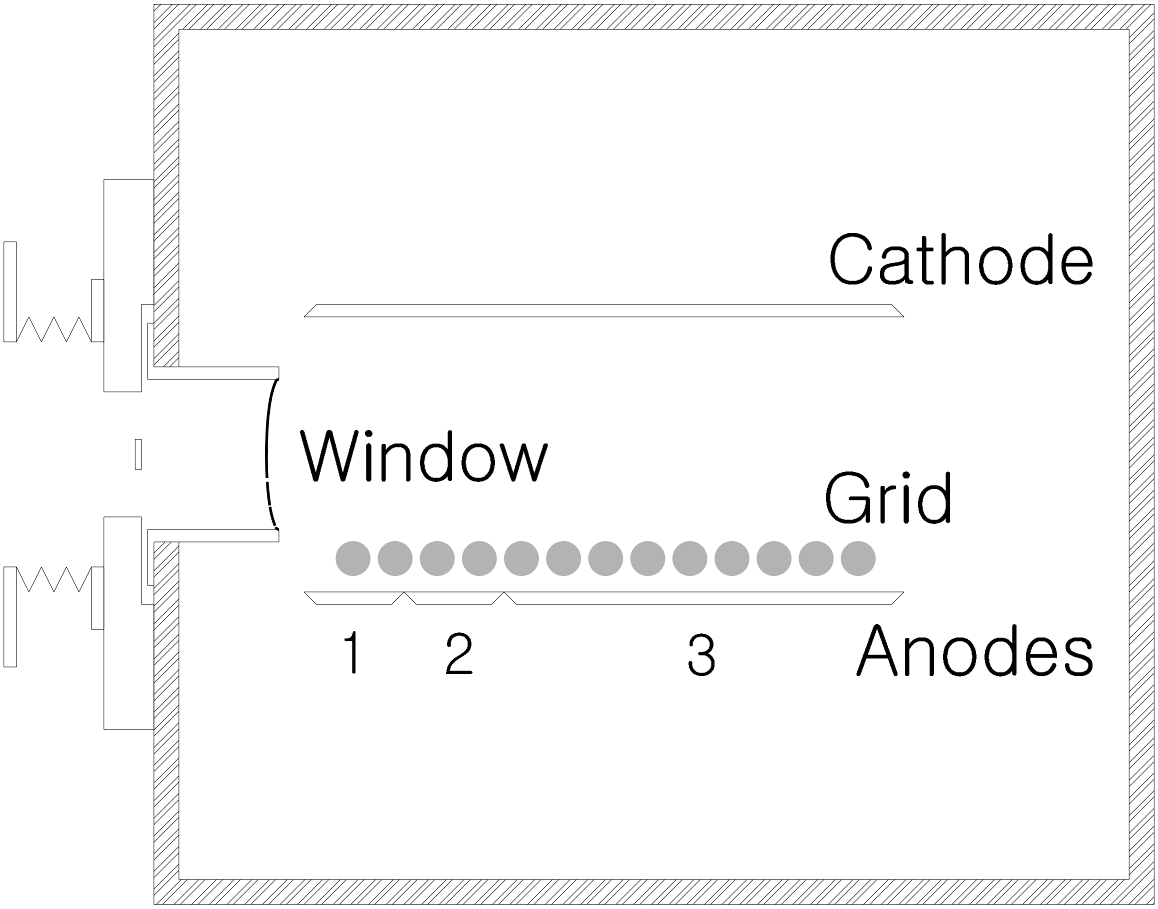

Figure 3.9: Diagram of the gas-filled ionization counter.

rate ($\sim$ 100 particles per second). The IC, therefore, had to handle a high counting rate with minimal losses to the pile-up of pulses.

Chapter 4

^{1}H(^{18}F,α)^{15}O Measurements

4.1 Motivation

The γ-ray emission from novae during the first several hours of the expansion is dominated by positron annihilation resulting from the beta decay of radioactive ^{18}F nuclei in the expanding envelope [Her99, Coc00]. The decay of ^{18}F is the most important positron annihilation source during this time because of its relatively long half-life (110 min) and large production rate. ^{18}F is synthesized in novae via proton capture on ^{17}O, or through the sequence ^{17}F(p,γ)^{18}Ne(e$^{+}\nu_e$)^{18}F, and is destroyed predominantly by the ^{18}F(p,α)^{15}O reaction [Utk98]. Knowledge of the ^{18}F(p,α)^{15}O reaction is, therefore, very important for the estimation of the amount of ^{18}F that survives the explosion and, therefore, the sensitivity of γ-ray telescopes to detect the ^{18}F decay radiation.

Because of the importance of understanding the ^{18}F + p reactions, a number of studies of the A=19 isobars have been made using stable and exotic beams [Cos95, Reh96, Utk98, Bar00, Gra00, Bar01, Bar02, Bar04, deS05, Koz05]. These studies have substantially improved our understanding of the ^{18}F(p,α)^{15}O reaction. There are still, however, remaining questions to be answered. As an example, the interference among $J^\pi = 3/2^+$ resonances could not be taken into account in reaction rate calculations due to the lack of experimental knowledge about the relative signs of the effect. As described in Refs. [Koz05,deS05], however, the interference has a significant effect on the reaction rate at nova temperatures. A recent calculation of the interference between the $E_{c.m.}$ = 38- and 665-keV resonances reported by de Séréville *et al.* [deS05] found that the best fit to the data of Bardayan *et al.* [Bar02] was obtained for constructive interference between the two resonances. That study was limited, however, in that the interference between all three low-lying $3/2^+$ resonances was not considered, and the calculations were constrained only by a single data point (Figure 4.1).

The goal of the present work was to study these interference effects by measuring the ^{18}F(p,α)^{15}O cross section off resonance. The cross sections on resonance are determined mostly by the properties of those resonances, while the cross sections off resonance are very sensitive to the interference. R-matrix calculations indicate that the cross section of the ^{18}F(p,α)^{15}O reaction at energies above the 665-keV resonance show a significant sensitivity to the interference of lower-lying 8-, 38-, and 665-keV resonances. The measurement of the ^{18}F(p,α)^{15}O reaction at energies above the 665-keV resonance (where the cross sections are larger) can thus be used to constrain the relative interference of the lower-lying levels at low energies.

4.2 Measurements & Data Analysis

The ^{18}F beam was produced at the ORNL HRIBF [Str03] using the Isotope Separator On-Line (ISOL) method. A beam of ^{4}He from the ORIC bombarded a thick HfO_2 target to produce ^{18}F atoms via ^{16}O(α,pn)^{18}F reaction [Wel02]. The produced ^{18}F

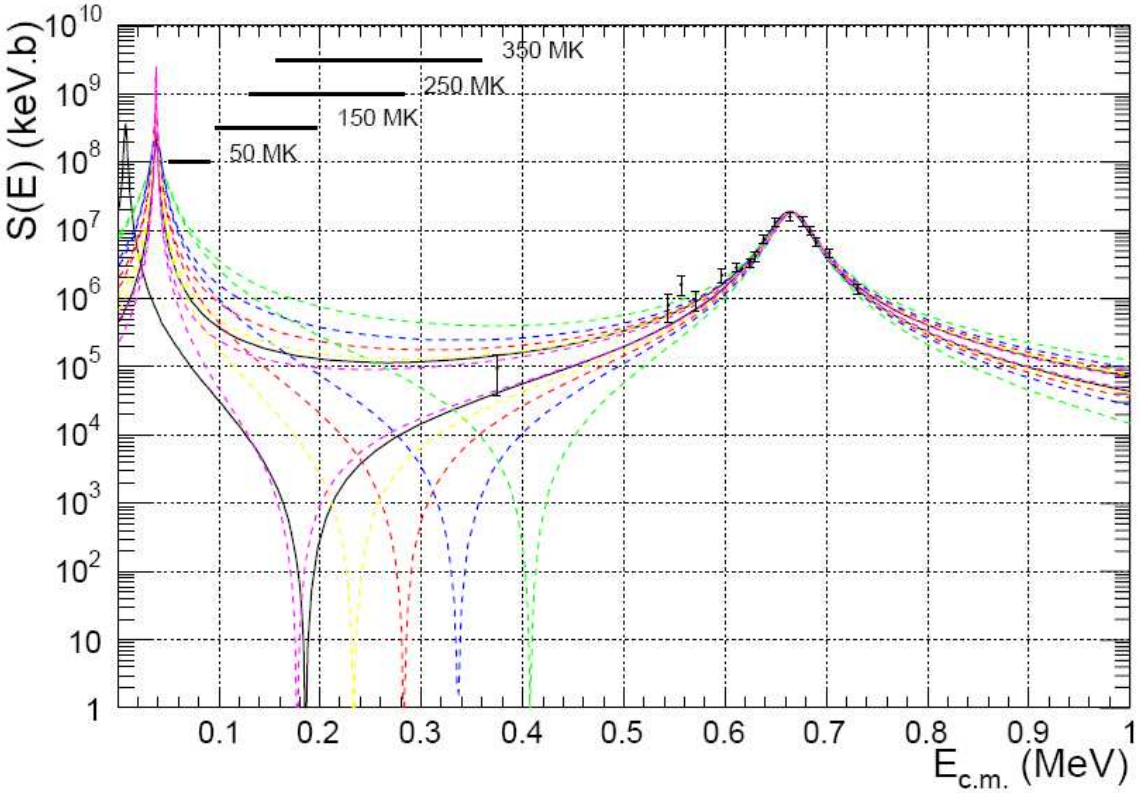

Figure 4.1: Astrophysical S-factor for constructive and destructive interferences between 38- and 665-keV resonances. Figure taken from [deS05].

atoms were then mass analyzed and post accelerated by the tandem electrostatic accelerator to the appropriate energies for this experiment.

The ^{1}H(^{18}F,α)^{15}O excitation function was measured at 5 energies over the range $E_{c.m.} \simeq$ 663 - 877 keV: 663, 717 770, 824, and 877 keV. A schematic diagram of the experimental setup is shown in Figure 4.2. The ^{18}F beam ($\sim 10^{5}$ ^{18}F/s, ^{18}F/^{18}O $\sim$ 0.04) was used to bombard a 70 μg/cm^{2} polypropylene CH$_{2}$ target (5.5$\times$10^{18} ^{1}H atoms/cm^{2}). 1 MeV steps were taken in bombarding energy ($\Delta E_{c.m.} \simeq$ 50 keV), because the ^{18}F beam loses about 970 keV in the target at this energy.

Recoil α-particles and ^{15}O ions from the ^{1}H(^{18}F,α)^{15}O reaction were detected in coincidence by two large area silicon detector arrays (SIDAR and MINI, respectively) as shown in Figure 4.2. The SIDAR [Bar01] was tilted forward 43° from the perpendicular to the beam axis in order to cover a large angular range ($29^\circ \leq \theta_{lab} \leq 73^\circ$), while the smaller annular detector (MINI) covers $11.5^\circ \leq \theta_{lab} \leq 22.5^\circ$. Scattered ^{18}F and ^{18}O ions were also continuously detected by a gas-filled ionization counter, enabling a constant monitoring of the beam composition. Figure 4.3 shows an example of the spectrum from the IC, where the y axis is the energy deposited at the first two anodes and the x axis is the total energy. By counting the numbers of events in the gates as shown in the figure, the ^{18}F/^{18}O ratio could be measured. The amount of ^{18}F deposited on target was determined from the amount of beam scattered from the carbon in the target and detected in the MINI detector using the measured ratio of ^{18}F/^{18}O in the beam and scaling, where appropriate, by the relative atomic numbers. In the Rutherford scattering theory, the differential cross section is

$$\frac{d\sigma}{d\Omega} = \frac{4Z^2e^2}{16E}\frac{1}{\sin^4\frac{\theta}{2}}, \tag{4.1}$$

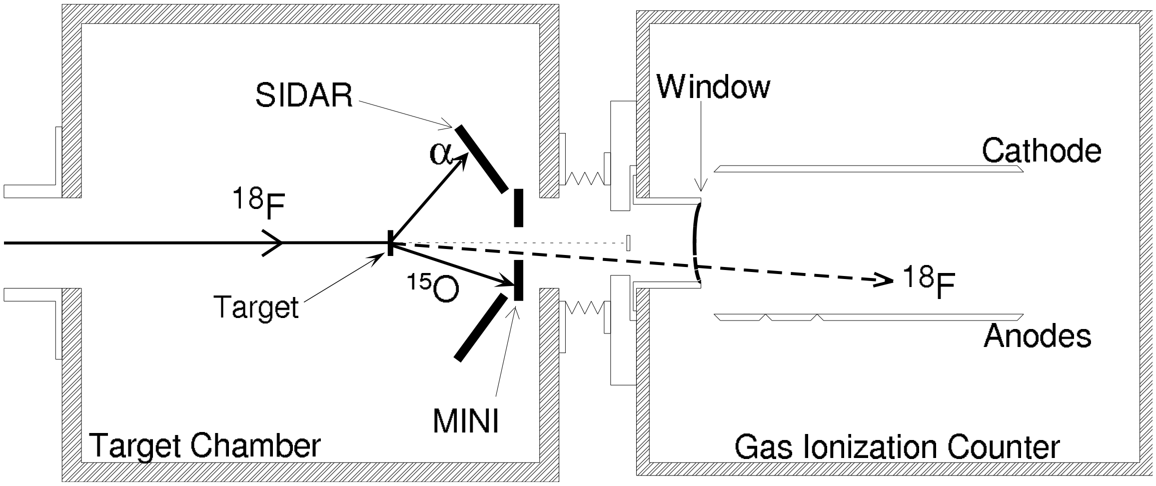

Figure 4.2: A schematic diagram of the experimental setup. A ^{18}F beam was used to bombard a 70 μg/cm^2 CH$_2$ target. The α particles and ^{15}O ions were detected in two silicon detector arrays, while scattered ^{18}F were detected in a gas-filled ionization counter.

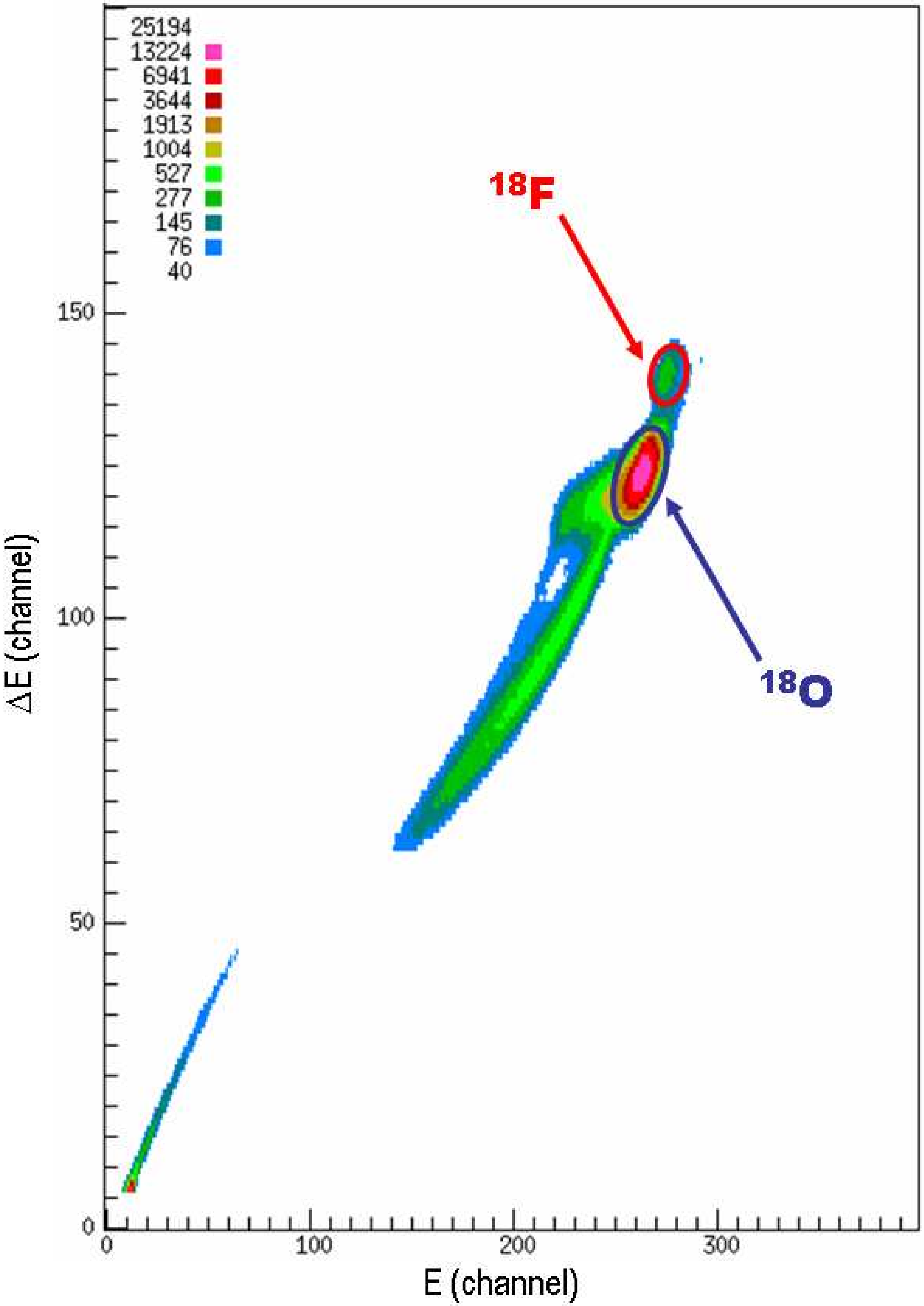

Figure 4.3: A spectrum from the IC.

where Z is the number of protons, E is the energy of the scattered particle. For ^{18}F/^{18}O cocktail beam, therefore, the cross section ratio between the two species depends only on the numbers of protons when the energies and the detected angles for a ^{18}F and ^{18}O are the same. The unscattered beam was stopped by a 1.5 cm disk which was put in front of the ion counter window to protect it from receiving the full beam intensity.

The ^{1}H(^{18}F,α)^{15}O and ^{1}H(^{18}O,α)^{15}N events were identified by reconstructing the total energy of detected particles in SIDAR and MINI (See Figure 4.4). Inside of the gate shown in this figure, the intense events were from the ^{1}H(^{18}O,α)^{15}N reaction and the fainter line of events was from the ^{1}H(^{18}F,α)^{15}O reaction. The intense groups along the x- and y-axis were from elastic scattering. Owing to the different Q values for the reactions, the α particles from the ^{1}H(^{18}F,α)^{15}O reaction could be distinguished from the ^{1}H(^{18}O,α)^{15}N events.

To determine the number of ^{1}H(^{18}F,α)^{15}O events that were observed at a given energy, several selections ("cuts") to the entire data set were applied. The time between SIDAR and MINI events was measured via a time-to-amplitude converter (TAC, see Figure 4.5), and the first cut was the requirement of an appropriate time coincidence. The next cut was in total energy - shown by the gate in Figure 4.4. Finally, the coplanarity of the α particle and ^{15}O ion were checked (i.e., the α particle and ^{15}O ions should be separated by $180° \pm 60°$, where 60° was the range covered by one SIDAR detector). With these conditions applied, the α angle was plotted versus its energy (Figure 4.6) and the number of ^{18}F(p,α)^{15}O events summed.

Even with all these conditions applied, there were still ^{18}O(p,α)^{15}N events which fell in the ^{18}F(p,α)^{15}O gate owing to the low purity of the beam. To estimate the number of contaminant events, we ran with a pure ^{18}O beam at each energy under identical conditions. This was done quickly by ending the cyclotron bombardment

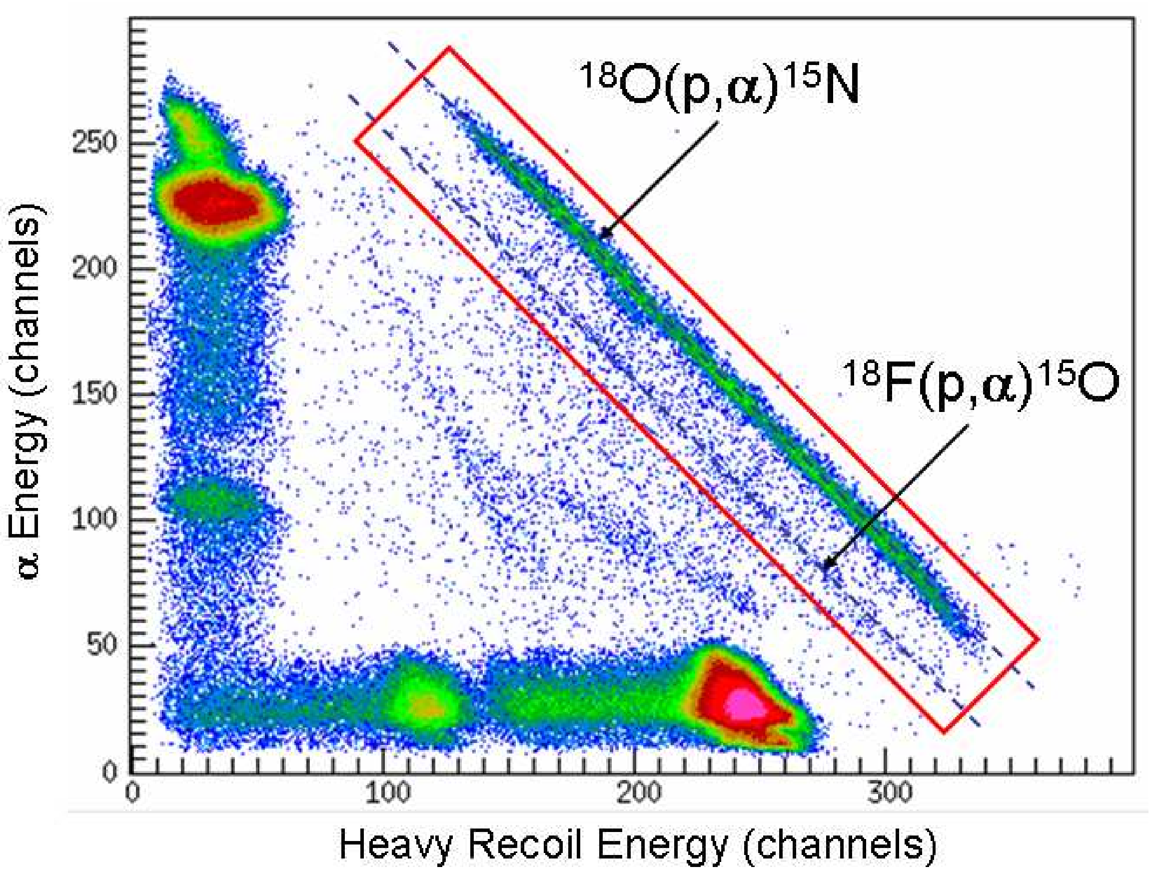

Figure 4.4: α energy vs heavy recoil energy plot. Events from $^{1}H(^{18}F,\alpha)^{15}O$ and $^{1}H(^{18}O,\alpha)^{15}N$ are shown in the gate. In this gate, the intense line is from $^{1}H(^{18}O,\alpha)^{15}N$ and the fainter line from $^{1}H(^{18}F,\alpha)^{15}O$. Strong elastic scattering groups lie along the x and y axes. $^{1}H(^{18}F,\alpha)^{15}O$ events could be identified by their different Q values. Two dashed lines show the regions where the events from two reactions are expected from kinematics.

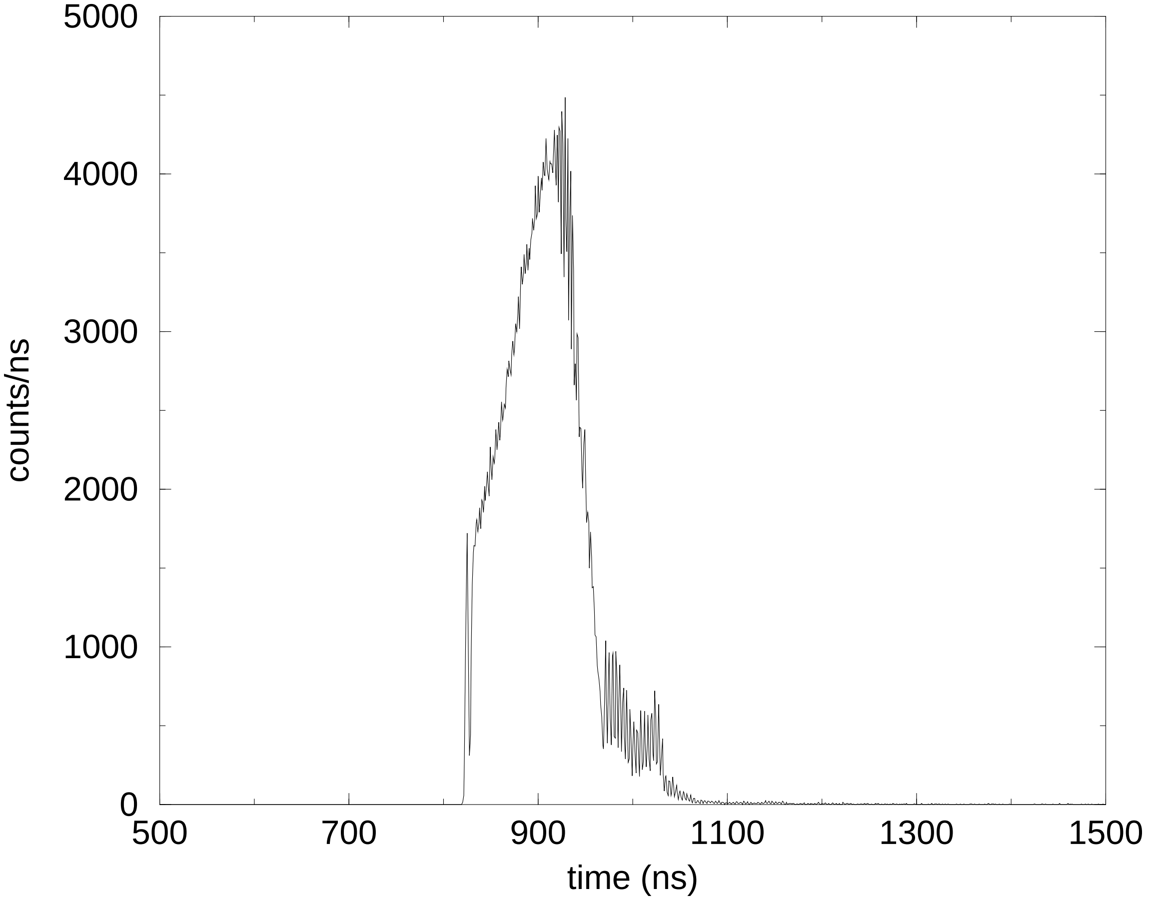

Figure 4.5: Time difference between SIDAR and MINI events.

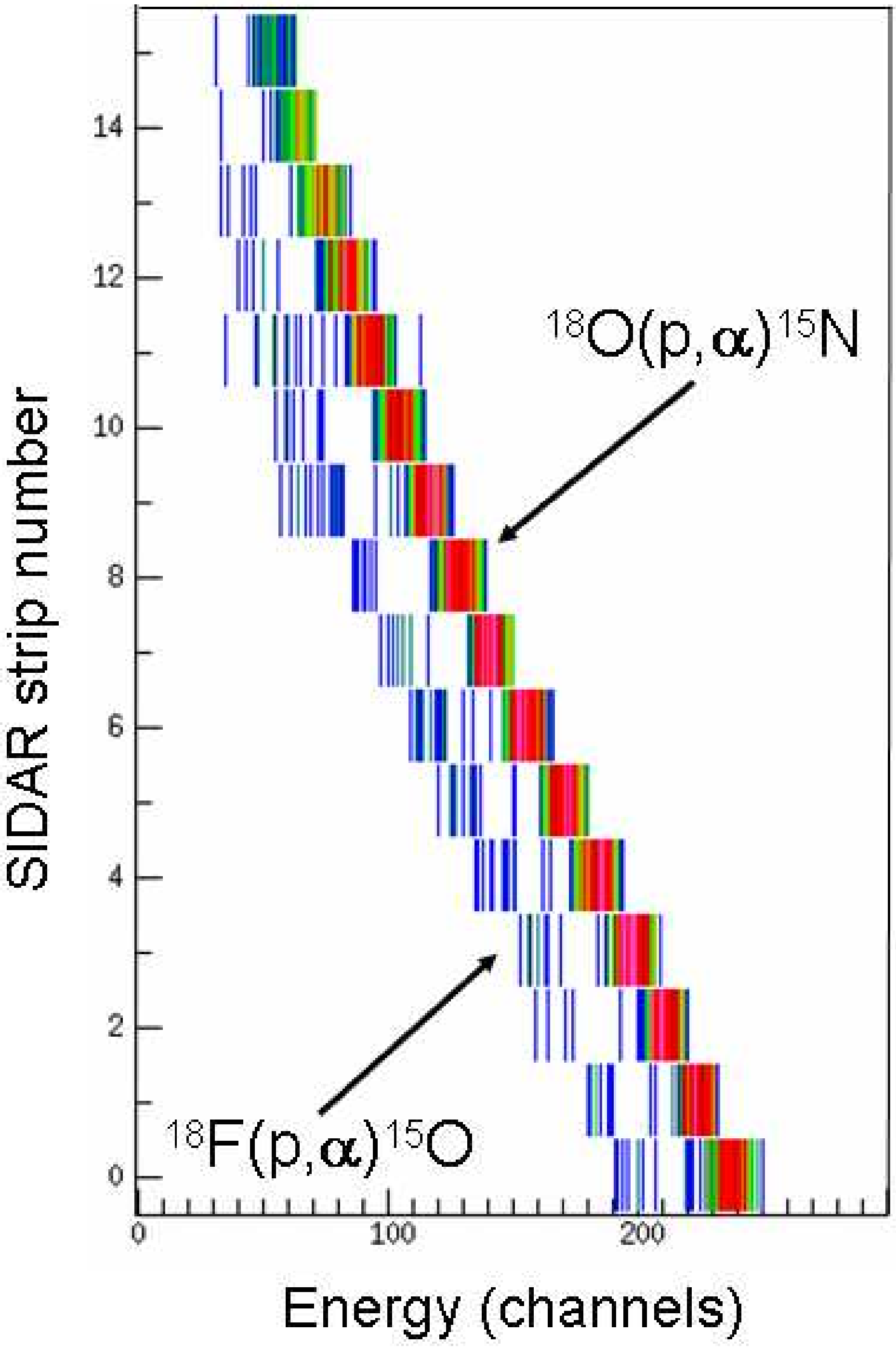

Figure 4.6: SIDAR strip number vs energy plot for events with the correct total energy. The ^{18}F(p,α)^{15}O and ^{18}O(p,α)^{15}N events are clearly visible. Here SIDAR strips 1-16 cover laboratory angles 29°- 73°, respectively.

at the ISOL target with the ^{18}F component decaying quickly with a half-life on the order of the hold up time in the target (~minutes) [Wel02]. We then subtracted the estimated amount of contaminant events from those in the ^{18}F(p,α)^{15}O gate to obtain the number of events of interest. These pure ^{18}O beam runs were also useful for checking the beam current normalization, since the ^{18}O(p,α)^{15}N cross section is well known [Chr90].

The differential cross section in the center of mass system at each energy was calculated as

$$\left(\frac{d\sigma}{d\Omega}\right)_E = \frac{Y(E)}{IN\sum_s \Delta\Omega_s \epsilon_s}, \tag{4.2}$$

where $Y(E)$ was the number of α particles identified from ^{1}H(^{18}F,α)^{15}O reaction, I was the number of ^{18}F ions incident on the target, N was the number of hydrogen atoms per unit area, $\Delta\Omega_s$ was the solid angle covered by a SIDAR strip in the center of mass system, and ϵ_s was the coincidence efficiency for detecting an α particle in that strip and the corresponding ^{15}O ion in the MINI detector. The beam current was determined from the number of scattered ^{18}F and ^{18}O ions detected in the MINI at $\theta_{lab} = 12°$, assuming Rutherford scattering, and the solid angle covered by each strip was obtained using a calibrated ^{244}Cm source that emits 5.8 MeV α particles. This measured solid angle agreed with geometric calculations within 3%. The coincidence efficiency of each strip was calculated from the known detector geometry and kinematics. The ^{18}F(p,α)^{15}O cross sections from our study are plotted in Figure 4.7. As a result of the ^{1}H(^{18}O,α)^{15}N cross section peaking at $E_{c.m.} = 789$ keV (see Figure 4.8) and the large ^{18}O contamination of the beam, only upper limits on the cross section were obtained at $E_{c.m.} = 770$ and 824 keV.

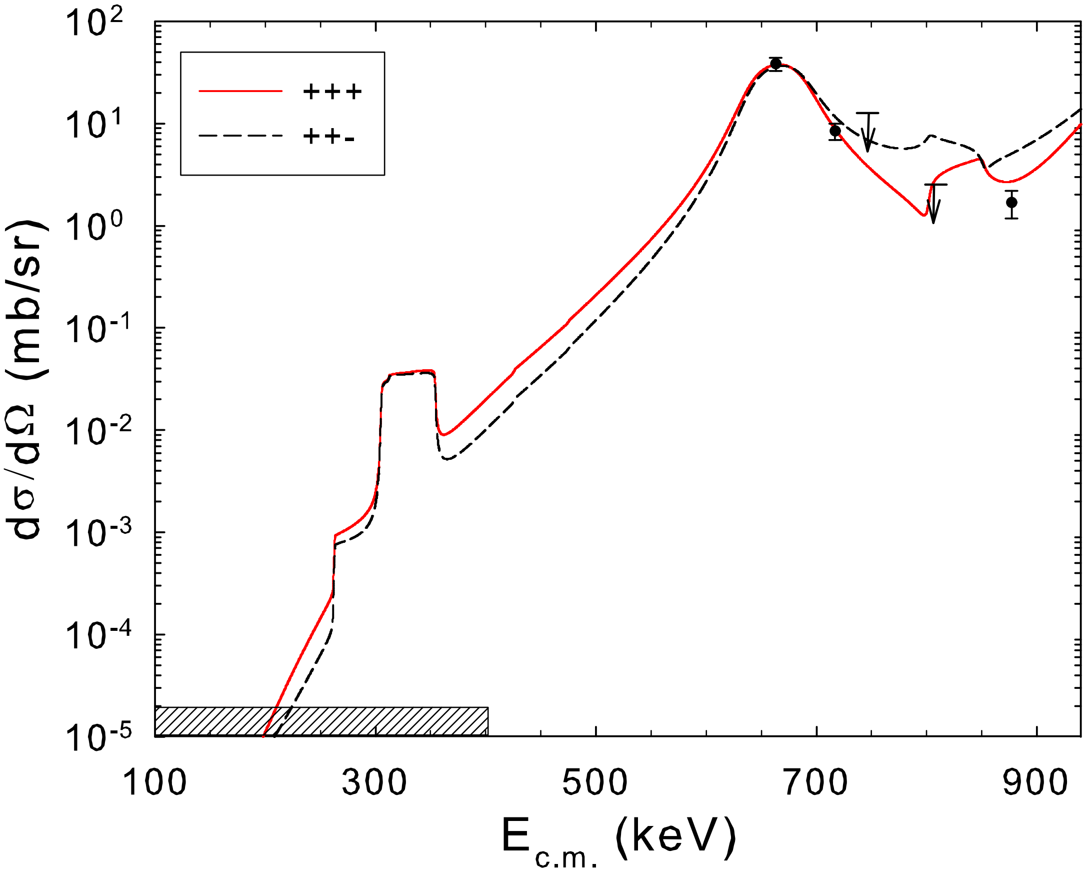

Figure 4.7: The ^{18}F(p,α)^{15}O excitation function is shown in the figure together with calculations from the R-matrix code MULTI. The theoretical cross section was calculated over the complete range of energies and then averaged over the energy loss in the target as well as over the angles covered by SIDAR ($56^\circ \leq \theta_{c.m.} \leq 138^\circ$) for direct comparison with the data. Two cases of the relative interference signs are shown for illustration (see text). Most effective energy range for novae is indicated by the shaded box.

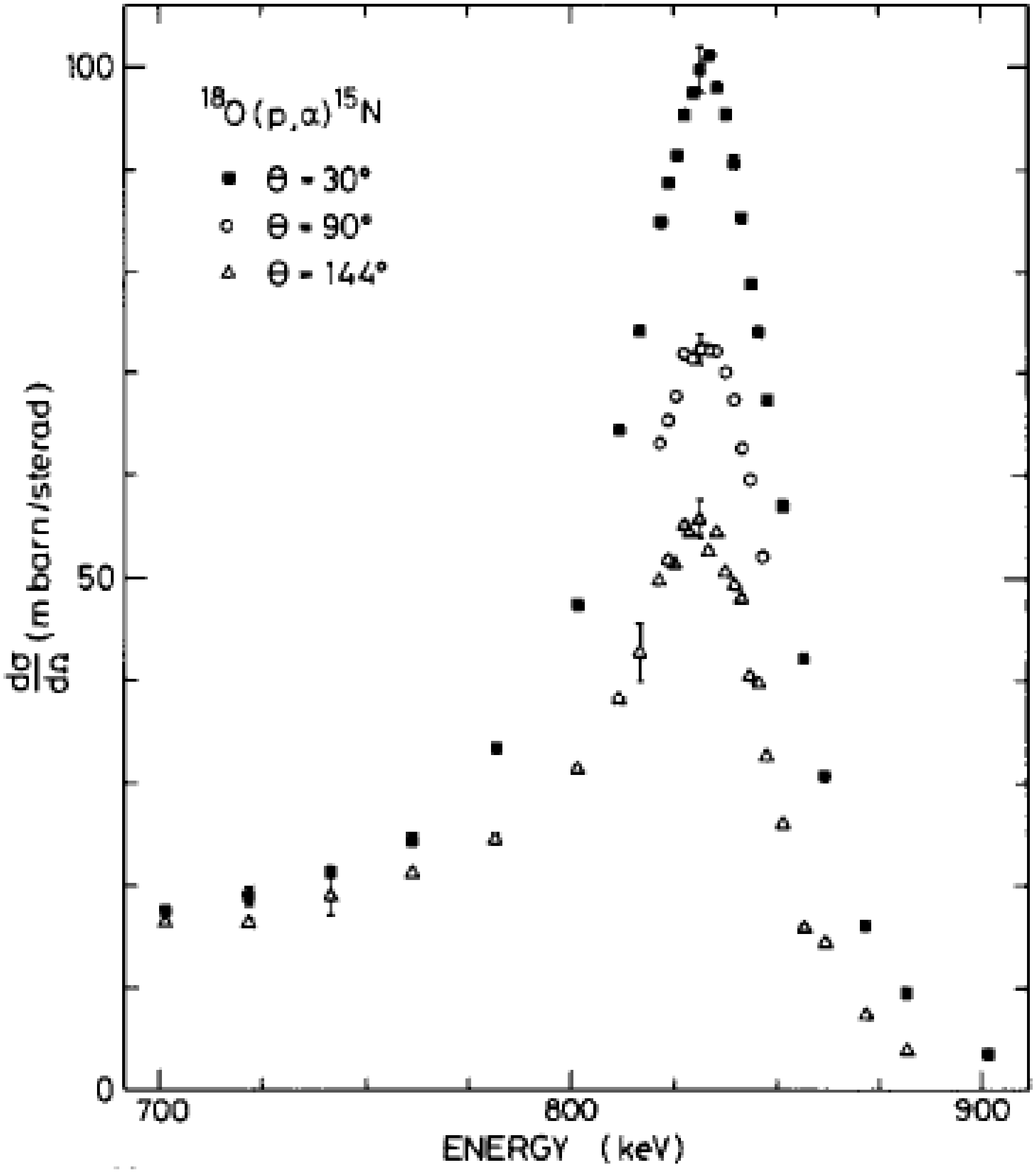

Figure 4.8: The $^{18}O(p,\alpha)^{15}N$ cross section. Figure taken from [Chr90].

Table 4.1: Summary of resonance parameters used in calculation of ^{1}H(^{18}F,α)^{15}O cross section. All these parameters were taken from Refs. [Koz05, Bar04] and references therein. Note: The proton width for the 842 keV resonance in Ref. [Bar04] is 0.9±0.9 keV (see text)

E_r (keV)	J^π	Γ_p (keV)	Γ_α (keV)	Ref.
8	$3/2^+$	2.2×10^{-37}	0.5	[Koz05]
26	$1/2^-$	1.1×10^{-20}	220.0	[Koz05]
38	$3/2^+$	4.0×10^{-15}	4.0	[Koz05]
287	$5/2^+$	1.2×10^{-5}	1.2	[Koz05]
330	$3/2^-$	2.22×10^{-3}	2.7	[Bar02]
450	$7/2^-$	1.6×10^{-5}	3.1	[Bar04]
664.7	$3/2^+$	15.2	24.0	[Bar01]
827	$3/2^+$	0.35	6.0	[Bar04]
842	$1/2^+$	0.2	23.0	[Bar04]
1009	$7/2^+$	27.0	71.0	[Bar04]
1089	$5/2^+$	1.25	0.24	[Bar04]
1122	$5/2^-$	10.0	21.0	[Bar04]

Although the relative normalization of the cross section data was well determined, determining the absolute normalization was not trivial mainly due to systematic effects such as the uncertainty in the number of hydrogen atoms in the target. This uncertainty was minimized by normalizing our cross sections to those from the well-known ^{1}H(^{18}O,α)^{15}N reaction which was simultaneously measured. The previously measured ^{1}H(^{18}O,α)^{15}N differential cross section [Chr90] is uncertain by ±15% meaning that the absolute normalization of our work is also uncertain by that amount.

To study the interference effects on the cross section, the *R*-matrix code MULTI [Nel85] was used along with the resonance parameters summarized in Table 4.1. We took $\Gamma_p = 0.2$ keV for $E_r = 842$ keV resonance in order to obtain the best fit to the current data, which is consistent with the upper limit on the width (1.8 keV) found in Ref. [Bar04]. To obtain the Γ_p value for $E_r = 842$ keV resonance, we reduced the width until the change in χ^2 value was negligible. While we use $\Gamma_p = 0.2$ keV in our calculations, any value of Γ_p smaller than this would also produce an equally good fit of our data. The theoretical cross section was calculated over the complete range of energies and then averaged over the energy loss in the target as well as over the angles covered by SIDAR for direct comparison with the data. For levels with the same J^π value, the astrophysical S-factor due to those levels can be taken from Eq.(XII. 5.15) of Lane and Thomas [Lan58], and expressed as

$$S_{tot} = |\sum_j \pm\sqrt{S_j} e^{i\delta_j}|^2, \tag{4.3}$$

where j is the resonance index, S_j is the S-factor from the resonance with index j, and δ_j is the phase [$\tan(\delta_j)=\Gamma/(2(E_j - E))$]. Each term in this sum can have either positive or negative signs [Fre65]. This ambiguity results in the observed interference in the cross section. The relative signs of the terms can not be determined theoretically but only from comparison with the measured cross section.

We take as free parameters the signs of three resonance terms for the $E_{c.m.} = 8$, 38, and 665 keV resonances. The other $J^\pi = 3/2^+$ resonance at $E_{c.m.} = 827$ keV was not included because the effect from this resonance was small resulting from its small reduced width. The results show that four out of the eight possibilities ('plus' and 'minus' signs for each term) could be ruled out. The only combination of signs consistent with our data have the 665-keV resonance term as positive [i.e., (+++), (+−+), (−++), (−−+) where the signs in parenthesis represent the signs of the 8-, 38-, and 665-keV resonances, respectively, in the sum in Eq.(4.3)]. All four of these possibilities produce nearly identical cross sections above the 665-keV resonance. In Figure 4.7, we show the clear rejection of the cases with a negative sign for the 665-keV resonance term. The signs of the other two resonances, $E_{c.m.} = 8$ and 38 keV, do not strongly affect the cross section above 665-keV. Interference effects from these resonances are, however, more important at the lower energy range ($E_{c.m} \leq 600$ keV)

Table 4.2: χ^2 values for the eight possible combinations.

Combinations	χ^2
$+++$	4.00
$-++$	3.23
$+-+$	1.16
$--+$	1.00
$++-$	72.19
$-+-$	38.45
$+--$	40.67
$---$	48.04

as shown in Figure 4.9. Effects from higher-lying $3/2^+$ resonances (such as a mirror to the 9.204-MeV ^{19}F level) were also considered but found to be negligible. χ^2 values for the eight possible combinations are quantified in Table. 4.2.

New upper limits on the proton widths (Γ_p) of the $E_{c.m.}$ = 827 and 842 keV resonances have also been set. For a given set of resonance parameters, the upper limits on Γ_p were calculated at 90% confidence level from the χ^2 distribution. Upper limits were found to be $\Gamma_p \leq 1.17$ keV at $E_{c.m.}$ = 827 keV and $\Gamma_p \leq 1.65$ keV at $E_{c.m.}$ = 842 keV. The upper limit at $E_{c.m.}$ = 842 keV is consistent with the previously determined values from a ^{18}F(p,p)^{18}F measurement in Ref. [Bar04], while the other upper limit is less stringent than the previous one.

Calculations for the astrophysical ^{18}F(p,α)^{15}O S-factor are shown in Figure 4.9. Our measurements provide the first experimental constraints on the signs of the interference between $3/2^+$ resonances. There are still considerable uncertainties in the signs for the other resonances, but measurements of the cross section between the 330-keV and the 665-keV resonances along with this work would allow for a nearly complete characterization of the interference. This is illustrated in Figure 4.9 showing the remaining possibilities for the S-factor depending on the interference signs for the 8- and 38-keV resonances.

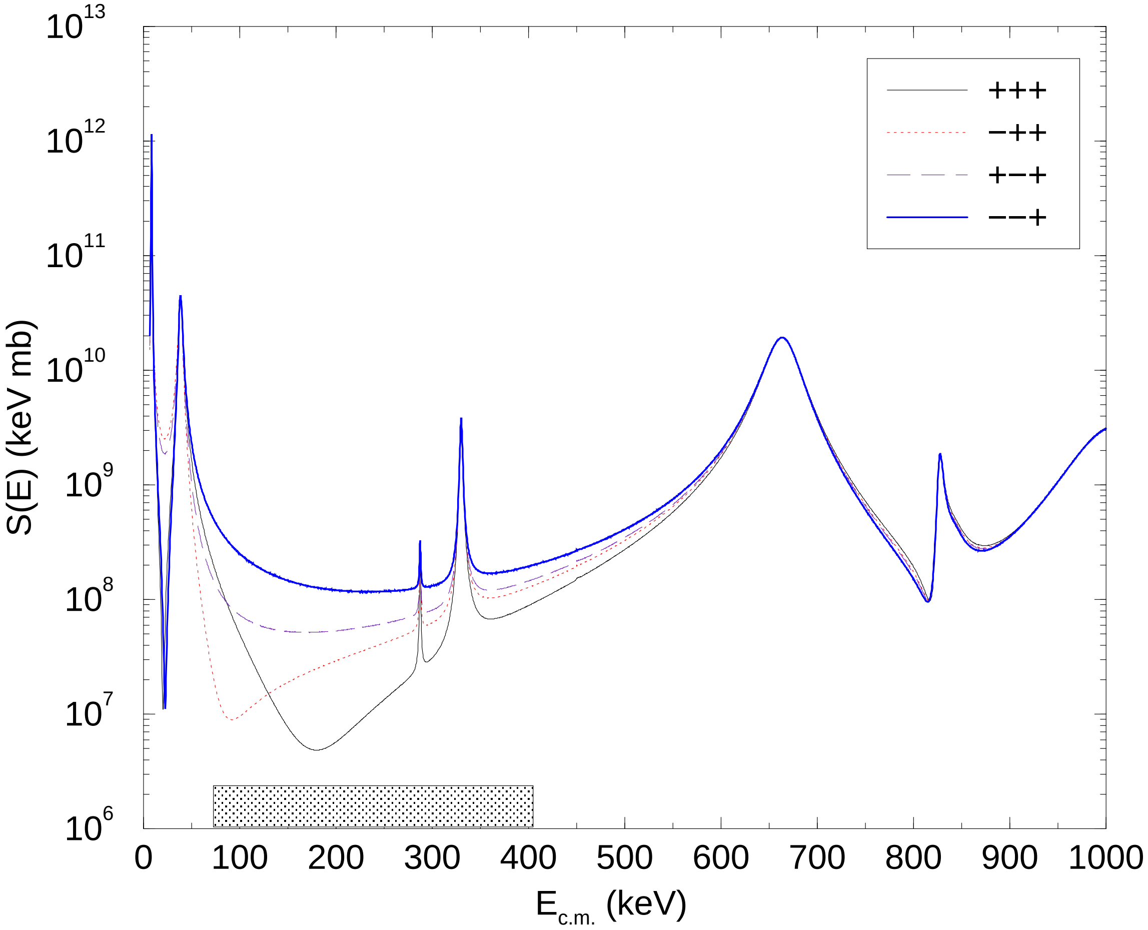

Figure 4.9: Astrophysical S-factor vs. center of mass energy plots for allowed four possibilities. The signs of reduced widths for the $E_{c.m.} = 8$, 38, and 665 keV resonances are shown in the legend. The most effective energy range for novae is also indicated.

4.3 Astrophysical Implications

To investigate how the uncertainty in interference propagates to uncertainties in ^{18}F production in novae, we have performed element synthesis calculations in the framework employed in the *Computational Infrastructure for Nuclear Astrophysics* [Infra]. Similar to Ref. [Par03], a nuclear reaction network [Hix99] containing 169 isotopes from ^{1}H to ^{54}Cr was used with nuclear reaction rates from the REACLIB [Rau01] database. Thermodynamic histories (time histories of the temperature and density) from one-dimensional hydrodynamic calculations were extracted for nova outbursts on a 1.35 $M_\odot$ ONeMg white dwarf [Sta98]. Reaction rate variations in the $^{18}F(p,\alpha)^{15}$O reaction do not appreciably change the nuclear energy generation, and thus this decoupling of nuclear and hydrodynamical effects is valid. The ejected envelope is divided into 28 zones, each with its own thermodynamic history. Separate reaction network calculations were carried out within each zone, and the final abundances determined by summing each zone's contribution to the total envelope mass. We find that the uncertainty in the ^{18}F(p,α)^{15}O reaction rate due to interference effects produces roughly a factor of 2 variation in the amount of ^{18}F produced in the calculation, with the largest variation occurring in the innermost, hottest zone where a factor of 18 variation was produced. The results are shown in Figure 4.10.

In conclusion, the ^{18}F(p,α)^{15}O reaction rate was uncertain partly because of the lack of experimental knowledge about the relative signs of the interference of three $3/2^+$ resonances. By measuring the ^{1}H(^{18}F,α)^{15}O cross sections in the energy range of $E_{c.m.}$ = 663-877 keV using radioactive ^{18}F beams at the HRIBF, we provide the first experimental constraints on the interference effects. Our results show that the uncertainty in the reaction rate for the temperature range 0.3 GK $\leq T \leq$ 0.6 GK is reduced by up to 37% compared to previous work [Koz05] (see Figure 4.11). We also

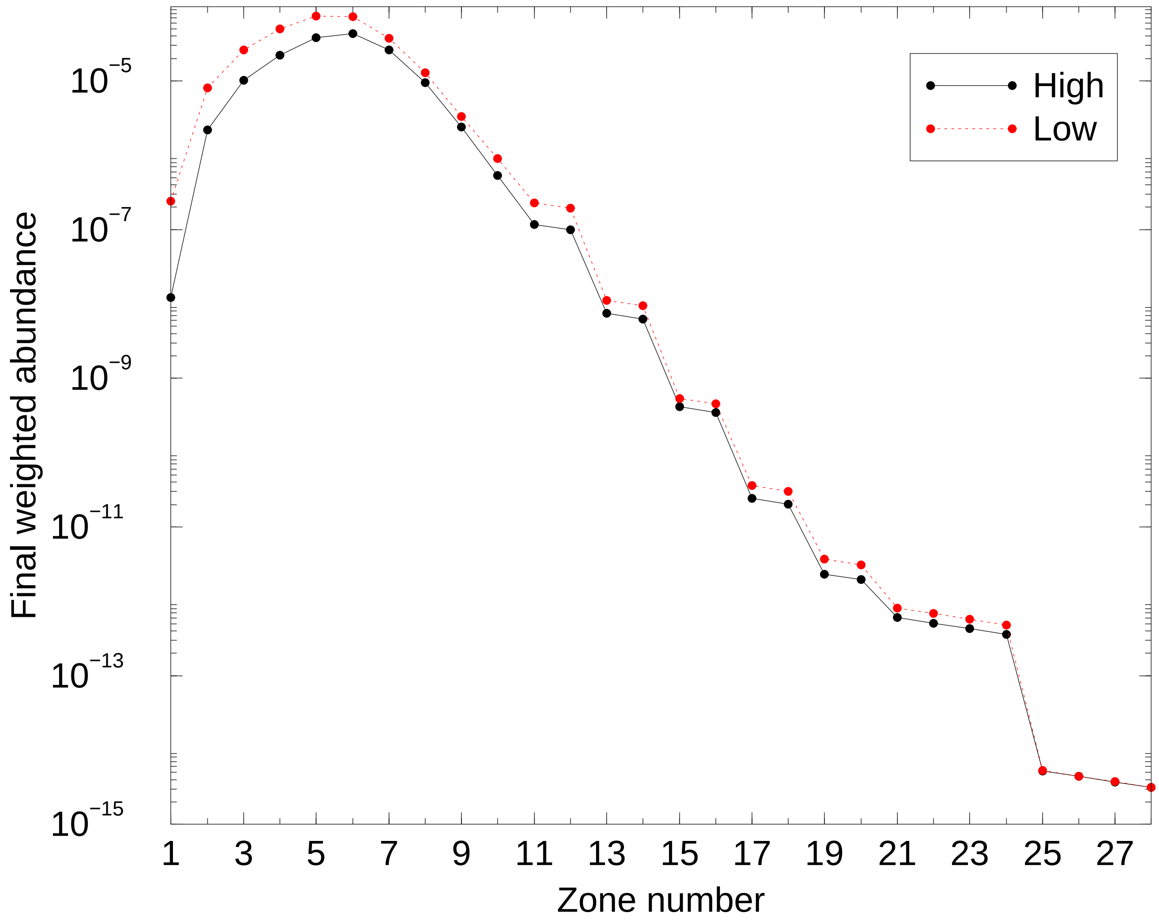

Figure 4.10: Final weighted abundances in ^{18}F at each zone. The lowest and the highest abundances at each zone are caused by the highest and the lowest reaction rates confined by present work.

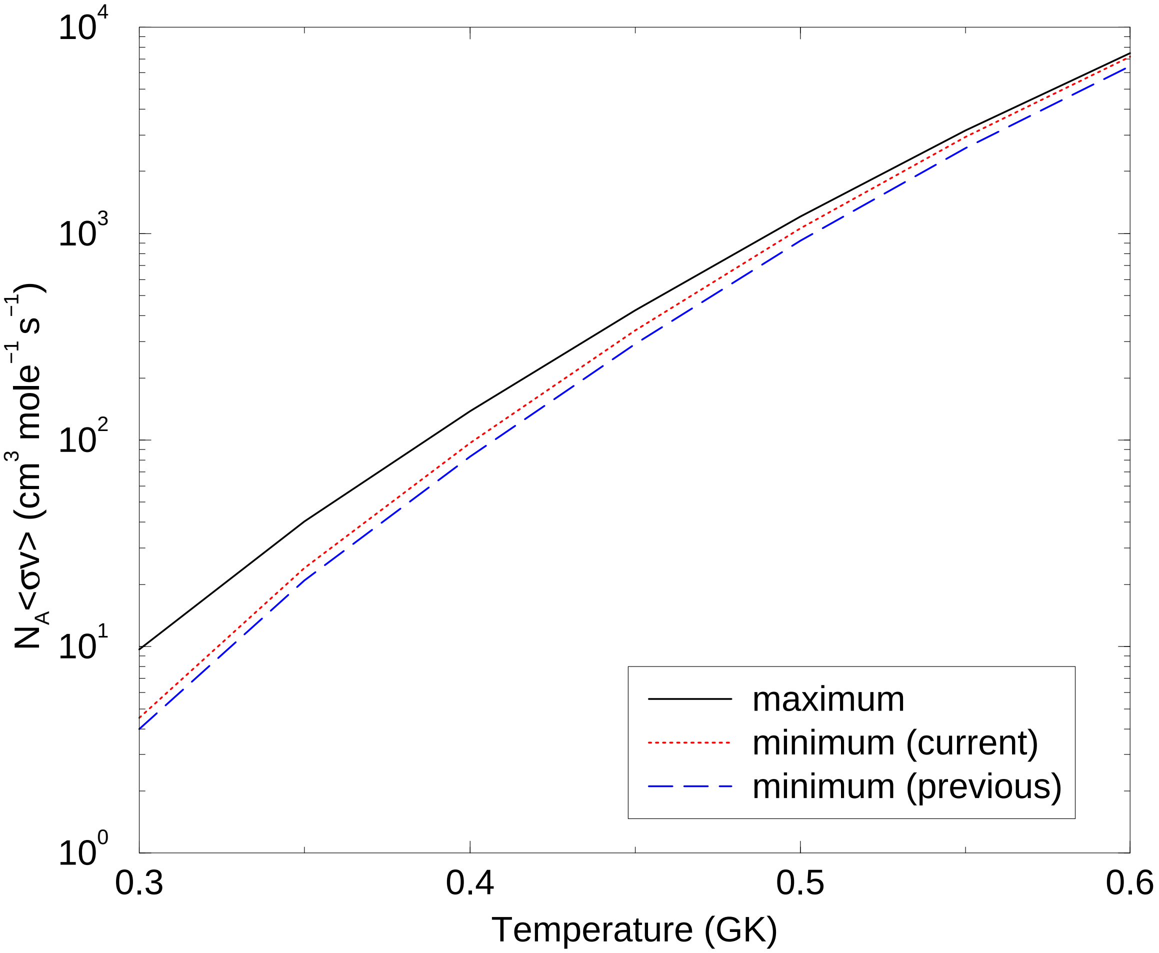

Figure 4.11: Reaction rates were calculated at nova temperatures. Solid line shows the highest reaction rate confined by present work, while dotted and dashed line show the lowest rate from present work and Ref. [Koz05], respectively.

set new upper limits on proton widths at $E_{c.m.}$ = 827 keV ($\Gamma_p \leq 1.17$ keV), and $E_{c.m.}$ = 842 keV ($\Gamma_p \leq 1.65$ keV).

Chapter 5

^{2}H(^{7}Be,^{3}H)^{6}Be Measurements

5.1 Motivation

The *pp* chain (Sec. 1.2) is responsible for the energy production of the sun and stars with masses less than a few times that of the sun. The process converts four protons into a ^{4}He nucleus via multiple nuclear reactions, releasing 27 MeV of energy. The ^{3}He nuclei produced during the *pp* chain are themselves involved in a number of reactions, including ^{3}He(d,p)^{4}He and ^{3}He(^{3}He,2p)^{4}He, which are responsible for destruction of ^{3}He and the production of ^{4}He. Since the abundance of deuterium in a star is extremely small, the latter reaction plays a more crucial role in understanding the destruction of ^{3}He [Rol88]. Also, this reaction strongly affects the calculated neutrino luminosity from the sun [Bon99]. Because of its importance, the ^{3}He(^{3}He,2p)^{4}He reaction has been studied several times at a variety of energies [Jun98,Bon99,Kud04]. Figure 5.1 shows one of these measurements.

Despite its importance, the low cross section of ^{3}He(^{3}He,2p)^{4}He at energies corresponding to stellar temperatures makes experimental studies difficult. Previous

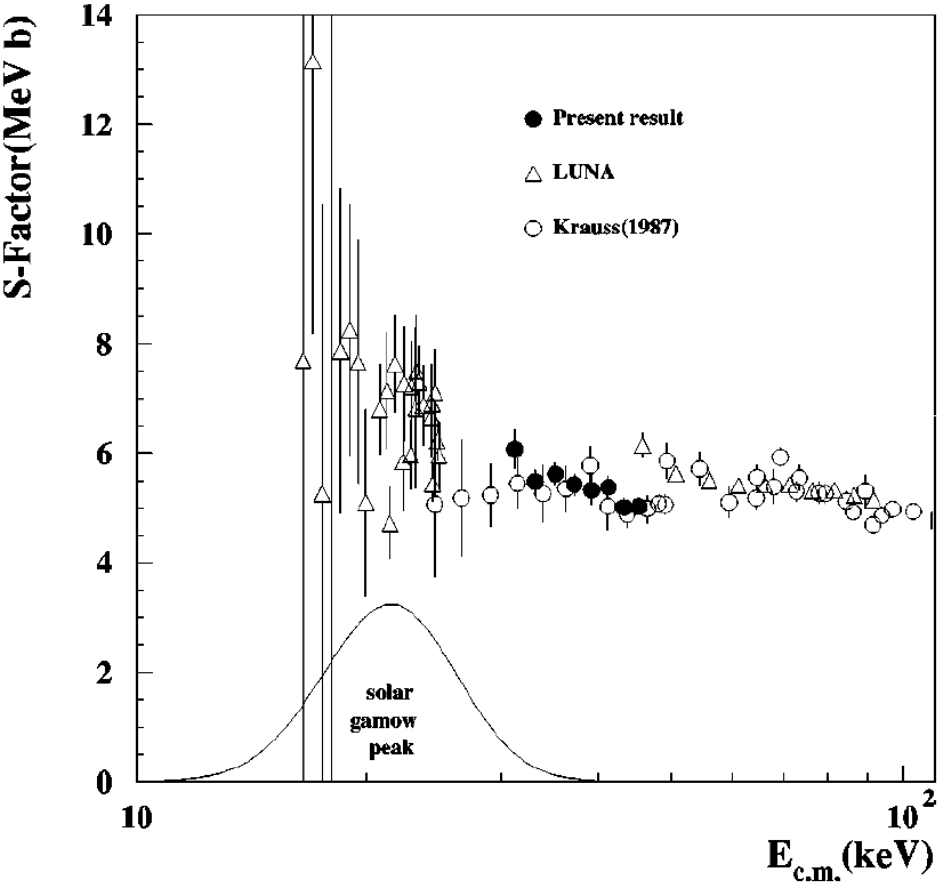

Figure 5.1: The astrophysical S-factors of the ^{3}He(^{3}He,2p)^{4}He reaction from previous measurements. Figure taken from [Kud04].

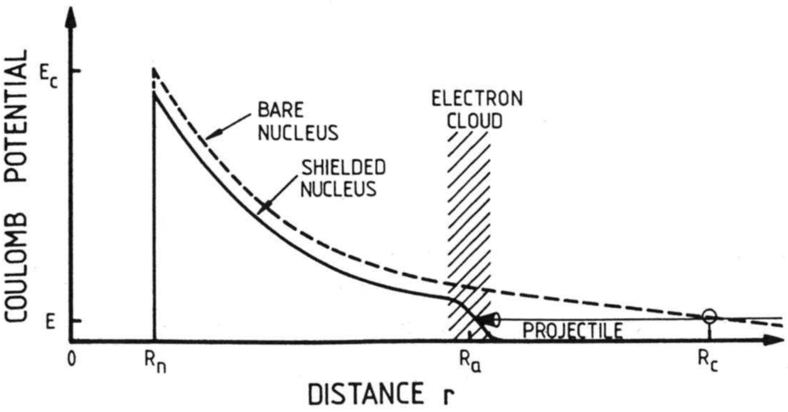

Figure 5.2: The electron screening effect is illustrated. Figure taken from [Rol88].

measurements have demonstrated a rise in the ^{3}He(^{3}He,2p)^{4}He S-factor at low energies [Bon99, Jun98, Kud04]. This could be due to a low energy resonance in the ^{3}He + ^{3}He (^{6}Be) system, or be due to the electron screening (see below). Therefore, searches for such a resonance are important in understanding the ^{3}He(^{3}He,2p)^{4}He reaction and the electron screening effect.

One motivation for studies of low energy cross sections is the electron screening effect. Under typical laboratory conditions, target nuclei are not bare but are in the form of atoms. Electrons around the target shield the nucleus from being seen by the projectile and generate a "screening" potential. As a result, the repulsive Coulomb potential is very small outside the atomic radius. This situation is illustrated in Figure 5.2, which is adopted from [Rol88]. The beam sees no Coulomb field until it comes within the atomic radius. Even though the distance between the target and the beam is small, the Coulomb barrier that the projectiles feel is less than that of bare nuclei. The effective Coulomb barrier can be written as

$$E_{eff} = \frac{Z_1 Z_2 e^2}{R_n} - \frac{Z_1 Z_2 e^2}{R_a}, \tag{5.1}$$

where R_n and R_a are the nuclear and atomic radii, respectively. The absolute value of the second term in right hand side is defined as the screening potential, U_e.

The adiabatic limit ($v_{\text{projectile}} \ll v_{\text{orbiting electrons}}$) of the electron screening potential (U_{ad}) is the difference in electron binding energies between the compound atom and the colliding atoms, and gives the maximal value of the potential because it corresponds to the maximal energy that can be transferred from the electrons to the nuclear motion. U_{ad}, therefore, can be expressed as [Cas96]

$$U_{ad} = E(A+B) - E(A) - E(B), \tag{5.2}$$

where A and B represent the two atomic systems (reactants), $A + B$ means the compound system, and $E(i)$ are the binding energies. At energies of astrophysical interest, this should be the limiting value of U_e. However, the LUNA study of the ^{3}He(^{3}He,2p)^{4}He reaction [Jun98] found arise in the S-factor at low energies that could be explained by a screening potential of 490 eV, which was much higher than the adiabatic limit (240 eV). The reasons for these discrepancies are not understood yet, but a low energy resonance in the ^{3}He + ^{3}He system could account for some of the observed rise in the cross section at low energies. The LUNA collaboration searched for such a resonance and concluded that a very narrow resonance in the interval of 9 to 20 keV with resonance width $\leq$ 1 keV was not excluded by their measurements [Jun98].

The nuclear levels in ^{6}Be are critical to understanding the behavior of the ^{3}He(^{3}He, 2p)^{4}He cross section at low temperatures. The level structures of some of the A=6 nuclei are shown in Figure 5.3, which is adopted from [Til02]. In the ^{6}Be nucleus, no excited states have been observed above the first 2^+ state at E_x = 1.67 MeV up to 23 MeV. But there is considerable evidence to support the presence of unknown

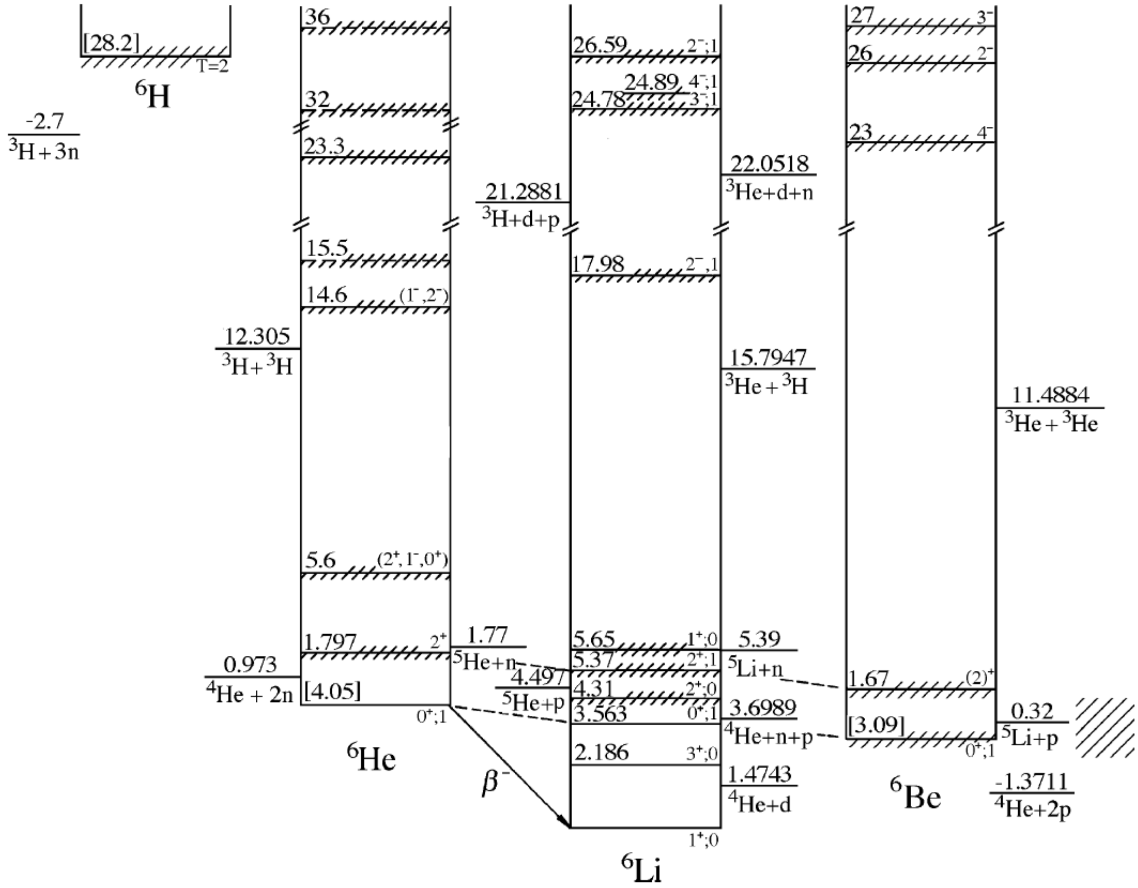

Figure 5.3: The isobar diagram for A=6 nuclei.

excited states in ^{6}Be. First of all, in the mirror nucleus ^{6}He two excited states have been established below the $t + t$ threshold at $E_x = 12.3$ MeV. Secondly, a recent measurement at Notre Dame University found tentative evidence for a ^{6}Be level at 9.6 MeV [Gui03].

Whether a state or a resonance is observed in an experiment depends on how strongly its wave function overlaps with the wave function of target and/or projectile used in a particular reaction. This is because the reaction rate depends on the properties of the interaction potential described by the Hamilton operator H_{int} which transforms the initial state wave function ψ_i into the final state wave function ψ_f. Thus, a possible reason why no excited states in ^{6}Be were previously found is the particular choice of reactions studied [Fet75, Tim99]. For example, an effort was made to find the hypothetical excited 0^+ level in ^{6}Be from decay through the channel $^6\mathrm{Be}^* \rightarrow {}^3\mathrm{He} + {}^3\mathrm{He}$ using the ^{6}Li(^{3}He, ^{3}H)^{6}Be reaction [Fet75]. However, ^{6}Be seemed to have a low probability of excitation in that reaction, and thus no states were found.

5.2 Measurements and Data Analysis

A search for the missing ^{6}Be levels was performed by studying the d(^{7}Be,t)^{6}Be reaction with the radioactive ^{7}Be beam (energy of 100 MeV, $E_{c.m.} = 22.302$ MeV) at ORNL HRIBF. In order to produce the ^{7}Be beam, ~10 MeV protons at the TUNL in North Carolina were used to irradiate a lithium pellet, and ^{7}Be was produced via the ^{7}Li(p,n)^{7}Be reaction. Then the produced ^{7}Be was separated from Li chemically at the ORNL facility. The ^{7}Be was used in a multi-sample cesium sputter ion source. An oven vaporizes Cs first, and the negative ^{7}Be ions are then sputtered from the cathode. The ^{7}Be beam is then mass analyzed, isobar separated, and injected into the 25 MV tandem accelerator. The beam was then stripped to $q = 4^+$ charge state

Table 5.1: The expected resolutions (in keV) as a function of excitation energies of ^{6}Be, lab angles, and target thickness are shown.

E_x in ^{6}Be	0 MeV		2 MeV		10 MeV		12 MeV	
t angle range	31.1°	32.0°	24.0°	32.0°	14.0°	25.0°	14.0°	20.0°
0.4 μg/cm^2	132	120	138	74	55	30	43	34
1.0 μg/cm^2	340	313	353	188	134	69	103	78
1°	334	318	241	370	204	470	231	375

at the tandem terminal, and ^{7}Li contamination in the beam was rejected by the energy-analyzing magnet (Sec. 3.2).

The 100 MeV beam of ^{7}Be at HRIBF impinged on a 1.0 mg/cm^2 CD$_2$ solid target (ρ=0.94 g/cm^2, 7.5 $\times 10^{19}$ ^{2}H atoms/cm^2). The thickness of the target requires careful consideration. If the target is too thin, too few events of interest would be detected, but the triton energy resolution is degraded when the target is too thick. So, both the yield and the resolution are crucial considerations for choosing the beam energy and thickness of the target. The expected resolutions as a function of excitation energies of ^{6}Be, lab angles, and target thickness were estimated, and are summarized in Table 5.1.

A schematic diagram of the experimental setup is shown in Figure 5.4. The average beam current on the target was $\sim 10^6$ particles per second, and total of 3.4×10^{11} ^{7}Be ions were impinged on the target. Recoil tritons from the $d(^7\text{Be},t)^6\text{Be}$ reaction were detected by SIDAR. The SIDAR was configured with 100 μm detectors backed by 500 μm detectors. Also, the wedges were arranged in a lampshade configuration to cover a large angular range ($14° \leq \theta_{lab} \leq 32°$). This angular range was chosen to optimize sensitivity around 10 MeV in excitation energy of ^{6}Be. The kinematics calculation of the reaction is shown in Figure 5.5.

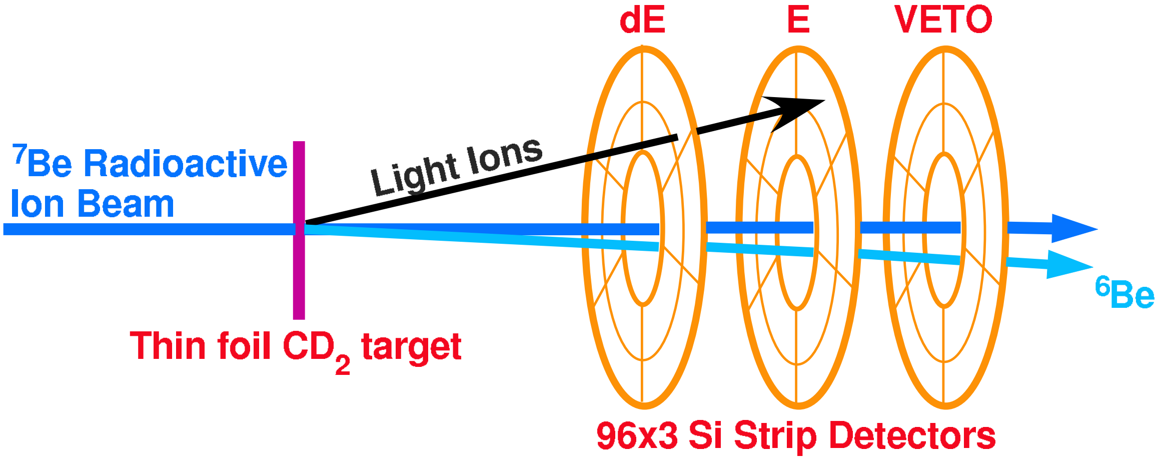

Figure 5.4: A schematic diagram of the experimental setup.

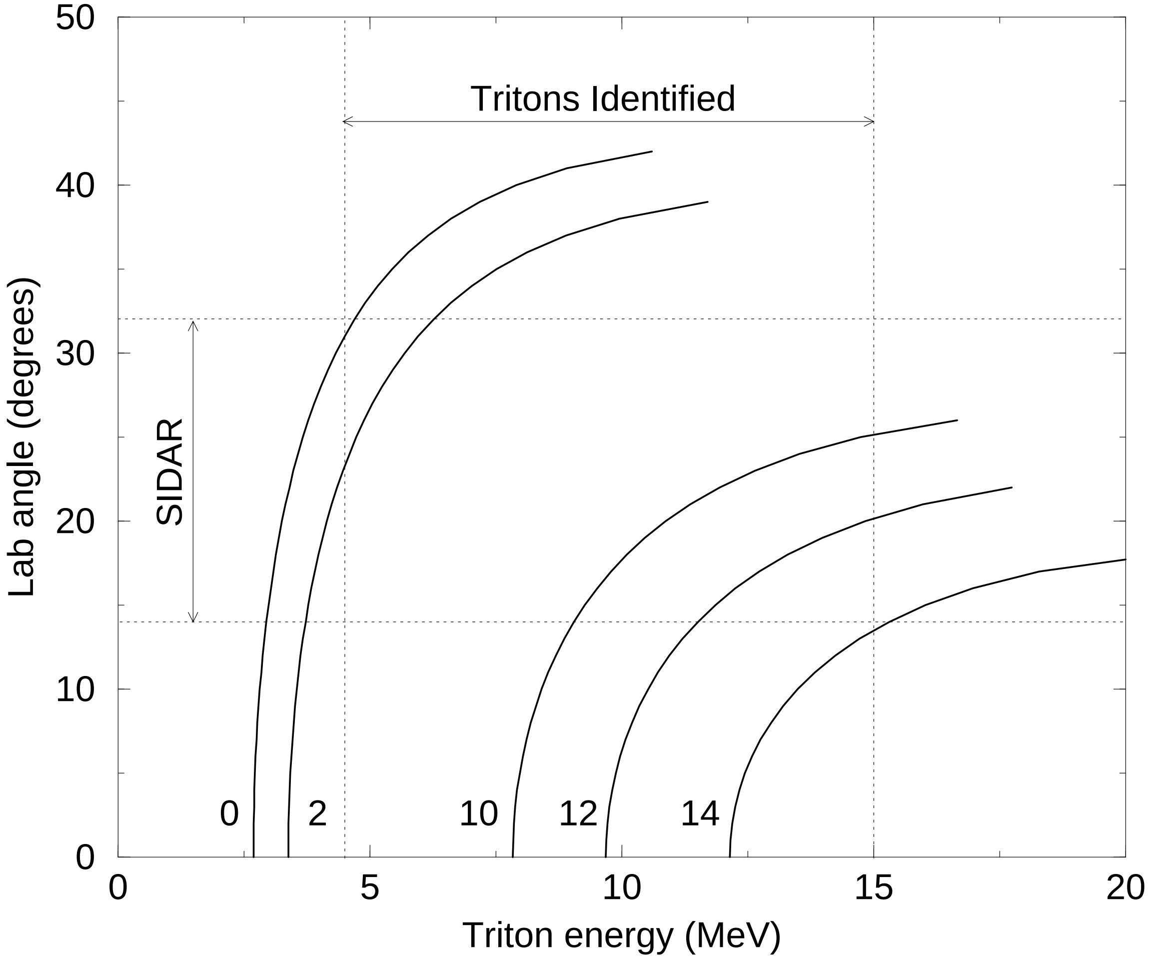

Figure 5.5: The kinematics calculation of the $d(^7\text{Be}, t)^6\text{Be}$ reaction. Curves are labeled by ^{6}Be excitation energy. The angular range ($14^\circ \leq \theta_{lab} \leq 32^\circ$) was chosen to optimize sensitivity around 10 MeV in excitation energy of ^{6}Be.

Two silicon strip detector arrays acted as energy-loss (ΔE) detectors (the first one, 100 μm thick), and residual energy (E) detectors (the second one, 500 μm thick), respectively, for light particles. Tritons from the reaction should penetrate the ΔE detector and stop at the E detector. The beam energy and the angles that were covered by SIDAR were chosen under this assumption. Tritons were identified by a standard energy loss technique. An example of ΔE-E plot from the current experiment is shown in Figure 5.6 (a). As seen in the figure, however, large amounts of ^{3}He particles "punch through" the E detector only partially depositing their energy and producing a "back-bending" locus that overlaps with the triton group.

To reduce this effect, another layer of detectors ("veto"-detectors, 300 μm thick) were placed behind the E detectors. The purpose of using the third layer of detectors was to detect the ^{3}He particles punching through the E detectors and to exclude these particles from the ΔE-E plot. The result of this veto condition is shown in Figure 5.6 (b). Not all punching through ^{3}He events were rejected, but a significant amount of the unwanted events were vetoed by this technique.

The SIDAR was energy calibrated by two methods. First, a calibrated ^{244}Cm source which emits alpha particles with energy of 5.8 MeV (Sec. 3.3.1) was used to illuminate the array before and after the current experiments. Also, 6- and 11-MeV deuteron beams were used for detector energy calibration. The deuteron beams impinged on a ^{197}Au target, and were scattered at full energy into the detectors. The ΔE-E plot from the deuteron beam calibration is shown in Figure 5.7.

To help identify true coincident ΔE-E events the time between ΔE and E events was measured using a time-to-amplitude converter (TAC). To determine the number of ^{2}H(^{7}Be, ^{3}H)^{6}Be events, an appropriate time coincidence (400 ns $\leq$ time difference $\leq$ 1200 ns, see Figure 5.8) was required. Unfortunately, the TAC showed no sensitivity to particle type (Figure 5.8). Next, proper ΔE-E profile was required as shown

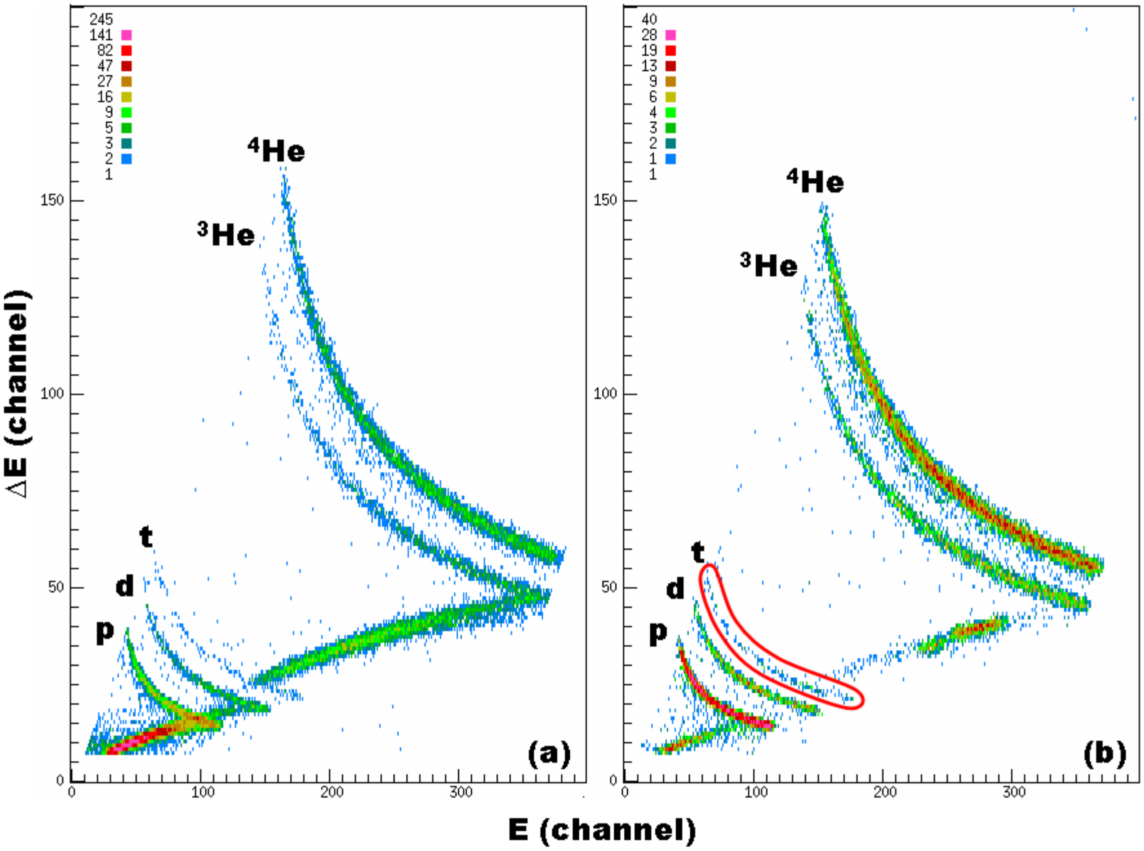

Figure 5.6: Examples of ΔE-E plots. (a) ΔE, E layers were used. (b) ΔE, E, and veto layers were used. Not all punching through ^{3}He events were excluded, but significant amount of the unwanted events were vetoed by using veto detectors.

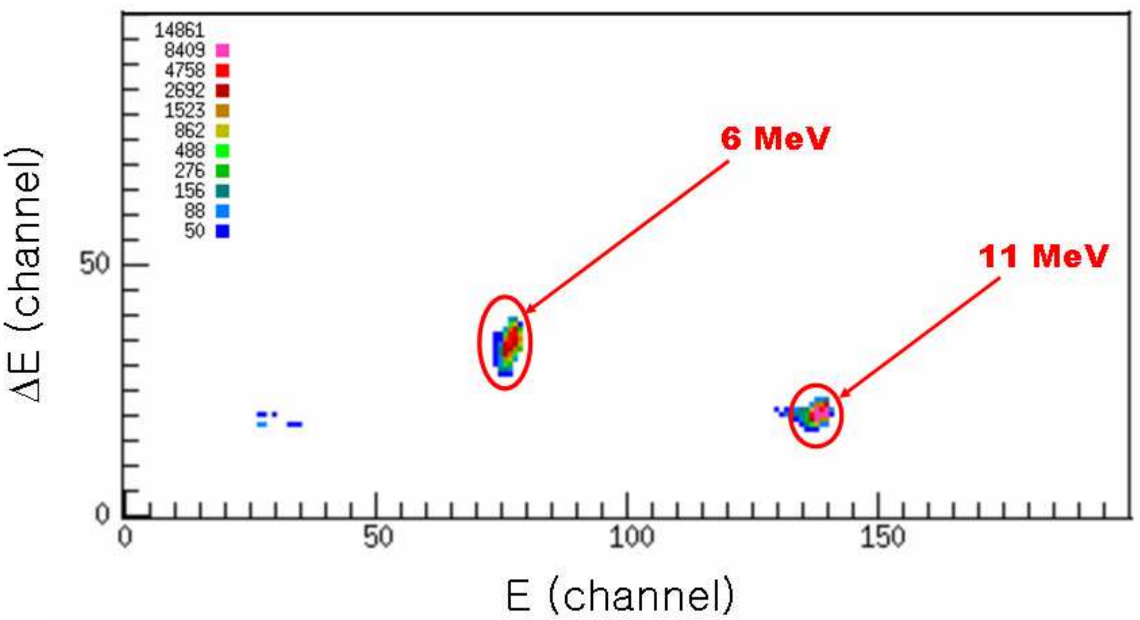

Figure 5.7: ΔE-E plot for deuteron beam on Au target. Two groups of events from 6- and 11-MeV deuteron beams are clearly identified.

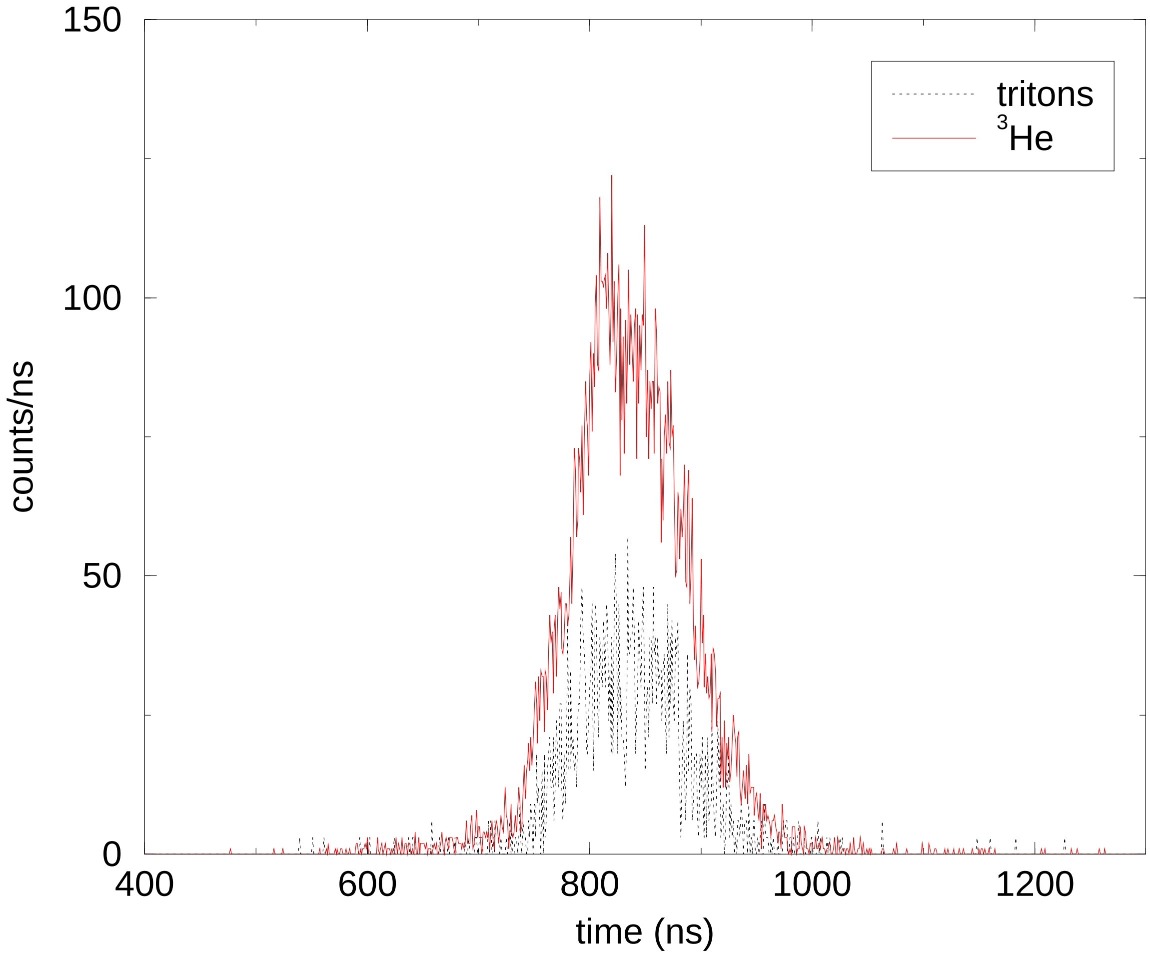

Figure 5.8: The time difference between ΔE and E events for tritons and ^{3}He particles.

in Figure 5.6 (b). Events which fell into the gate were identified as "tritons". As mentioned earlier, however, large amount ^{3}He particles also fell into this gate. Figure 5.9 shows the number of counts per channel versus ^{6}Be excitation energy ($E_{\rm Be}$) plot at $\theta_{lab} = 13.6°$.

The differential cross section measured in each strip as a function of ^{6}Be excitation energy was calculated as

$$\left(\frac{d\sigma}{d\Omega}\right)_s (E_{\rm Be}) = \frac{Y(E_{\rm Be})}{IN\Delta\Omega_s}, \tag{5.3}$$

where $Y(E_{\rm Be})$ was the number of ^{2}H(^{7}Be,^{3}H)^{6}Be events at given ^{6}Be energy, I was the number of ^{7}Be ions that impinged on the target, N was the number of deuterium atoms per unit area in the target, $\Delta\Omega_s$ was the solid angle covered by a SIDAR strip in the center of mass system. Differential cross section versus ^{6}Be excitation energy is plotted for each SIDAR strip in Figure 5.10 assuming all of the observed events are from the ^{2}H(^{7}Be,^{3}H)^{6}Be reaction.

The triton energy spectrum observed in Figure 5.9 is rather featureless indicating that direct transfer to ^{6}Be levels is not particularly strong. Other reaction mechanisms producing tritons were therefore investigated including a phase space model and three-body continuum (Chapter 2). Three reactions were included in the phase space model:

$$^7\text{Be} + d \Rightarrow \begin{cases} t + p + p +^4 \text{He} \\ t +^3 \text{He} +^3 \text{He} \\ t + p +^5 \text{Li}. \end{cases}$$

These reactions produce tritons in their exit channel, which may fall into the gate shown in Figure 5.6 (b). The phase space distribution was calculated as (Sec. 2.3.2)

$$P_i^{\rm lab}(\mu, E, E') = C_n\sqrt{E'}\left[E_i^{\rm max} - \left(E^* + E' - 2\mu\sqrt{E^*E'}\right)\right]^{\frac{3n}{2}-4}, \tag{5.4}$$

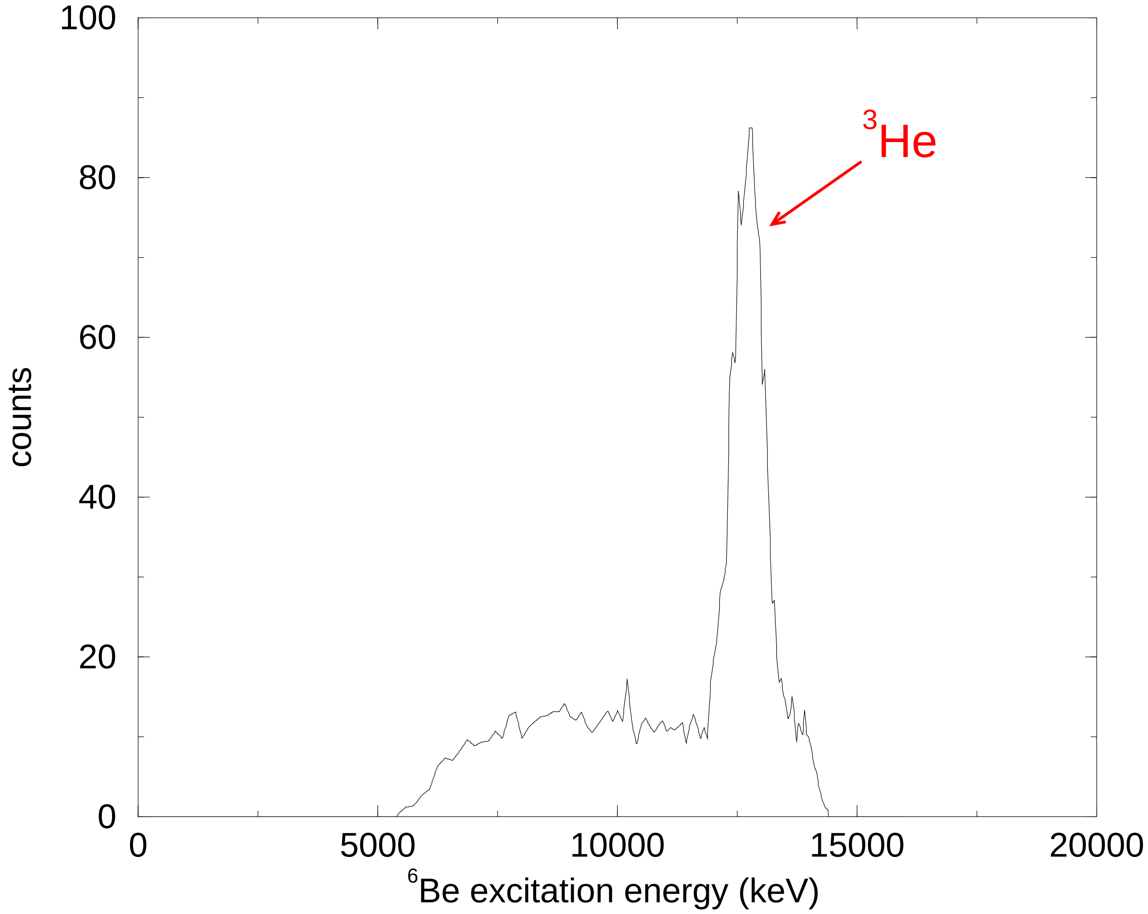

Figure 5.9: The number of counts per channel versus ^{6}Be excitation energy plot at $\theta_{lab} = 13.6°$.

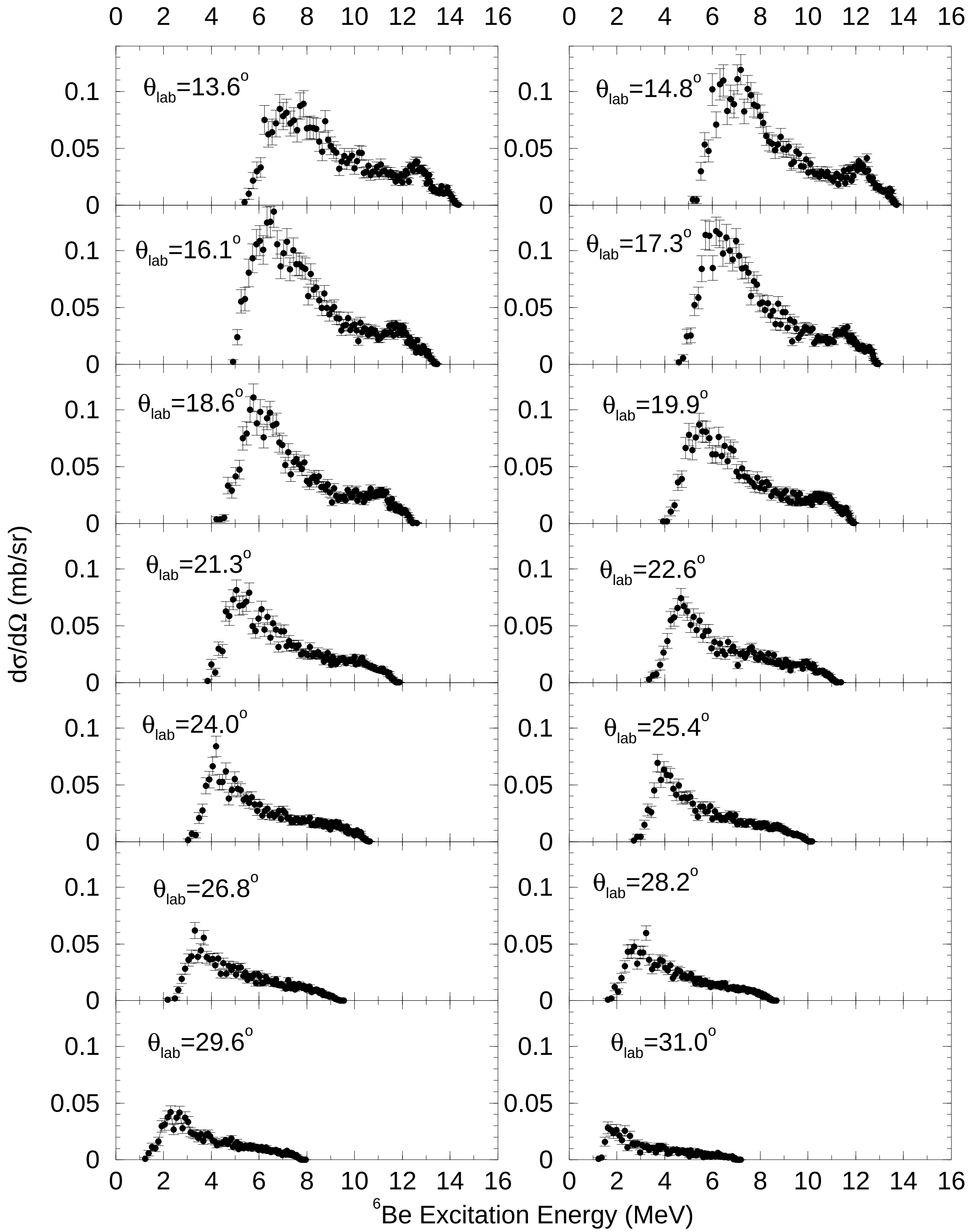

Figure 5.10: The differential cross section vs. ^{6}Be excitation energy plots for each SIDAR strip.

where all variables and constants are defined in Sec. 2.3.2. The normalization factors, C_n, are given by

$$
\begin{aligned}
C_3 &= \frac{4}{\pi(E_i^{\max})^2} && (5.5)\\
C_4 &= \frac{105}{32(E_i^{\max})^{7/2}}, && (5.6)
\end{aligned}
$$

where n is the number of particles in exit channel. The overall normalization factor is, however, still undetermined. The distributions from three reactions above are shown in Figure 5.11 as well as the total distribution as a function of ^{6}Be excitation energy. Clearly, there is very little contribution to our spectra from this phase space decay model.

Sequential decay mechanisms (Sec. 2.3.1) were considered next. The reactions that were considered by this mechanism were:

$$
{}^7\text{Be} + d \Rightarrow \begin{cases} {}^5\text{Li} + {}^4\text{He}^* = t + p + {}^5\text{Li} \\ {}^4\text{He} + {}^5\text{Li}^* = t + p + p + {}^4\text{He}. \end{cases}
$$

The energy spectra for the tritons were calculated using Eq.(2.50), and one case is shown in Figure 5.12. Also, the experimental cross section together with the energy spectrum is shown in Figure 5.13.

The data were not well described by either background process considered. Since no ^{6}Be levels were evident, we have set upper limits on the cross section to populate such levels. Widths of 0.5 and 1 MeV were assumed for the hypothetical levels in ^{6}Be nucleus, since few levels are reported in the orders of MeV in the mirror nucleus ^{6}He. While the width of level was fixed, the excitation energy could vary from 3 MeV to 11 MeV. Assuming a Gaussian distribution of tritons would be produced by such

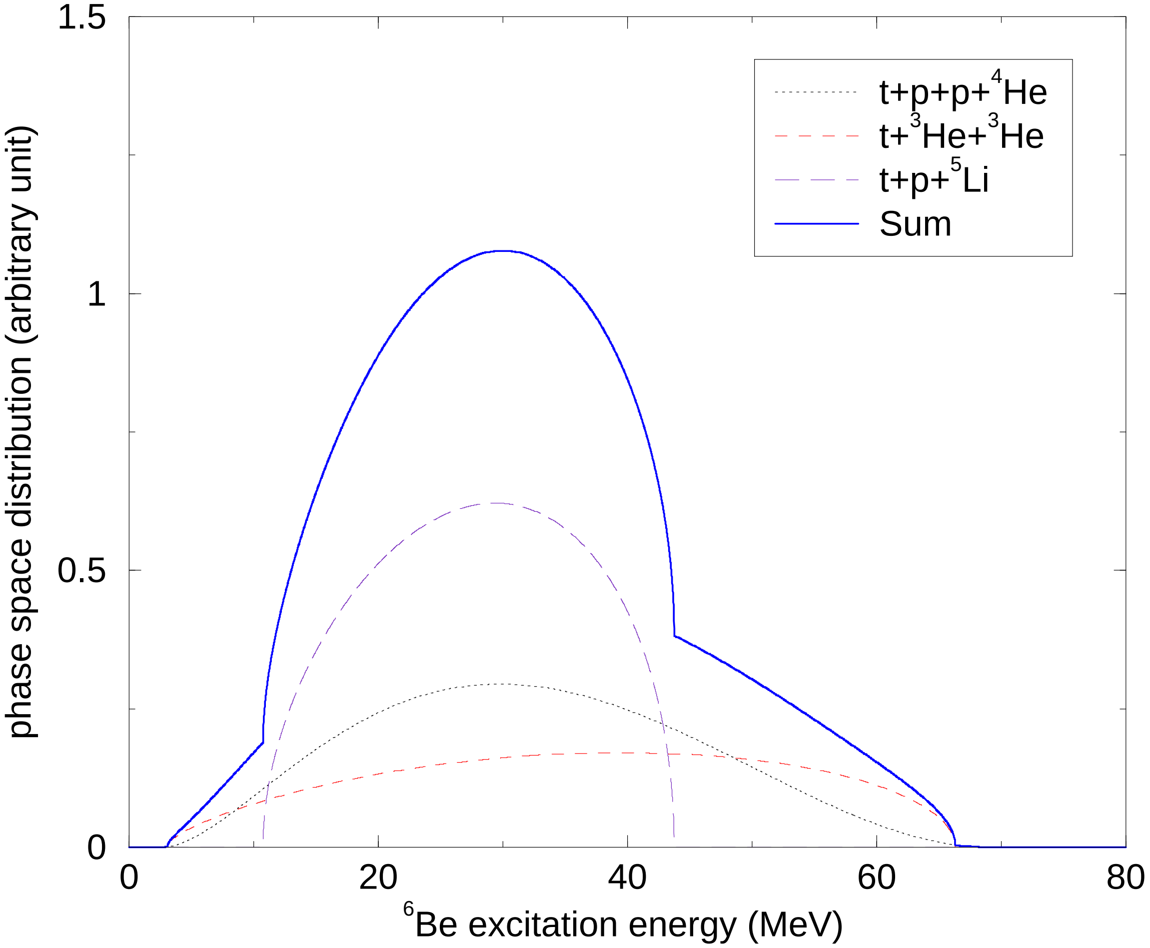

Figure 5.11: The phase space distributions for three cases at $\theta_{lab} = 13.6°$.

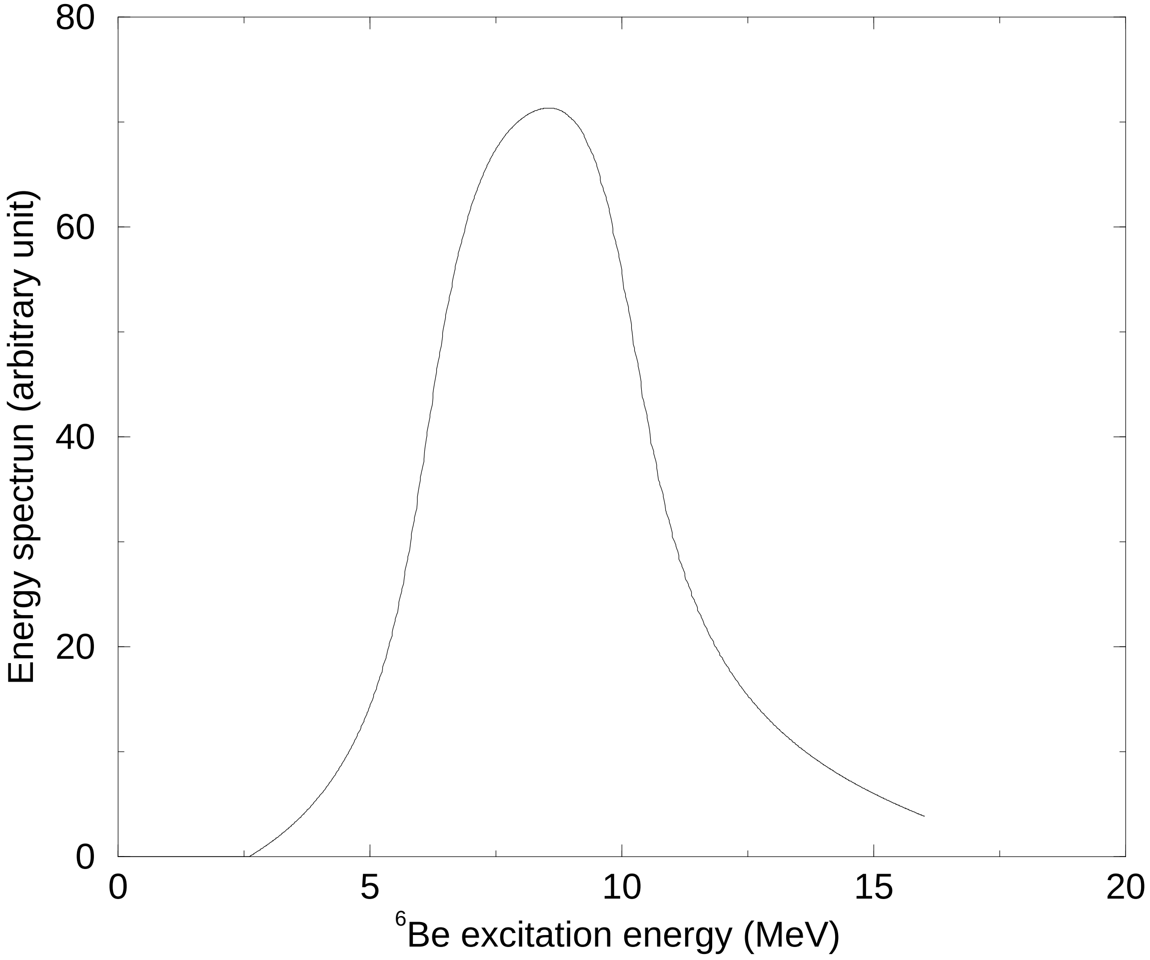

Figure 5.12: The energy spectrum for the tritons from ^{7}Be + $d \rightarrow t + p +$^{5}Li reaction. $\theta_{lab} = 13.6^{\circ}$ in this case.

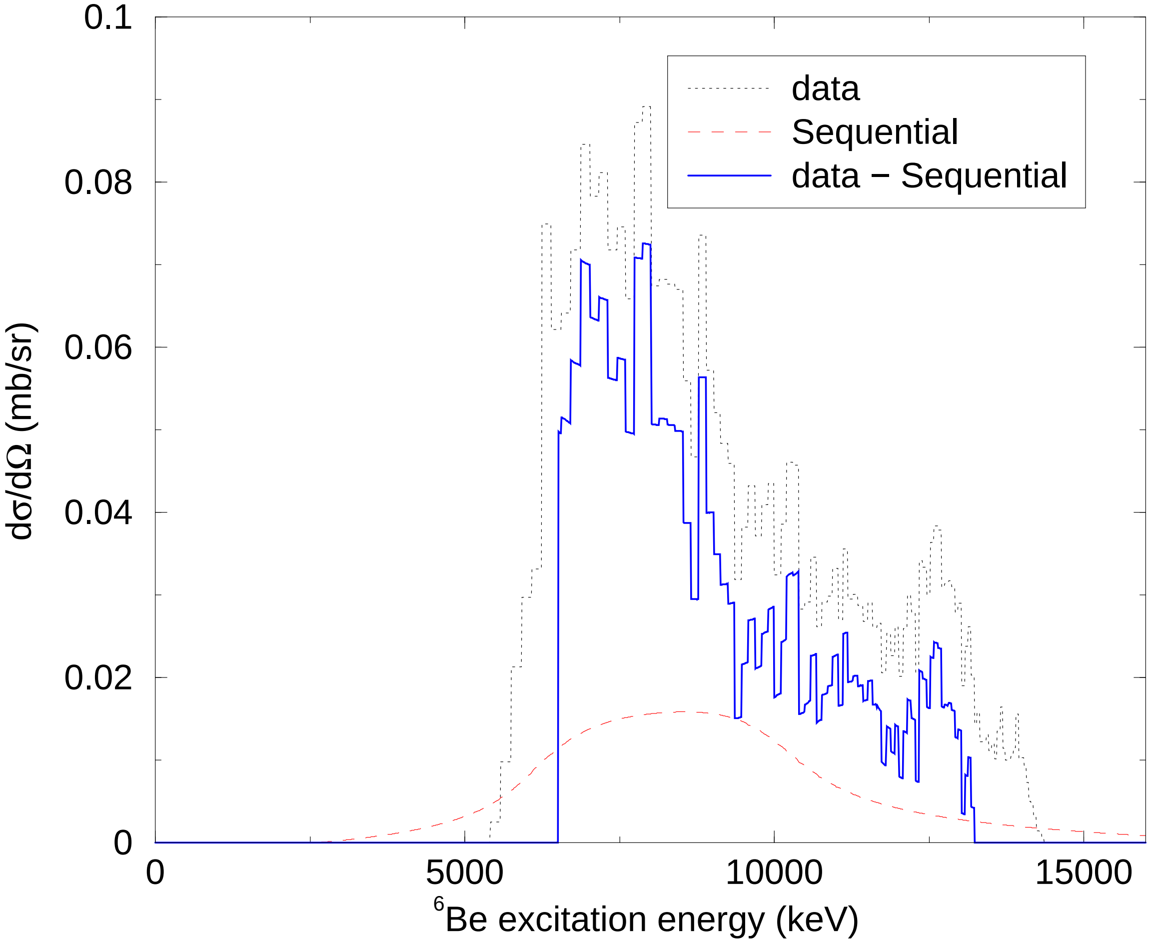

Figure 5.13: The experimental cross section data and the sequential decay energy spectrum with proper normalization factor. The blue curve shows the difference between two sets (experimental data - sequential decay energy spectrum). $\theta_{lab} = 13.6°$ in this case.

a resonance, we increased the normalization factor of the distribution until the χ^2 was increased by a prescribed amount. The range of the excitation energy (3 MeV $\leq E_{Be} \leq$ 11 MeV) was chosen such that more than 99.7 % of the Gaussian distribution fell into the energy range covered by each SIDAR strip. Results of the upper limits calculations are summarized in Table 5.2. Similar calculations assuming 1 MeV of width are also shown in Table 5.3, and one of the results is shown in Figure 5.14.

Angular distributions of the differential cross section were compared with Distorted Wave Born Approximation (DWBA) calculations using the computer code TWOFNR [Iga] with previously determined optical model parameters [ElN70]. The optical parameters are:

$$
\begin{aligned}
U &= 48.8 \text{ MeV, real volume central potential depth} \\
W &= 14.8 \text{ MeV, imaginary volume central potential depth} \\
a &= 0.57 \times 10^{-15} \text{ m, volume diffuseness} \\
r &= 1.60 \times 10^{-15} \text{ m, volume radius}
\end{aligned}
$$

Nuclear shell model calculations predict five levels in the ^{6}Be system at the energy range of 3.3 MeV $\leq E_{Be} \leq$ 23.8 MeV [Bev86]. The suggested J^π values for the five levels are $0^+, 1^+, 2^+, 3^+$. Angular momentum and parity considerations show that $l = 1$ transfers can populate these levels. Additionally, $l = 0$ transfers can populate 1^- and 2^- levels and also are considered. Calculations show that the cases with same l value produce nearly identical cross sections. The DWBA calculations for $l = 0$ and 1 are shown in Figure 5.15. In most cases, our observed cross sections are larger than the DWBA calculations indicating that a mixture of reaction mechanisms are involved.

Table 5.2: The upper limits on cross section (in mb/sr) at each angle are summarized. The width of hypothetical level in ^{6}Be nucleus is assumed 0.5 MeV, and the excitation energies of $3 \sim 11$ MeV are considered.

Angle	Levels in ^{6}Be (MeV)								
	3	4	5	6	7	8	9	10	11
13.6°	-	-	-	-	0.74	0.78	0.68	0.52	0.36
14.8°	-	-	-	-	1.12	0.93	0.69	0.49	0.34
16.1°	-	-	-	-	1.22	1.00	0.66	0.45	-
17.3°	-	-	-	-	1.25	0.84	0.56	0.38	-
18.6°	-	-	-	1.24	0.93	0.66	0.40	-	-
19.9°	-	-	-	1.06	0.76	0.52	0.35	-	-
21.3°	-	-	-	0.82	0.61	0.40	0.28	-	-
22.6°	-	-	0.84	0.57	0.40	0.33	-	-	-
24.0°	-	-	0.76	0.50	0.36	0.26	-	-	-
25.4°	-	-	0.62	0.42	0.31	-	-	-	-
26.8°	-	0.66	0.48	0.33	0.24	-	-	-	-
28.2°	-	0.55	0.38	0.26	-	-	-	-	-
29.6°	0.58	0.36	0.27	-	-	-	-	-	-
31.0°	0.25	0.19	0.13	-	-	-	-	-	-

Table 5.3: The upper limits on cross section (in mb/sr) at each angle are summarized. The width of hypothetical level in ^{6}Be nucleus is assumed 1 MeV, and the excitation energies of 4.5 $\sim$ 11 MeV are considered.

Angle	Levels in ^{6}Be (MeV)													
	4.5	5	5.5	6	6.5	7	7.5	8	8.5	9	9.5	10	10.5	11
13.6°	-	-	-	-	-	-	-	-	1.47	1.35	1.19	1.03	0.88	0.78
14.8°	-	-	-	-	-	-	-	-	1.63	1.40	1.19	1.00	0.86	-
16.1°	-	-	-	-	-	-	-	1.94	1.64	1.36	1.12	0.95	-	-
17.3°	-	-	-	-	-	-	-	1.71	1.40	1.14	0.95	0.83	-	-
18.6°	-	-	-	-	-	-	1.58	1.30	1.06	0.88	0.78	-	-	-
19.9°	-	-	-	-	-	-	1.27	1.06	0.89	0.77	-	-	-	-
21.3°	-	-	-	-	-	1.20	1.00	0.83	0.71	-	-	-	-	-
22.6°	-	-	-	-	0.98	0.84	0.74	0.66	-	-	-	-	-	-
24.0°	-	-	-	-	0.86	0.73	0.64	-	-	-	-	-	-	-
25.4°	-	-	-	0.87	0.74	0.65	-	-	-	-	-	-	-	-
26.8°	-	-	0.81	0.68	0.59	-	-	-	-	-	-	-	-	-
28.2°	-	0.78	0.65	-	-	-	-	-	-	-	-	-	-	-
29.6°	0.63	-	-	-	-	-	-	-	-	-	-	-	-	-

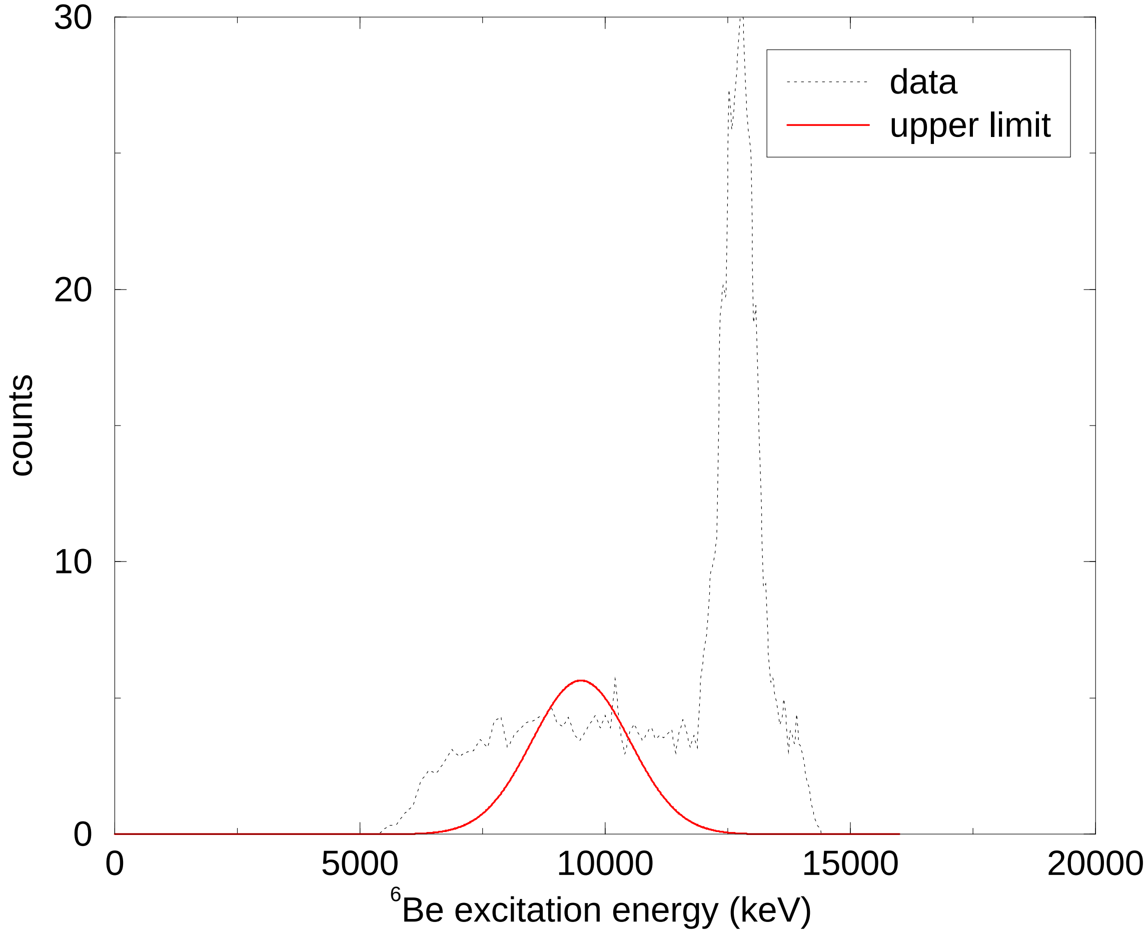

Figure 5.14: The upperlimit on cross section is shown together with experimental data at $\theta_{lab} = 13.6°$. $E_x = 9.5$ MeV and width of 1 MeV are assumed for the hypothetical level.

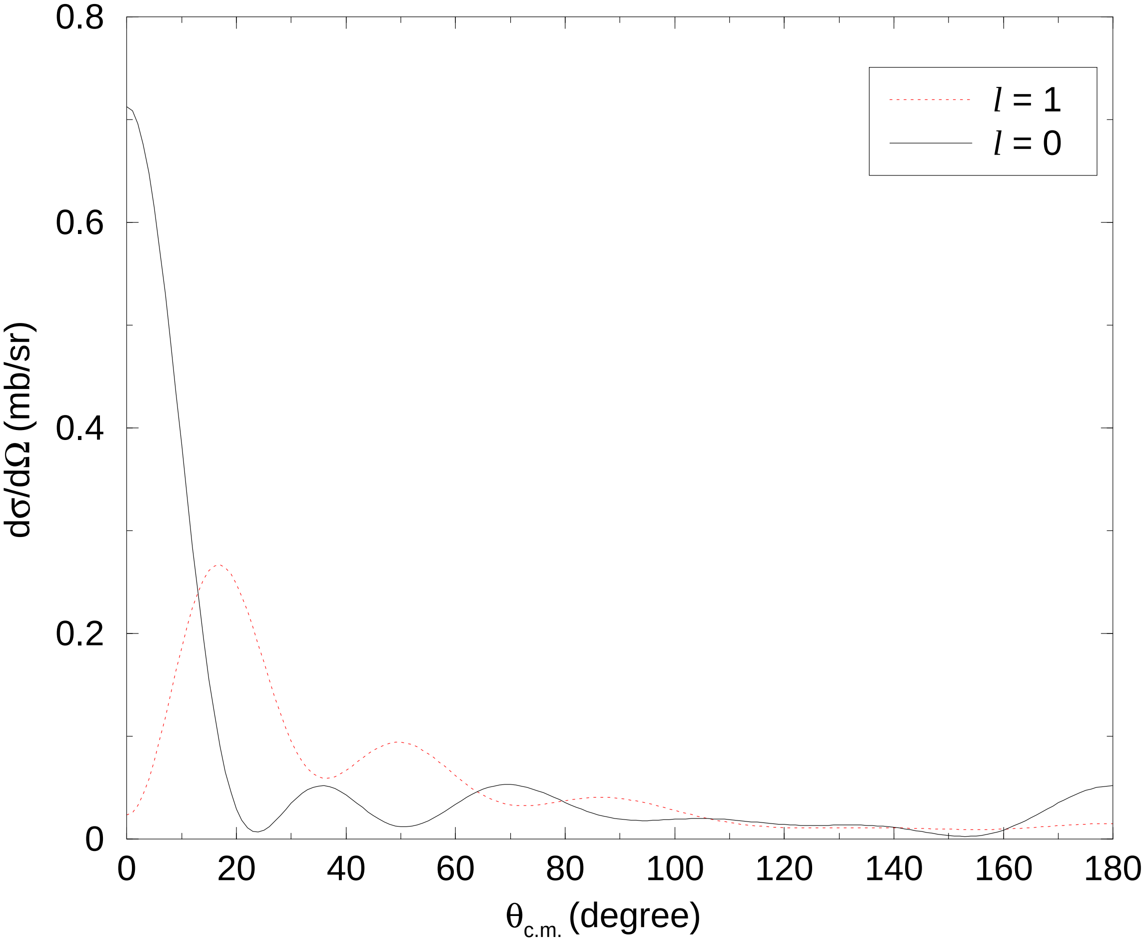

Figure 5.15: The DWBA calculations for l=0 and 1. E_x = 9.6 MeV and width of 1 MeV are assumed for the hypothetical level.

Chapter 6

Conclusions

Radioactive ion beams of ^{18}F were used for the study of the astrophysically important ^{18}F(p,α)^{15}O reaction. The reaction rate was uncertain partly because of the lack of experimental knowledge about the relative signs of the quantum mechanical interference of three lower-lying $3/2^+$ resonances. By measuring the ^{1}H(^{18}F,α)^{15}O cross sections in the energy range of $E_{c.m.}$ = 663-877 keV at the ORNL HRIBF, and by comparing the experimental results with theoretical calculations, we provided the first experimental constraints on the interference effects. The results show that four out of the eight possibilities in interference, which are caused by the signs of the 8-, 38-, and 665-keV resonances, could be ruled out. The only combination of signs consistent with our data have the 665-keV resonance term as positive. There are still considerable uncertainties in the signs for the other resonances, but measurements of the cross section between the 330-keV and the 665-keV resonances along with present work would allow for a nearly complete characterization of the interference. Our results show that the uncertainty in the reaction rate at the temperature range 0.3 GK $\leq T \leq$ 0.6 GK is reduced by up to 37% compared to previous work. We have performed element synthesis calculations in the framework employed in the *Computational Infrastructure for Nuclear Astrophysics* to investigate how the uncertainty in interference propagates to uncertainties in ^{18}F production in novae. We find that the current uncertainty in the ^{18}F(p,α)^{15}O reaction rate due to interference effects produces roughly a factor of 2 variation in the amount of ^{18}F produced in the calculation. New upper limits on the proton widths (Γ_p) of the $E_{c.m.}$ = 827 and 842 keV resonances have also been set. For a given set of resonance parameters, the upper limits on Γ_p were calculated at 90% confidence level from the χ^2 distribution. Upper limits were found to be $\Gamma_p \leq 1.17$ keV at $E_{c.m.}$ = 827 keV and $\Gamma_p \leq 1.65$ keV at $E_{c.m.}$ = 842 keV. The upper limit at $E_{c.m.}$ = 842 keV is consistent with the previously determined values from a ^{18}F(p,p)^{18}F measurement, while the other upper limit is less stringent than the previous one.

The ^{7}Be(d,t)^{6}Be reaction has been studied in order to search for resonances in the unbound ^{6}Be nucleus using a radioactive ^{7}Be beam at the ORNL HRIBF. The level structure of the ^{6}Be nucleus is crucial in understanding the behavior of the ^{3}He(^{3}He,2p)^{4}He reaction rate at low energies. Because of its importance, the ^{3}He(^{3}He, 2p)^{4}He reaction has been studied several times at a variety of energies. However, the reason for a rise in the ^{3}He(^{3}He,2p)^{4}He S-factor at low energies is not clear. Since the ^{7}Be(d,t)^{6}Be reaction has never been studied before, the reaction could populate the unknown states in ^{6}Be nucleus. The 100 MeV beam of ^{7}Be at HRIBF impinged on a 1.0 mg/cm^2 CD$_2$ solid target in order to search for unbound states in ^{6}Be nucleus. The average beam current on the target was $\sim 10^6$ particles per second, and total of 3.4×10^{11} ^{7}Be ions bombarded the target. Recoil tritons from the d(^{7}Be,t)^{6}Be reaction were detected by SIDAR at $14^\circ \leq \theta_{lab} \leq 32^\circ$. The beam energy, target thickness, and the angular range were chosen to optimize sensitivity around 10 MeV in excitation energy of ^{6}Be. Two silicon strip detector arrays acted as ΔE and E detectors respectively, and tritons were identified by a standard energy loss technique. However, large amounts of ^{3}He particles "punch through" the E detector, only partially depositing their energy and producing a "back-bending" locus that overlaps with the triton group. Another layer of detectors was placed behind the E detectors to detect the ^{3}He punch through and to reject those events from tritons spectra. The triton energy spectrum is rather featureless, indicating that direct transfer to ^{6}Be levels is not particularly strong. Other reaction mechanisms producing tritons were therefore investigated, including a phase space model and three-body continuum. The data were, however, not well described by either background process considered, and thus we have set upper limits on the cross section to populate such levels. In most cases, our observed cross sections are larger than the DWBA calculations, indicating that a mixture of reaction mechanisms is involved.

Bibliography

Bibliography

[Ada87] E. Adamides, H. G. Bohlen, W. von Oertzen, M. Buenerd, J. Chauvin, D. Lebrun, J. Y. Hostachy, P. Martin, G. Perrin, and P. de Saintgnon, Nucl. Phys. A **475**, 598 (1987).

[Alt94] G. D. Alton, G. D. Mills, and J. Dellwo, Rev. Sci. Instrum. **65**, 2006 (1994).

[Alt98] G. D. Alton and J. R. Beene, J. Phys. G **24**, 1347 (1998).

[Bar99] D. W. Bardayan, *Explosive* ^{17}*F(p,γ)*^{18}*Ne Burning Through the 3*$^{+}$ *State in* ^{18}*Ne*, Ph.D. thesis, Yale University, 1999.

[Bar00] D. W. Bardayan, J. C. Blackmon, W. Bradfield-Smith, C. R. Brune, A. E. Champagne, T. Davinson, B. A. Johnson, R. L. Kozub, C. S. Lee, R. Lewis, P. D. Parker, A. C. Shotter, M. S. Smith, D. W. Visser, , and P. J. Woods, Phys. Rev. C **62**, 042802(R) (2000).

[Bar01] D. W. Bardayan, J. C. Blackmon, W. Bradfield-Smith, C. R. Brune, A. E. Champagne, T. Davinson, B. A. Johnson, R. L. Kozub, C. S. Lee, R. Lewis, P. D. Parker, A. C. Shotter, M. S. Smith, D. W. Visser, and P. J. Woods, Phys. Rev. C **63**, 065802 (2001).

[Bar02] D. W. Bardayan, J. C. Batchelder, J. C. Blackmon, A. E. Champagne, T. Davinson, R. Fitzgerald, W. R. Hix, C. Iliadis, R. L. Kozub, Z. Ma,

S. Parete-Koon, P. D. Parker, N. Shu, M. S. Smith, and P. J. Woods, Phys. Rev. Lett. **89**, 262501 (2002).

[Bar04] D. W. Bardayan, J. C. Blackmon, J. G. del Campo, R. L. Kozub, J. F. Liang, Z. Ma, L. Sahin, D. Shapira, and M. S. Smith, Phys. Rev. C **70**, 015804 (2004).

[Bet37] H. A. Bethe, Rev. Mod. Phys. **9**, 69 (1937).

[Bev86] J. J. Bevelacqua, Phys. Rev. C **33**, 699 (1986).

[Bod62] D. Bodansky, Annu. Rev. Nucl. Sci. **12**, 79 (1962).

[Boh37] N. Bohr, Science **86**, 161 (1937).

[Boh85] H. G. Bohlen, H. Ossenbrink, H. Lettau, and W. von Oertzen, Z. Phys. A **320**, 237 (1985).

[Boh01] H. G. Bohlen, R. Kalpakchieva, A. Blažević, B. Gebauer, T. N. Massey, W. von Oertzen, and S. Thummerer, Phys. Rev. C **64**, 024312 (2001).

[Bol07] B. Boltwood, Am. J. Sci. **23**, 77 (1907).

[Bon99] R. Bonetti, C. Broggini, L. Campajola, P. Corvisiero, A. D'Alessandro, M. Dessalvi, A. D'Onofrio, A. Fubini, G. Gervino, L. Gialanella, U. Greife, A. Guglielmetti, C. Gustavino, G. Imbriani, M. Junker, P. Prati, V. Roca, C. Rolfs, M. Romano, F. Schuemann, F. Strieder, F. Terrasi, H. P. Trautvetter, and S. Zavatarelli, Phys. Rev. Lett. **82**, 5205 (1999).

[Bre40] G. Breit, Phys. Rev. **58**, 1068 (1940).

[Bur57] E. M. Burbidge, G. R. Burbidge, W. A. Fowler, and F. Hoyle, Rev. Mod. Phys. **29**, 547 (1957).

[Cas96] V. Castellani, G. Fiorentini, B. Ricci, and O. Straniero, Z. Phys. **354**, 237 (1996).

[Chr90] N. S. Christensen, F. Jensen, F. Besenbacher, and I. Stensgaard, Nucl. Instrum. Methods Phys. Res. B **51**, 97 (1990).

[Cla83] D. D. Clayton, *Principles of Stellar Evolution and Nucleosynthesis*, Univ. of Chicago Press, 1983.

[Coc00] A. Coc, M. Hernanz, J. José, and J.-P. Thibaud, Astron. Astrophys. **357**, 561 (2000).

[Cos95] R. Coszach, M. Cogneau, C. R. Bain, F. Binon, T. Davinson, P. Decrock, T. Delbar, M. Gaelens, W. Galster, J. Goerres, J. S. Graulich, R. Irvine, D. Labar, P. Leleux, M. Loiselet, C. Michotte, R. Neal, G. Ryckewaert, A. S. Shotter, J. Vanhorenbeeck, J. Vervier, M. Wiescher, and P. Woods, Phys. Lett. B **353**, 184 (1995).

[Del83] T. Delbar, G. Grégoire, Belery, and G. Paić, Phys. Rev. C **27**, 1876 (1983).

[deS05] N. de Séréville, E. Berthoumieux, and A. Coc, Nucl. Phys. A **758**, 745c (2005).

[Edd20] A. S. Eddington, Nature **106**, 14 (1920).

[ElN70] M. El-Nadi, O. Zhohni, and H. M. Hussein, Ann. Phys. (Leipzig) **25**, 1 (1970).

[End05] ENDF-6 Formats Manual.

[Fer50] E. Fermi, Prog. Theor. Phys. **5**, 570 (1950).

[Fet75] V. N. Fetisov and Y. S. Kopysov, Nucl. Phys. A **239**, 511 (1975).

[Fit05] R. P. Fitzgerald, *Measurement of the* $^{1}H(^{7}Be,^{8}B)\gamma$ *cross section*, Ph.D. thesis, University of North Carolina at Chapel Hill, 2005.

[Fow67] W. A. Fowler, *Nuclear Astrophysics*, American Philosophical Society, 1967.

[Fre65] R. M. Freeman and G. S. Mani, Proc. Phys. Soc. (London) **85**, 267 (1965).

[Gia02] L. Gialanella, U. Greife, N. D. Cesare, A. D'Onofrio, M. Romano, L. Campajola, A. Formicola, Z. Fulop, G. Gyurky, G. Imbriani, C. Lubritto, A. Ordine, V. Roca, D. Rogalla, C. Rolfs, M. Russo, C. Sabbarese, E. Somorjai, F. Strieder, F. Terrasi, and H. P. Trautvetter, Nucl. Instrum. Methods Phys. Res. B **197**, 150 (2002).

[Gra00] J.-S. Graulich, S. Cherubini, R. Coszach, S. E. Hajjami, W. Galster, P. Leleux, W. Bradfield-Smith, T. Davinson, A. D. Pietro, A. C. Shotter, J. Görres, M. Wiescher, F. Binon, and J. Vanhorenbeeck, Phys. Rev. C **63**, 011302 (2000).

[Gui03] V. Guimarães, R. Kuramoto, R. Lichtenthäler, G. Amadio, E. Benjamin, P. N. de Faria, and A. Lépine-Szily, Nucl. Phys. A **722**, 341c (2003).

[Her99] M. Hernanz, J. José, A. Coc, J. Gómez-Gomar, and J. Isern, Astrophys. J. **526**, L97 (1999).

[Hil79] D. Hilscher, J. R. Birkelund, A. D. Hoover, W. U. Schroder, W. W. Wilcke, J. R. Huizenga, A. C. Mignerey, K. L. Wolf, H. F. Breuer, and V. E. Viola, Phys. Rev. C **20**, 556 (1979).

[Hix99] W. R. Hix and F. Thielemann, J. Comp. Appl. Math. **109**, 321 (1999).

[Iga] University of Surrey modified verion of the doce TWOFNR of M. Igarashi, M. Toyama, and N. Kishida, unpublished.

[Infra] http://www.nucastrodata.org.

[Jam88] A. N. James, T. P. Morrison, K. L. Ying, K. A. Connell, H. G. Price, and J. Simpson, Nucl. Inst. Meth. **267**, 144 (1988).

[Jos06] J. José and M. Hernanz, Eur. Phys. J. A **27**, 107 (2006).

[Jun98] M. Junker, A. D'alessandro, S. Zavatarelli, C. Arpesella, E. Bellotti, C. Broggini, P. Corvisiero, G. Fiorentini, A. Fubini, G. Gervino, U. Greife, C. Gustavino, J. Lambert, P. Prati, W. S. Rodney, C. Rolfs, F. Strieder, H. P. Trautvetter, and D. Zahnow, Phys. Rev. C **57**, 2700 (1998).

[Kno00] G. F. Knoll, *Radiation Detection and Measurement*, Wiley, 2000.

[Koz05] R. L. Kozub, D. W. Bardayan, J. C. Batchelder, J. C. Blackmon, C. R. Brune, A. E. Champagne, J. A. Cizewski, T. Davinson, U. Greife, C. J. Gross, C. C. Jewett, R. J. Livesay, Z. Ma, B. H. Moazen, C. D. Nesaraja, L. Sahin, J. P. Scott, D. Shapira, M. S. Smith, J. S. Thomas, and P. J. Woods, Phys. Rev. C **71**, 032801 (2005).

[Kra87] Krane, *Introductory Nuclear Physics*, Wiley, 1987.

[Kud04] N. Kudomi, M. Komori, J. Takashisa, S. Yoshida, K. Kume, H. Ohsumi, and T. Itahashi, Phys. Rev. C **69**, 015802 (2004).

[Lan58] A. M. Lane and R. G. Thomas, Rev. Mod. Phys. **30**, 257 (1958).

[Lis75] H. Liskienk and A. Paulsen, At. Data Nucl. Data Tables **15**, 57 (1975).

[Mic06] http://www.micronsemiconductor.co.uk.

[Nel85] R. O. Nelson, E. G. Bilpuch, and G. E. Mitchell, Nucl. Instrum. Methods Phys. Res. A **236**, 128 (1985).

[Nou98] S. Nouri, Phys. Rev. A **57**, 1526 (1998).

[Pad00b] T. Padmanabhan, *Theoretical Astrophysics Volume II: Stars and Stellar Systems*, Cambridge University Press, 2000.

[Per03] D. Perkins, *Particle Astrophysics*, Oxford University Press, 2003.

[Par03] S. Parete-Koon, W. R. Hix, M. S. Smith, S. Starrfield, D. W. Bardayan, M. W. Guidry, and A. Mezzacappa, Astrophys. J. **598**, 1239 (2003).

[Rau01] T. Rauscher and F. Thielemann, At. Data Nucl. Data Tables **79**, 47 (2001).

[Reh96] K. E. Rehm, M. Paul, A. D. Roberts, C. L. Jiang, D. J. Blumenthal, S. M. Fischer, J. Gehring, D. Henderson, J. Nickles, J. Nolen, R. C. Pardo, J. P. Schiffer, and R. E. Segel, Phys. Rev. C **53**, 1950 (1996).

[Rol88] C. Rolfs and W. S. Rodney, *Cauldrons in the Cosmos*, Univ. of Chicago Press, 1988.

[Rui03] C. Ruiz, *Aspects of Nuclear Phenomona Under Explosive Astrophysical Conditions*, Ph.D. thesis, University of Edinburgh, 2003.

[Sch01] H. Schatz, A. Aprahamian, V. Barnard, L. Bildsten, A. Cumming, M. Ouellette, T. Rauscher, F.-K. Thielemann, and M. Wiescher, Phys. Rev. Lett. **86**, 3471 (2001).

[Sta98] S. Starrfield, J. W. Truran, M. C. Wiescher, and W. M. Sparks, Mon. Not. R. Astron. Soc. **296**, 502 (1998).

[Str03] D. W. Stracener, Nucl. Instrum. Methods Phys. Res. B **204**, 42 (2003).

[Til02] D. R. Tilley, C. M. Cheves, J. L. Godwin, G. M. Hale, H. M. Hofmann, J. H. Kelley, C. G. Sheu, and H. R. Weller, Nucl. Phys. A **708**, 3 (2002).

[Tim99] N. K. Timofeyuk, Nucl. Phys. A **652**, 132 (1999).

[Utk98] S. Utku, J. G. Ross, N. P. T. Bateman, D. W. Bardayan, A. A. Chen, J. Görres, A. J. Howard, C. Iliadis, P. D. Parker, M. S. Smith, R. B. Vogelaar, M. Wiescher, and K. Yildiz, Phys. Rev. C **57**, 2731 (1998).

[Vog59] E. Vogt, *Resonance Reactions, Theoretical: Nuclear Reactions*, North Holland, 1959.

[Vog62] E. Vogt, Rev. Mod. Phys. **34**, 723 (1962).

[Wel99] R. F. Welton, R. L. Auble, J. R. Beene, J. C. Blackmon, J. Kormicki, P. E. Mueller, D. W. Stracener, and C. L. Williams, Nucl. Instrum. Methods Phys. Res. B **159**, 116 (1999).

[Wel02] R. F. Welton, Nucl. Phys. A **701**, 452c (2002).

Vita

Kyung Yuk Chae was born in Seoul, Korea (Republic of) on September 16, 1975. After completing high school at Yoido high school in 1994, he attended Sogang University in Korea (March 1994 - February 2000), where he received his Bachelor of Science degree in Physics. During that period, he served in the Korea Army for 26 months. He then entered the University of Tennessee at Knoxville in the fall of 2001. He is currently working towards his Ph.D. in Physics.